Turbulent Skin-Friction Drag Reduction via Spanwise Wall Oscillations

Vom Fachbereich Maschinenbau
an der Technischen Universität Darmstadt
zur
Erlangung des Grades eines Doktor-Ingenieurs (Dr.-Ing.)
genehmigte

D i s s e r t a t i o n

vorgelegt von

M.Sc. Davide Gatti

aus S. Angelo Lodigiano (Italien)

Berichterstatter:	Prof. Dr.-Ing. C. Tropea
Mitberichterstatter:	Prof. Dr.-Ing. H. F. Schlaak
Mitberichterstatter:	Prof. Dr.-Ing. B. Frohnapfel
Tag der Einreichung:	21.10.2015
Tag der mündlichen Prüfung:	17.12.2014

Darmstadt 2015
D17 (Diss. Darmstadt)

Hiermit versichere ich, die vorliegende Doktorarbeit unter der Betreuung von Prof. Dr.-Ing. C. Tropea und Prof. Dr.-Ing. B. Frohnapfel nur mit den angegebenen Hilfsmitteln selbständig angefertigt zu haben.

Darmstadt, den 21. Oktober 2014,

Abstract

The present work aims at contributing to the development of active flow control via spanwise wall oscillations for turbulent skin-friction drag reduction with numerical and experimental tools, both improving our understanding of their mechanisms and to easing laboratory implementation with a novel actuator principle: the dielectric elastomer actuators (DEA).

Dielectric elastomer actuators, capable of large in-plane wall motions, are developed and thoroughly characterized for suitability in flow-control applications. The influence of a major design parameter, the amount of pre-stretch, on static and dynamic actuation is extensively discussed and an optimal combination is found, which yields the best trade-off between actuation amplitude and frequency.

DEA-based spanwise oscillating surfaces are tested in a laboratory, low-Reynolds number (Re), fully developed turbulent channel flow, where they yield an actively-induced relative decrease in skin-friction of about 5%. Measurements of the real power required to impose the spanwise oscillations are performed and enable to evaluate the control performance in terms of energetic efficiency. A negative yet promising net power saving, budget between the energy saving and expenditure, is achieved which is several order of magnitude larger than previous experiments with conventional actuator technologies.

Direct numerical simulations (DNS) of fully developed turbulent channel flows are performed to study the effects of inhomogeneous actuation on control performance. Spatial onset transients are investigated as source of the commonly-observed discrepancies between laboratory and numerical experiments, by directly comparing the experimental investigations to their numerical idealized representation.

The rate at which the drag reduction deteriorates at increasing Re is investigated by exploring a new DNS dataset of turbulent channel flows controlled through an alternative spanwise wall forcing method: the streamwise-traveling waves of spanwise wall velocity. A mathematical relationship between the Reynolds number and the drag reduction is found to predict the dominant part of this decay, which is not specific to the particular control technique but rather inherent in the definition of drag reduction rate.

Kurzfassung

Das Ziel der vorliegenden Arbeit ist aktive Strömungskontrolle mittels Wandbewegung quer zur Strömungsrichtung zur Reduktion turbulenter Oberflächenreibung mit numerischen und experimentellen Werkzeugen beizutragen. Diese dienen dem besseren Verständnis der Mechanismen, sowie der Ermöglichung einer Anwendung eines neuartigen Aktuationsprinzips in Laborexperimenten: den dielektrischen Elastomeraktoren (DEA).

Dielektrische Elastomeraktoren, die die Fähigkeit zu großen Bewegungen in der Wandebene besitzen, werden entwickelt und hinsichtlich ihrer Eignung zur Strömungskontrolle charakterisiert. Der Einfluss eines Hauptmerkmals, des Betrags der Vorspannung, auf statische und dynamische Bewegung wird ausführlich diskutiert. Hierdurch wird eine optimale Abstimmung zwischen Amplitude und Frequenz der Bewegung dargestellt.

DEA-basierte oszillierende Flächen werden im Labor bei niedrigen Reynolds-Zahlen (Re) in einer vollentwickelten turbulenten Kanalströmung getestet, in der sie eine aktiv induzierte Absenkung der Wandreibung um 5% erzielen. Zusätzlich werden Messungen der real verbrauchten Energie zur Erzeugung von Oszillationen quer zur Strömungsrichtung durchgeführt, was die Beurteilung der Kontrollleistung in Bezug auf die energetische Effizienz ermöglicht. Auf diese Weise wird zwar eine negative aber dennoch vielversprechende Energiebilanz zwischen Energieersparnis und –aufwand erreicht, die um einige Größenordnungen höher liegt als mit bisher getesteten konventionellen Aktuationsprinzipien.

Direkte Numerische Simulationen (DNS) von vollentwickelten turbulenten Kanalströmungen werden durchgeführt, um die Auswirkung inhomogener Bewegungen auf die Kontrollleistung zu untersuchen. Der direkte Vergleich der experimentellen Untersuchung mit ihrer numerischen Abbildung weist ein räumlich verzögertes Einsetzen auf, welches ein Grund für die häufig beobachteten Diskrepanzen zwischen Laborexperimenten und numerischen Studien ist.

Der Grad, mit dem die Reibungsreduktion bei steigender Re abnimmt, wird anhand eines neuen DNS Datensatzes für die Kontrolle turbulenter Kanalströmungen mit einer alternativen Wandbewegung quer zur Strömungsrichtung beurteilt: die vorwärts bewegende Wellen transversaler

Geschwindigkeit. Eine mathematische Beziehung zwischen der Reynolds-Zahl und der Reibungsminderung zur Vorhersage des dominierenden Anteils der Abnahme wird vorgestellt, die nicht spezifisch für die bestimmte Kontrolltechnik, sondern aus der Definition der Reibungsminderung vorgegeben ist.

Acknowledgments

First of all I gratefully acknowledge the support and generosity of Prof. Dietmar Hennecke and the Fritz und Margot Faudi Stitung for having financed my research and given me the unique possibility of accomplishing my Ph.D at the Technische Univesität Darmstadt.

I would like to express my special appreciation and thank to Prof. Cameron Tropea, for having trusted me and offered all the infrastructures and support I needed in the last three years. His love for science, passion and total dedication to its institute have been a model for me.

Prof. Bettina Frohnapfel deserves special words of thank for having selected me for this project, supported throughout my whole Ph.D. and motivated me till the very end. Cooperating with a professor can hardly be easier and more pleasant than with her.

I would like to thank Prof. Helmut F. Schlaak for having hosted me at the Institute of Electromechanical Design during the last two years. At his institute I experienced a very stimulating atmosphere, with a unique and cohesive group of colleagues.

A personal thank is for Prof. Maurizio Quadrio, from whom I learned simplicity, pragmatism, honesty and curiosity. Working together in the last years has been an honour and a real enjoyment.

The wind-tunnel experiments would have not been possible without the wind-tunnel built by Andreas Güttler, with no doubt the best engineer I have ever met, and a great friend.

I would like to thank the colleagues of the Dielectric Elastomer Actuator research group of the Institute of Elechtromechanical Design: Henry Haus, Holger Mössinger, Florentine Förster, Roman Karsten and Tanja Grotepaß. I really enjoyed spending the last two years with these excellent and helpful colleagues. A special thanks is for Marc Matysek, who helped me rapidly start in the new institute and whose advices have been precious.

In particular, I must mention two friends, Henry Haus and Tanja Stosik, for having significantly helped print this document and having made the last moment before its submission very enjoyable.

I would like to thank the colleague of the Computational Physical Chemistry group of the Center of Smart Interfaces for significantly improving the

working environment. My three years of Ph.D. could not have been so funny and special without Emiliano Brini, a good-mood bomb and a tireless optimist. I must thank Valentina Marcon, for having continuously motivated and supported me during many important choices in the last three years. Every coffee break spent together has been very precious.

Moreover, I would like to thank many colleagues and friends with whom I enjoyed special moments that left a footprint in me: Marcus Camarinha Lopes, Kathrin Fasold, Claudia Herbers, Francesco Pastori, Daniela Werm, Livia Marnetto and Fabio Grossi.

My scientific and cultural development would not have been worth it without those people that contributed to my personal enrichment. I am truly grateful to my parents, from which I inherited modesty and simplicity. I am very grateful to my sister for having coloured the family in the last years and to my brother for some beautiful small trips that we should repeat and for having taught some details of human history.

I would like to acknowledge the support and encouragement I received from my parents-in-law, Carolina and Gianluigi, throughout the years. A special thank is for Annalisa - a red, curly-haired concentrate of humanity, generosity and simplicity - for always being at my side.

Finally I would like to thank Rossella, for being the bright sunshine over the golden wheat, the cool breeze after a thunderstorm, the jasmine scent at the twilight, the dew in the dawn and many other slight and wandering things.

Contents

1 Introduction

Flow control aimed at reducing the turbulent skin friction is a challenging theoretical and technological problem and is being intensively pursued by the scientific community. The challenge lies in bridging the broad range of concepts involved: on the one hand the continuously expanding understanding of turbulent wall-bounded flows enables the formulation of new strategies to influence a flow; on the other hand any passive or active flow control technique requires highly sophisticated micro-machining to produce finely structured surfaces, riblets being the most famous example, or highly-developed micro-sensors and actuators.

Particularly promising and appealing are active control techniques, whose forcing consist of a pre-determined, periodic wall movement. Being pre-determined, they have no need for distributed, real-time, micro-sensing over large surfaces. Moreover, they only require actuation at the boundaries, where actuators can be embedded in surfaces. The rationale for affecting the near-wall region of wall-bounded flows relies on the fact that most of the turbulent activity that accounts for the skin-friction arises in the so-called autonomous near-wall cycle. If the near-wall turbulence is favourably influenced, the wall friction drag may decrease. Such an achievement would have paramount importance in both scientific and industrial communities: the former due to the broadened horizon and understanding of turbulent flow dynamics, which may lead to improved flow conditioning strategies; the second relates to bringing active flow control to practice, driven by the potentially large economical savings and environmental improvements.

In the number of the possible drag-reducing wall actuations, in-plane wall oscillations in the direction normal to the mean flow, called spanwise oscillations, have been the focus of many studies in the literature of the last 20 years, after the first seminal work of Jung et al. [6]. Various reasons explain the interest in this particular sub-class of control techniques. The first involves the direction of the forcing. Forcing in the spanwise direction is found to be quite effective, though not significantly disrupting the natural state of near-wall turbulence, as wall-normal forcing usually does. Moreover, turbulent wall-bounded flows subject to spanwise wall oscillations exhibit friction drag reduction from about 20% in the few proof-of-principle

experimental verifications to 40% in Direct Numerical Simulations (DNS) of low-Reynolds number channel flows. Finally, the relative simplicity of the wall movement makes their experimental implementation more realistic than other techniques while the high reduction of turbulent friction drag makes a direct measurement feasible.

In spite of their various captivating features, the development of spanwise oscillations into an established drag-reducing technique has been slow, due to severe conceptual and technological problems. On the one hand, our understanding of turbulence, in general, and of the complex interplay of spanwise wall forcing and wall turbulence, in particular, is still so limited that some important questions remain unanswered. The biggest open issue is the portability of the experimental and numerical evidence, usually obtained at relatively low Reynolds (Re) number, to higher-Re flows typical of most industrial applications. The limited evidence to date clearly shows that the drag-reducing capability of many active and passive near-wall control techniques, including spanwise oscillations, decreases with Re at a rate that may make their usefulness at high-Re flows questionable. Drawing conclusions about the high-Re behavior of the present control technique on the basis of numerical or laboratory experiments is impeded, since comprehensive investigations at high-Re are missing mainly because of the difficulties in running high-Re numerical or laboratory experiments.

On the other hand, despite the relative simplicity, the spanwise oscillation concept is difficult to realize in practice. Being energy efficient, lightweight and within the space- and timescale of near-wall turbulence are requisites difficult to fulfill in a device. In fact, spanwise oscillations have been tested almost solely numerically, and the few attempted experimental implementations are proof-of-principle laboratory experiments in which the spanwise wall velocity is achieved by moving the wall through bulky crank-driven mechanisms. Though effective in reaching their aim, such solutions are generally energetically inefficient, require significant modifications of the wind tunnel test section and, most importantly, do not lend themselves to developing a system-integrated, compact solution.

The present work aims at contributing to the development of active flow control via spanwise wall forcing with numerical and experimental tools, both trying to improve our understanding of their mechanisms and to ease their laboratory implementation with a novel actuator principle: the dielectric elastomer actuators (DEA). The only attempt to date by Gouder et al. [58], where spanwise wall oscillations and DEA-based actuators were combined, revealed that “the technology is still immature, often leading to

fragile actuators with a high proportion of failures" [57]. In this work, we develop new, simple, dielectric-elastomer-based actuators with improved robustness and dynamic performances. After a mechanical and electrical characterization of both the final device and the dielectric material, we run wind-tunnel tests in an air channel flow, in which it is shown that accurate measurements of the actively drag reduction is possible.

The validity of the low-Re experimental evidence obtained at higher-Re flows is studied with the aid of theoretical arguments and a newly generated very large database of direct numerical simulations (DNS) of controlled turbulent channel flows at relatively high Reynolds number.

The present work sets the following goals:

- Research, develop and characterize active surfaces made of dielectric elastomer actuators that realize spanwise wall oscillations.
- Critically assess dielectric elastomer membrane actuators for turbulent flow-control applications, including consideration on energy efficiency and frequency bandwidth.
- Experimentally measure drag reduction via DEA-based spanwise oscillating surfaces in a turbulent channel flow at low-Reynolds numbers.
- Examine the effect of non-homogeneous actuation on the achievable skin-friction drag reduction.
- Investigate the effect that the Reynolds number has on drag reduction. Is the low-Re experimental evidence valid for high-Re turbulent flows?

2 Fundamentals and state of the art

In this Chapter, the two main scientific topics of the present work are introduced. Section 2.1 discusses fundamental concepts of turbulence and turbulent flows, with a focus on fully developed turbulent channel flows. Turbulent flow-control strategies aimed at reducing the skin-friction drag are classified, before describing in detail aspects of the two main techniques based on spanwise wall forcing: spanwise wall oscillations and streamwise-traveling waves of spanwise wall velocity.

Section 2.2 presents general principles of dielectric elastomer actuators (DEA), the actuator technology utilized to experimentally implement spanwise wall oscillations. Their working principle is described with both infinitesimal and finite-strain theory. The most elemental actuator configurations are presented, with a focus on those applicable to aeronautical applications.

2.1 Turbulent flows and their control

Most flows occurring in nature are turbulent flows, from geophysical and astronomical flows, flows around cars and airplanes, to rivers, flows in ducts and the smoke of a chimney. Our innate idea of turbulence is based on everyday experience and is associated with some of its features, such as chaos, irregularity and unsteadiness. In his famous experiment, Reynolds [135] distinguished very intuitively between direct and sinuous motion of a flow, efficaciously describing in one word the randomness and high mixing associated with turbulence.

The focus of the present work is oriented to one of the fundamental manifestations of turbulence in the simplest wall-bounded flows: the increase of friction drag above the laminar value. Although desirable for improving heat exchanges or to delay flow separation, high friction losses are unwanted in many applications where friction represents the main energy sink, prompting the study of techniques aimed at skin-friction drag reduction in the turbulent regime.

In the following, the turbulent channel flow, used in the present numerical and experimental investigations, is described. The main features which

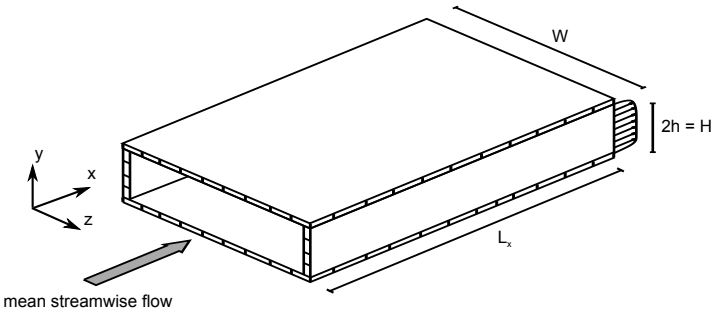

Figure 2.1: Sketch of a channel flow.

generate and sustain near-wall turbulence are identified and characterized. Finally, spanwise wall forcing as means for turbulence skin-friction drag reduction is presented.

2.1.1 Turbulent Channel flow

Description of the flow

A channel flow, through a rectangular duct of height $H = 2h$, length $L_x \gg h$ and aspect ratio $W/H \gg 1$ is sketched in Figure 2.1. The mean flow is predominantly in the x-direction, called streamwise, with the mean velocity varying mainly in the y-direction, called wall-normal direction. The extent of the channel in the spanwise direction is large enough to consider the flow statistically homogeneous in the z-direction, called spanwise direction. The centerline is located at $y = h$ and $z = 0$, while the bottom and the top walls are placed at $y = 0$ and $y = 2h = H$ respectively. Far away from the inlet the flow in said to be fully developed and is statistically homogeneous in the x direction and statistically stationary.

u, v and w are the streamwise, wall-normal and spanwise velocity components respectively, grouped in the velocity vector $\mathbf{u}$, which can be decomposed into its mean $\langle \mathbf{u} \rangle$ and the turbulent fluctuation $\mathbf{u}'$ as follows:

$$\mathbf{u}(\mathbf{x}, t) = \langle \mathbf{u}(\mathbf{y}) \rangle + \mathbf{u}'(\mathbf{x}, t) \tag{2.1}$$

The Reynolds numbers that characterize the flow are:

$$Re_b = \frac{2U_b h}{\nu} \tag{2.2}$$

$$Re_c = \frac{U_c h}{\nu} \tag{2.3}$$

where $U_c = \langle u \rangle_{y=h}$ is the centerline velocity, ν is the kinematic viscosity of the fluid and $\langle \cdot \rangle$ is the averaging operator along the statistically homogeneous directions, time included.

As there is no mean streamwise acceleration in the flow, the streamwise balance of mean momentum yields the following important relation between the streamwise shear stress $\tau_x(y)$ and the mean wall pressure gradient $\mathrm{d}p_w/\mathrm{d}x$:

$$\frac{\mathrm{d}\tau(y)}{\mathrm{d}y} = \frac{\mathrm{d}p_w}{\mathrm{d}x} \tag{2.4}$$

where the total shear stress $\tau_x(y)$ is

$$\tau_x(y) = \rho\nu \frac{\mathrm{d}\langle u \rangle}{\mathrm{d}y} - \rho\langle u'v' \rangle \tag{2.5}$$

the sum of the viscous stress $\rho\nu \mathrm{d}\langle u \rangle/\mathrm{d}y$ and the Reynolds stress $-\rho\langle u'v' \rangle$.

Since $\tau(y)$ is a function of only y, and $\mathrm{d}p_w/\mathrm{d}x$ a function of only x, it is evident from Equation 2.4 that both $\mathrm{d}\tau(y)/\mathrm{d}y$ and $\mathrm{d}p_w/\mathrm{d}x$ are constant. By defining $\tau_x \equiv \tau(0)$, Equation 2.4 can be integrated in y to yield:

$$\frac{\tau_x}{h} = -\frac{\mathrm{d}p_w}{\mathrm{d}x} \tag{2.6}$$

which relates the wall shear stress to the pressure drop along the channel. Combining Equations 2.4 and 2.6 and integrating in y direction results in:

$$\tau(y) = \tau_w \left(1 - \frac{y}{h}\right) \tag{2.7}$$

which states that the total shear stress varies linearly with y.

The no-slip boundary condition dictates that the turbulent fluctuations must be zero at the wall, consequently the wall shear stress is only due to the viscous contribution:

$$\tau_x = \rho\nu \left.\frac{\mathrm{d}\langle u \rangle}{\mathrm{d}y}\right|_{y=0} \tag{2.8}$$

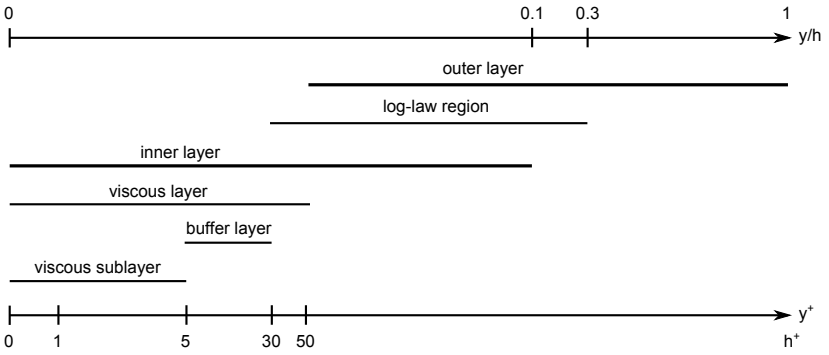

Figure 2.2: A sketch of the various regions and layers of wall turbulence defined in terms of y/h and $y^+ = y/\delta_\nu$

In the vicinity of the wall, where viscous effects dominate, viscous scales can be defined, based on the two locally important parameters ν and τ_x. These are:

$$u_\tau = \sqrt{\frac{\tau_x}{\rho}}, \qquad \delta_\nu = \frac{\nu}{u_\tau}, \qquad t_\nu = \frac{\nu}{u_\tau^2} \tag{2.9}$$

where u_τ, δ_ν and t_ν are a velocity, time, and space scale typical of the near-wall turbulence.

An additional Reynolds number, the friction Reynolds number Re_τ, characterize the near-wall turbulence and is defined as:

$$Re_\tau = \frac{u_\tau h}{\nu} \tag{2.10}$$

The distance from the wall, measured in viscous lengths, also called wall units, is

$$y^+ = \frac{y}{\delta_\nu} = \frac{y u_\tau}{\nu} \tag{2.11}$$

and is similar to a local Reynolds number, so that its magnitude can determine the relative importance of viscous and turbulent processes [124]. According to the value of y^+, different regions, or layers, are defined. In the viscous layer $y^+ < 50$, the viscosity has a direct effect on the shear stresses $\tau(y)$. In the outer layer $y^+ > 50$ the effect of viscosity is negligible. Within the viscous layer, in the viscous sublayer $y^+ < 5$, the Reynolds stresses are negligible.

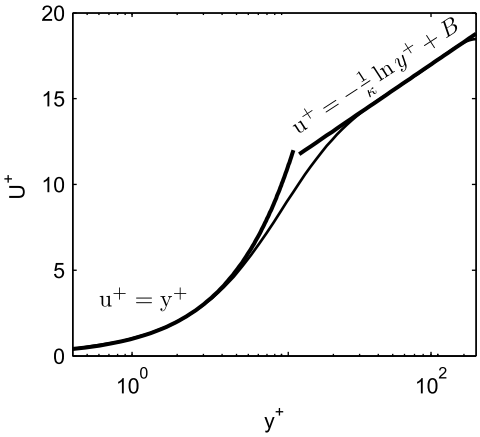

Figure 2.3: Mean velocity profile in fully-developed turbulent channel flow. Thin solid line: data from direct numerical simulation (DNS) experiments at $Re_b = 6350$ ($Re_\tau = 200$); thick solid lines: the law of the wall in viscous sublayer (Eq. 2.12) and lo-law regions (Eq. 2.13).

Mean velocity profile

Based on dimensional analysis and on the local importance of the viscous effects, the mean velocity profile of a turbulent channel flow can be partially predicted, starting from the so-called law of the wall. The reader can find a detailed description of the theoretical background in Pope [124].

Figure 2.2 shows the various layers in which the channel can be segmented. In the inner layer $y/h < 0.1$ the velocity is assumed not to be a function of the position y/h across the channel but on the distance y^+ from the wall. Within the viscous sublayer, in the innermost edge of the inner layer, from the definition of u_τ leads to:

$$u^+ = y^+ \tag{2.12}$$

where $u^+ = \langle u \rangle / u_\tau$.

At sufficiently high Reynolds numbers, a region between the outermost part of the inner layer $y^+ > 30$ and the innermost part of the outer layer exists $y/h < 0.3$, where the following logarithmic law, or simply log law,

holds:

$$u^+ = \frac{1}{\kappa} \ln y^+ B \tag{2.13}$$

where $\kappa = 0.41$ is the von Kármán constant and $B \approx 5.2$. Both are deemed to be universally constant at high Reynolds numbers.

Figure 2.3 shows Equations 2.12 and 2.13, superimposed to the mean velocity profile of a turbulent channel flow at moderately low Re. The agreement is excellent in the respective regions of validity and improves with Re.

With similar arguments, the velocity can be assumed to be a function of y/h only close to the centerline of the channel, where the viscous effects are negligible. In this region, the following velocity-defect law can be derived:

$$\frac{U_c - \langle u \rangle}{u_\tau} = -\frac{1}{\kappa} \ln \left(\frac{y}{h} \right) + B_1 \tag{2.14}$$

where the constant B_1 is flow-dependent, which represents the difference between the law of Equation 2.14 and the real centerline velocity U_c. Evaluating 2.14 at the centerline $y = h$ yields:

$$\frac{U_c - U_{c,log}}{u_\tau} = B_1 \tag{2.15}$$

where $U_{c,log}$ denotes the value of $\langle u \rangle$ at the centerline according to Equation 2.14. The constant B_1 is normally nonzero [39, 82] but is relatively small $B_1 < 1$, meaning that the Equation 2.14 is a good approximation of the defect-velocity profile at the centerline.

Friction law

The wall shear stress normalized by a reference velocity is called a skin-friction coefficient. On the basis of U_b and U_c two different skin-friction coefficients can be defined:

$$C_f = 2\tau_x / \left(\rho U_b^2 \right) \tag{2.16}$$

$$c_f = 2\tau_x / \left(\rho U_c^2 \right) \tag{2.17}$$

which are function of the Reynolds number only. U_b is the average or bulk velocity in the channel and U_c is the centerline velocity. In laboratory experiments, C_f is a mild function of the aspect ratio of the channel, as the flow uniformity across the channel decreases for decreasing aspect ratios.

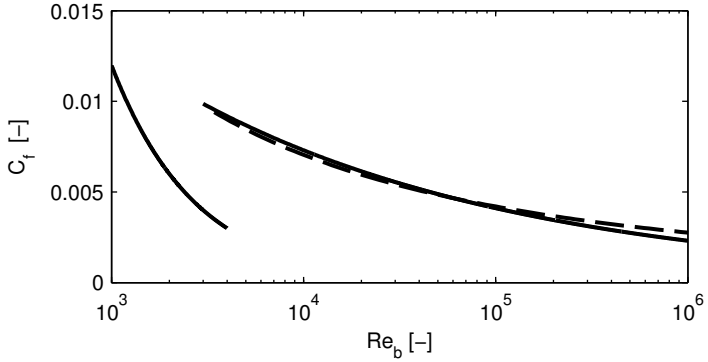

Figure 2.4: Skin-friction coefficient C_f against the bulk Reynolds number Re_b for a channel flow. Solid lines: laminar solution $C_f = 12/Re_b$ for $Re_b < 4000$ and the correlation $C_f = 0.073 Re_b^{-0.25}$ by Dean [39], based on experimental data of turbulent channel flows with different aspect ratios; dashed line: the friction law of Eq. 2.19.

The law of the wall can be used to determine the Reynolds number dependence of the skin-friction coefficient and eventually predict its value. This can be done by establishing relationship among u_τ, U_c and U_b.

A good estimate of the bulk velocity is obtained by integrating Equation 2.14 over the whole channel and assuming $B_1 = 0$ for consistency. The result yields:

$$\frac{U_c - U_b}{u_\tau} = \frac{1}{\kappa} \tag{2.18}$$

When the log-law in the inner layer (Equation 2.14) and in the defect layer (Equation 2.13) are added together, the y dependence vanishes to yield:

$$\frac{U_c}{u_\tau} = \frac{1}{\kappa} \ln\left[Re_c \frac{u_\tau}{u_c} \right] + B + B_1 \tag{2.19}$$

which can be solved for U_c/u_τ for a given Re_c to determine c_f, which, together with Equation 2.18, allows Re_b and C_f to be computed.

Figure 2.4 compares the skin friction coefficient C_f, obtained from Equation 2.19 (dashed line), to the empirical correlation $C_f = 0.073 Re_b^{-1/4}$ proposed by Dean [39] and based on various experimental results. The fairly

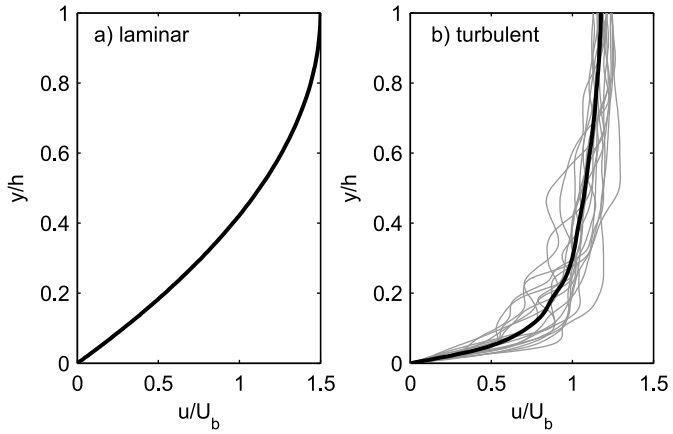

Figure 2.5: (a) laminar and (b) turbulent velocity profiles up to the channel semi-height. Both turbulent local and instantaneous profiles (gray lines) and averaged profile (black line) are represented.

good agreement confirms the validity of the hypothesis underlying Equations 2.18 and 2.19.

2.1.2 Turbulent drag

The higher mixing and unsteadiness associated with velocity fluctuations of turbulent flows leads to higher skin-friction. In Figure 2.5 a laminar and a turbulent velocity profile in channel flows at the same flow rate are compared. Instantaneous, local velocity profiles are also represented for the turbulent case and show high fluctuations from the mean velocity profile.

It is clear from Section 2.1.1, that the total mean streamwise shear stress $\tau(y)$ is made up of viscous shear stresses $\rho\nu\frac{\mathrm{d}\langle u\rangle}{\mathrm{d}y}$ and Reynolds shear stresses $-\rho\langle u'v'\rangle$, which just depends on u' and v' fluctuations. The relation between the turbulent Reynolds shear stresses and the higher skin-friction of turbulent flows has been derived by Fukagata *et al.* [48].

If the flow is driven throughout the channel at constant flow rate, the

skin friction can be expressed as:

$$C_f = \underbrace{\frac{12}{Re_b}}_{laminar} \underbrace{- 24 \int_0^1 (1-y) \langle u'v' \rangle \, \mathrm{d}y}_{turbulent} \tag{2.20}$$

where all quantities are normalized by the channel semi-height h and twice the bulk velocity $2U_b$. The skin friction is composed of two terms: the first corresponds to the skin friction of a laminar flow with the same flow rate; the second is the excess turbulent friction, which is proportional to the weighted integral of the Reynolds stresses $-(1-y)\langle u'v' \rangle$. The weight $(1-y)$ indicates that Reynolds stresses in the vicinity of the wall have an higher impact on skin friction than away from it.

Marusic *et al.* [104] found an analogous expression, valid for a channel flow driven at constant pressure gradient, which corresponds to imposing the mean streamwise wall shear τ_x (Equation 2.6), hence u_τ and Re_τ. In this case, the turbulent flow exhibits a lower flow rate with respect to its laminar counterpart with the same mean wall shear stress, as follows:

$$U_b = \underbrace{\frac{Re_\tau}{3}}_{laminar} + \underbrace{\int_0^{Re_\tau} \left(1 - \frac{y}{Re_\tau}\right) \langle u'v' \rangle \, \mathrm{d}y}_{turbulent} \tag{2.21}$$

where all quantities are normalized by the friction velocity u_τ and kinematic viscosity ν. Once again, the laminar and turbulent contribution can be distinguished.

The streamwise and wall-normal fluctuations of wall-bounded turbulent flow are such that $-\langle u'v' \rangle$ is positive in the near wall region [82, 167], thus contributing an increasing wall shear (at constant flow rate, Equation 2.20) or decreasing the flow rate (at constant wall shear, Equation 2.21).

2.1.3 Near-wall structures

The high mean Reynolds stresses in the near-wall region are the statistical footprint of repeatable, characteristic and quasi-deterministic events or structures.

The local Reynolds shear stress product $u'v'$ can be classified into four quadrants depending on the signs of u' and v', as shown in Figure 2.6. Whenever the instantaneous, local $u'v'$ is stronger than a threshold, i.e. collocates away from the axes of the quadrant plot, an "event" is said to occur. Among them, events that occur in the second Q2 event correspond

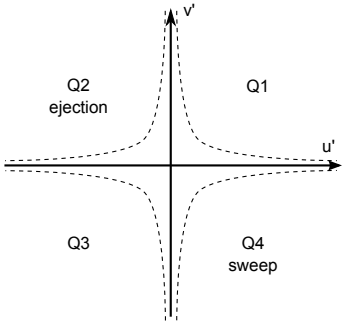

Figure 2.6: The $u'-v'$ event space showing the numbering of the four quadrant and the quadrant corresponding to ejections and sweeps. Events lying within the region bounded by the dashed lines, the so-called "hole", are not intense enough to be classified as ejections or sweeps.

to a low-speed fluid $u' < 0$ moving away from the wall $v' > 0$, i.e. ejection, while Q4 event correspond to high-speed flow $u' > 0$ moving towards the wall, i.e. sweep. The other quadrants are called the interaction modes, which correspond to Q1 ($u' > 0$ and $v' > 0$), the upward interaction, and to Q3 ($u' < 0$ and $v' < 0$), the downward interaction. Sweep and ejection events are prevalent [82, 100, 167] and their contribution to the average Reynolds shear stress $-\langle u'v'\rangle$ contributes to an increase of friction drag.

The consistency with which sweeps and ejections occur is a consequence of the existence of coherent structures in the wall-bounded turbulence. Whether it be a vortex, a region of coherent motion, or a shear layer, a coherent structure is a deterministic feature, immersed in a random background, that appears repeatedly in a specific region of the turbulent flow.

Several coherent structures have been conjectured [159], observed [19, 83] and studied [1] in turbulent wall-bounded flows, many of them listed by Robinson [140]. In what Jeong *et al.* [68] defined as a zoo of proposed structures, an agreed upon set of main protagonists has been identified to be responsible for strong turbulent production $-\langle u'v'\rangle \frac{\mathrm{d}\langle u\rangle}{\mathrm{d}y}$ in the viscous layer, and for the observed ejection, or bursting, phenomena. They are the low speed streaks (LSS) and the quasi streamwise vortex (QSV).

The quasi streamwise vortex is an elongated vortical structure, analyzed in detail by Jeong *et al.* [68], although its existence has been suggested also previously [18, 140]. It is elongated in the streamwise direction, lies

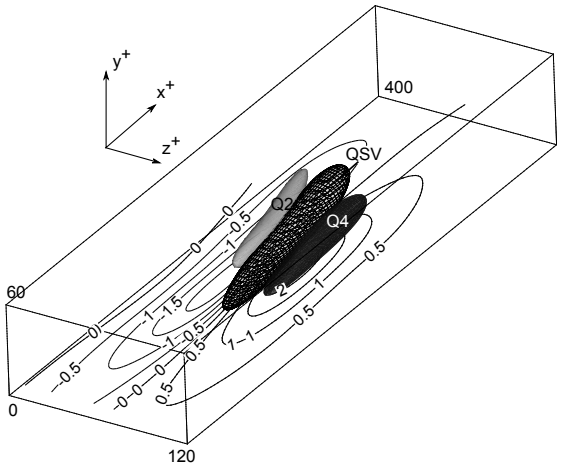

Figure 2.7: A mean, conditionally averaged quasi streamwise vortex (QSV); educed from a numerical simulation of a low-Re turbulent channel flow with the procedure described by Jeong *et al.* [68]. Wireframe: conditional QSV with $\omega_x > 0$; light gray: region of strong Q2 event; dark gray: region of strong Q4 events; solid lines: contour of conditionally-averaged streamwise velocity at $y^+ = 10$.

just above the wall, starting at the uppermost part of the buffer layer and eventually protrudes into the bulk of the flow. It is slightly tilted in both the x-z and x-y planes and therefore stretched by the mean shear [68]. The strong streamwise vorticity induces both high- and low-speed streaks at their sides, by pulling up low-speed fluid from the near-wall region towards the channel at one side, and pushing higher energetic flow from the bulk towards the channel walls at the other. As a result, two regions of high Q2 and Q4 are located along the vortex. A QSV is generally associated with a low speed streak, located along the suction side of the vortex. An average quasi streamwise vortex, together with its associated regions of Q2 and Q4 events is represented in Figure 2.7, obtained numerically with a vortex eduction procedure proposed by Jeong *et al.* [68]. Underneath the vortex, two regions of positive and negative velocity fluctuations can be observed.

The interaction of LSS and QSV, together with the effect of the mean shear are the foundation of the so-called near-wall, autonomous, turbulence regeneration cycle [70], in which near-wall turbulence is continuously

regenerated and sustained in a cyclical process. The cycle starts with a quasi streamwise vortex that generates low speed streaks at the lifting side of the vortex, where it lifts low speed flow upwards. The low speed streak grows linearly in time until it becomes unstable and an additional blob of vorticity is produced, which give rise to further QSVs.

This main, self-sustained, turbulent generation process has been observed to persistently occur in the viscous layer and constitutes therefore an important mechanism of turbulence sustainability. However, it is not the only mechanism. Other regeneration cycle may coexist, especially in high Reynolds number flows, where other large-scale motions occur [50, 65, 105], which are observed to interact with the near-wall region.

2.1.4 Turbulent drag reduction

The manipulation of a turbulent flow, aimed at reducing its excess turbulent drag gained a very relevant position in modern fluid mechanics thanks to the potential technological achievements and to the challenging understanding of turbulent momentum transfer phenomena near the wall [28, 49, 76, 154].

Classification

Several strategies can be adopted to control a flow and, in particular, to control a turbulent flow for reducing its drag. A tentative classification has been proposed by Gad-el-Hak [49], based on the energy expenditure and complexity of the involved control loop (Figure 2.8).

Firstly, passive and active flow control techniques are distinguished. A passive control device requires neither auxiliary power nor a control loop, a classic example being riblets [52], structured surfaces that yield up to 8–10% reduction of skin friction in well controlled, low-Reynolds laboratory conditions and have been estimated to yield reductions of total aerodynamic drag of at least 2% in flight conditions [164].

Active control strategies are further classified according to the complexity of their control loop. Predetermined control includes the application of steady or unsteady energy input regardless the actual state of the flow. A control loop is said to be open, if no sensing of any flow quantity is required. In reactive control strategies, the control action is continuously adjusted according to the state of the flow, requiring the knowledge of certain local and instantaneous flow quantities through sensing.

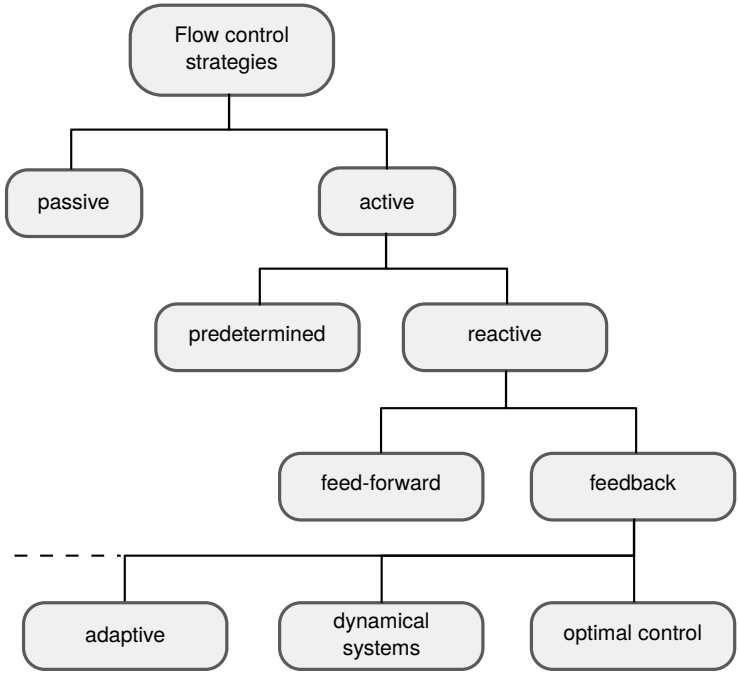

Figure 2.8: Classification of control strategies according to Gad-el-Hak [49]

A reactive control strategy is feed-forward if measured and controlled variables differ. A typical example concerning stationary convection is the sensing of a variable at an upstream position which triggers the action of an actuator placed downstream. In feedback control, the measured and controlled variable coincide, and the control action is aimed at reducing the difference between the measured variable and a reference desired value. How the measured state is used to determine the control action determines the further classification of feedback control techniques and many different examples exist [67, 79, 95, 96].

Performance indicators

The control performance is evaluated, according to the notation introduced by Kasagi *et al.* [75], in terms of three dimensionless indicators (R, S, G). R is the drag reduction rate, equivalent to the relative reduction of pumping power P per unit channel area:

$$R = \frac{P_0 - P}{P_0}, \tag{2.22}$$

where the subscript 0 refers to the uncontrolled flow.

The control goal for active control techniques, which require a power consumption P_{in} to manipulate the flow, is to obtain a positive net power saving S. It is defined as the budget between the saving and expenditure consequent to the control imposition as follows:

$$S = R - \frac{P_{\text{in}}}{P_0} \tag{2.23}$$

Another important parameter for is the effectiveness of a control algorithm, i.e. the gain G defined as:

$$G = \frac{P_0 - P}{P_{\text{in}}} \tag{2.24}$$

which represents the power saved per unit input power.

Clearly, in passive techniques, for which $P_{\text{in}} = 0$, the net power saving S is equivalent to the drag reduction rate R and drag reduction always results in power saving.

2.1.5 Spanwise wall oscillations

Prompted by the evidence that the most important turbulence production mechanisms occur close to the wall of a wall-bounded turbulent flow, most techniques aimed at reducing the skin-fricition, either actively or passively, reside at the wall, where structured surfaces or actuating devices can be installed.

Spanwise wall movements are an active technique that yield sizable drag reduction with the advantage of moderate complexity, as they do not need sensors and only require relatively large-scale actuators. Since the numerical experiment by Jung *et al.* [72], cyclic surface motions in the spanwise direction are known to significantly alter wall-bounded turbulent flows, either

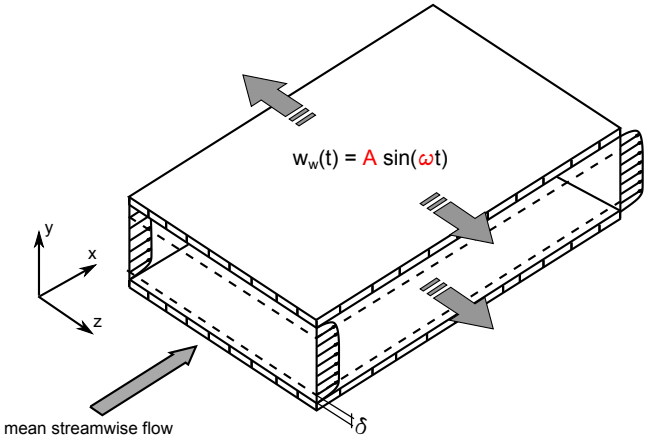

Figure 2.9: Sketch of a channel flow with spanwise oscillating walls.

in internal or in external geometries. The most interesting and practically appealing effect of the oscillating wall on turbulent flows is the significant reduction of the mean streamwise wall friction [130].

The spanwise, in-plane, oscillatory motion of a surface is tantamount to the imposition of a periodic spanwise wall velocity w_w:

$$w_w(t) = A \sin\left(\frac{2\pi}{T} t\right) \tag{2.25}$$

where $T = 2\pi/\omega$ and A are the period and amplitude of wall oscillation, ω is its angular frequency and t is time.

The first consequence of the spanwise wall motion is the creation of a spanwise cross-flow, the so-called Stokes layer, confined within a distance δ from the wall, which is described by the laminar solution of the second Stokes problem [146]:

$$w(y,t) = A \exp\left(-y\sqrt{\frac{\pi}{T\nu}}\right) \sin\left(\frac{2\pi}{T} t - y\sqrt{\frac{\pi}{T\nu}}\right) \tag{2.26}$$

The interaction between the spanwise Stokes layer and the near-wall turbulence can be favorable, only if the induced cross-flow is itself laminar, though superimposed on the turbulent background of the main flow. Vittori

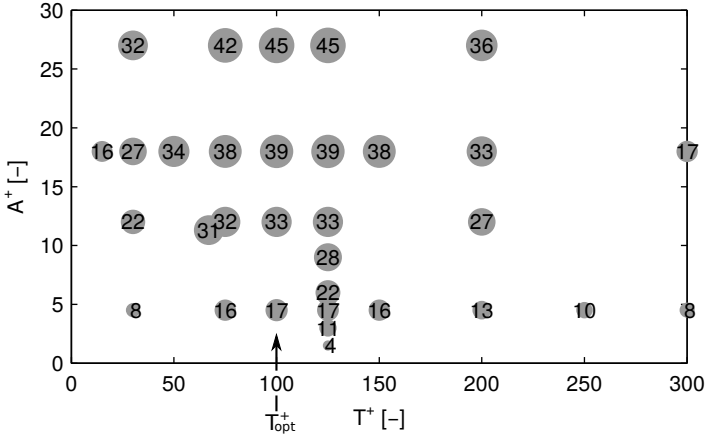

Figure 2.10: Map of the percent drag reduction $100R$ versus amplitude A^+ and period T^+ of wall oscillation. The size of the circle is proportional to the drag reduction indicated by the numbers. Adapted from Quadrio & Ricco [130].

& Verzicco [165] found that this condition is verified if the Reynolds number $Re_\delta = \frac{A\delta}{\nu}$ based on oscillation amplitude and the Stokes layer thickness is below 120. This condition is always fulfilled by spanwise wall oscillations that potentially lead to drag reduction. In fact, the phase-averaged spanwise velocity profile is found to be practically unaffected by the main turbulent flow in which it resides [30].

The most complete survey on the effect of spanwise wall oscillations at various amplitude and frequency on the skin-friction in a low-Re turbulent channel flow has been made by Quadrio & Ricco [130], with direct numerical simulations (DNS). Figure 2.10 shows the attainable percent drag reduction $100R$ versus the two oscillation parameters of Equation 2.25. It is found that an optimal period of oscillation exists and corresponds to $T^+_{\mathrm{opt}} = 100 \div 120$. It depends very mildly on the oscillation amplitude, being lower for lower A^+. Subsequently T^+ and A^+ are the period and amplitude of wall oscillation nondimensionalized with the friction velocity of the unmanipulated flow, and the kinematic viscosity.

Another important finding of Quadrio & Ricco [130] regards the theoretical maximum attainable power saving, computed by considering only

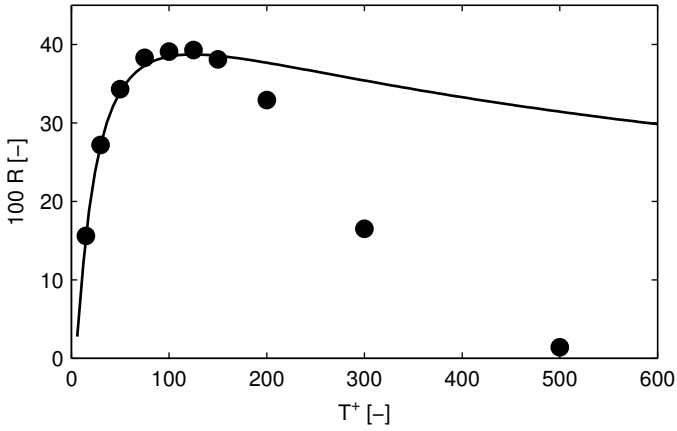

Figure 2.11: Percent drag reduction $1000R$ versus period of wall oscillation for a wall oscillating at amplitude $A^+ = 18$. Filled circles: data by Quadrio & Ricco [130]; solid line: empirical correlation $131S^+$ - 2.7.

the power required to overcome the spanwise wall shear stresses. A maximum power saving of 7.3% can be attained with oscillations at $T^+ = 120$ at the somewhat low oscillation amplitude of $A^+ = 4.5$. This means that the oscillation parameters which yield maximum net power saving $S_{\max}$ and maximum drag reduction $R_{\max}$ do not coincide.

The relative simplicity of spanwise wall oscillation opposed to the complicate interactions occurring in the near-wall turbulence made spanwise oscillation a very useful model tool to improve the understanding of drag reduction mechanisms. In spite of the huge number of numerical (some relevant examples are [11, 30, 44, 129, 130, 133, 138, 160, 169]) and some experimental [32, 34, 41, 58, 139, 163] investigation produced in the last twenty years, only recently more consensus has been achieved on the main mechanisms leading to drag reduction. The literature on the subject is by far too large to be comprehensively reviewed here and only studies that point out quantitative correlations between drag reduction and the control parameters or properties of the Stokes layer and near-wall turbulence are mentioned.

J.-I. Choi *et al.* [30], starting from the Stokes solution Equation 2.26, constructed a scaling parameter S^+ by combining a wall-normal length

scale ℓ^+, related to the distance at which the wall oscillation affects the turbulent structures, and a local spanwise acceleration a_m^+ of the Stokes layer. The critical length scale, representative of the penetration depth of the Stokes layer into the turbulent flow, is identified by the requirement that the maximum oscillating velocity at a distance $y^+ = \ell^+$ from the wall has a magnitude higher than a threshold velocity A_{th}^+, representing a typical value of the spanwise turbulent fluctuations. The maximum acceleration a_m^+ is evaluated at a given wall-normal height $\overline{y}^+$, chosen according to physically based heuristic arguments [30].

$$S^+ = \frac{a_m^+ \ell^+}{A^+} = 2\sqrt{\frac{\pi}{T^+}} \ln\left(\frac{A^+}{A_{th}^+}\right) \exp\left(-\overline{y}^+ \sqrt{\pi/T^+}\right) \tag{2.27}$$

Quadrio & Ricco [130] found that the parameter S^+ correlates with R according to the following linear correlation:

$$R = 1.31 S^+ - 0.027 \tag{2.28}$$

Two main aspects are implicit in the definition of the parameter S^+. First, the spanwise Stokes layer can affect turbulence only if its thickness is such that interaction with near-wall events taking place above the viscous sublayer can occur. Then, interaction occurs due to the spanwise acceleration induced in the same region. From the viewpoint of the control parameters, the smaller T becomes the thinner the Stokes layer is, which then does not have time to diffuse into the flow. Therefore, large T should affect a larger portion of near-wall turbulence, thanks to the thicker Stokes layer. However, the larger T, the smaller is the acceleration (unsteadiness) within the Stokes layer, and consequently also the effect of wall oscillations. The trade-off between Stokes layer thickness and unsteadiness could explain the existence of the optimal T at fixed A.

Equation 2.28 correlates with drag reduction measurements (Figure 2.11) only up the optimal period, well predicting its position but fails beyond T_{opt}^+ [130], suggesting that other or additional phenomena might occur at large T^+

Bandyopadhyay [9] proposed a correlation based on the effect of the Stokes layer on the near-wall turbulence. The central idea is that the Stokes layer cyclically re-orients the near-wall vorticity and that the drag reduction is linearly related to the sine of the maximum angle of vorticity re-alignment with respect to the streamwise direction.

Ricco *et al.* [137] and Touber & Leschziner [160] were the first to stress the importance of the induced spanwise shear within the Stokes layer for

the achievement of drag reduction. The former found a linear correlation between the drag reduction and the volume integral of enstrophy (a quantity whose volume integral is identical to turbulent dissipation) production term, which explicitly contains the spanwise shear. Also this correlation predicts the drag reduction only up to T^+_{opt}. The latter states that the drag reduction effect is determined by the magnitude of the spanwise shear relative to the streamwise shear in the viscous sublayer. They also observed that the LSS reorientation that takes place near the wall under the Stokes spanwise strain is related to drag reduction. When the Stokes spanwise stress changes rapidly, the streaks have no time to readjust their orientation to the new state and they weaken dramatically. They also found that the streak tilt angle in the x-z plane has high wall-normal coherence and is strictly related to the shear angle at $y^+ = 10$, where the shear angle is the angle between the resultant of the streamwise and spanwise shear with the x-direction.

In 2014, Yakeno *et al.* [169] offered an explanation for the existence of the optimal period and proposed a linear correlation that predicts the drag reduction beyond T^+_{opt} reasonably well. They adopted a conditional averaging procedure to observe the properties of mean quasi streamwise (similar to what done in Figure 2.7) vortices at specific phases of oscillation, focusing on the phase variation of Q2 and Q4 events, which determine the Reynolds stress, at the sides of the QSV induced by the spanwise oscillation. When the spanwise shear is large at $y^+ = 10$ and locally counteracts the rotation of the downward part of a QSV, Q2 events are strongly reduced, resulting in drag reduction. Moreover, the tilting of QSV is also found to cause drag reduction. When the wall motion coincides with the vortical motion in the downward part of a QSV, drag is reduced. However, at large T^+ the spanwise tilting of QSV in the x-z plane, well correlated with the shear angle at $y^+ = 15$, may become too large generating a nonlinear self-induced vortex stretching which results in enhancements of Q4 events. This causes an increase of Reynolds stresses, hence drag. Based on this model of near-wall interaction, the following correlation has been proposed:

$$\Delta U_b = c_1 \left(\left. \frac{\mathrm{d}\tilde{w}}{\mathrm{d}y} \right|_{y^+=10} \right)_{\mathrm{rms}} - c_2 \left(\left. \frac{\mathrm{d}\tilde{w}}{\mathrm{d}y} \right|_{y^+=15} \right)_{\mathrm{rms}} \tag{2.29}$$

where $\tilde{w}$ is the phase-averaged spanwise velocity, eventually computed with the laminar Stokes solution of Equation 2.26, and $(\cdot)_{\mathrm{rms}}$ indicates the r.m.s. over one period of oscillation. c_1 and c_2 are two empirical coefficients, while ΔU_b is the increase of U_b due to the application of the control. In fact,

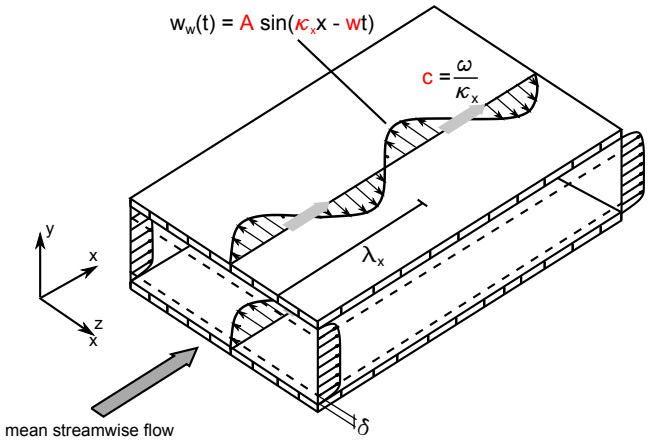

Figure 2.12: Sketch of a channel flow with imposed streamwise-traveling waves of spanwise wall velocity.

Yakeno *et al.* [169] ran a simulation at constant pressure gradient, where the mean friction drag is then imposed a priori. Within this framework, the imposition of the control results in an increase of flow rate at constant mean streamwise wall shear, which also implies a reduction of C_f.

2.1.6 Traveling waves of spanwise wall velocity

The streamwise traveling waves of spanwise wall velocity are a promising generalization of the spanwise wall oscillations (Equation 2.25) and have been first discovered to yield sizable drag reduction and high net power saving rates by Quadrio *et al.* [132]. A streamwise-modulated, time-dependent spanwise wall velocity is imposed at the wall, according to the following:

$$w_w = A \sin(\kappa_x x - \omega t) \tag{2.30}$$

where A is the oscillation amplitude, $\kappa_x = 2\pi/\lambda_x$ is the streamwise wavenumber and λ and $\omega = 2\pi/T$ is the angular frequency, which respectively define the streamwise wavelength λ_x and the oscillation period T.

The spanwise wall forcing of Equation 2.30 results in the wall movement sketched in Figure 2.12. At a given instant in time, the spanwise velocity at the wall is a streamwise modulated wave of wavelength λ_x and amplitude

A. The wave moves in time with phase speed $c = \omega/\kappa_x$, either forward ($c > 0$) or backward ($c < 0$) according to the sign of c. Therefore, in this case it is allowed to consider negative frequencies ω, which correspond to backward-traveling waves.

It is worth noting that Equation 2.30 reduces to the spanwise oscillating wall if the streamwise wavenumber κ_x is zero.

As for the spanwise oscillations, also the streamwise traveling waves of spanwise wall velocity generate a thin cross-flow confined within a distance δ from the wall, called generalized Stokes layer (GSL), which is modulated in the streamwise direction and time. Quadrio & Ricco [131] found the following analytical solution for the laminar GSL, written in nondimensional viscous variables for compactness:

$$w_w\left(x^+, y^+, t^+\right) = A^+\left\{Ce^{i\left(\kappa_x^+ x^+ - \omega^+ t^+\right)}\mathrm{Ai}\left[e^{\pi i/6}\left(\kappa_x^+\right)^{1/3}\left(y^+ - \frac{\omega^+}{\kappa_x^+} - i\kappa_x^+\right)\right]\right\} \tag{2.31}$$

where i is the imaginary unit, Ai is the Airy function of the first kind and $C = \left\{\mathrm{Ai}\left[\mathrm{i}e^{i\pi/3}(\kappa_x^+)^{1/3}(\omega^+/\kappa_x^+ + \mathrm{i}\kappa_x^+)\right]\right\}^{-1}$ is a constant.

The laminar solution of equation 2.31 has been found [131] to hold also in turbulent flows provided that:

$$\frac{\lambda_x^+}{c_w^+ - c^+} \leq 120 \tag{2.32}$$

where $c_w^+ \approx 10$ is the convection velocity of near-wall turbulent skin-friction fluctuations [127].

Quadrio *et al.* [132] tested the traveling waves using DNS of fully developed, low-Re, channel flows driven at constant flow rate. Figure 2.13 describes the effects of the traveling waves in terms of percentage drag reduction rate R as a function of ω^+ and κ_x^+ at $A^+ = 12$. The phase speed c^+ is interpreted graphically as the inverse of the slope of straight lines passing through the origin. In the first quadrant, the waves move forward in the direction of the mean flow, while the second quadrant corresponds to backward-traveling waves. The flow response reveals an unexpectedly rich behavior.

The contours show that local maxima and local minima form two elongated narrow regions. In the red region, whose crest identifies a curve which does not cross the origin, the flow presents an intense DR. The maximum is about 48%, which is higher than 34% for the best-performing wall oscillations at the same A^+. The blue region identifies a region of finite

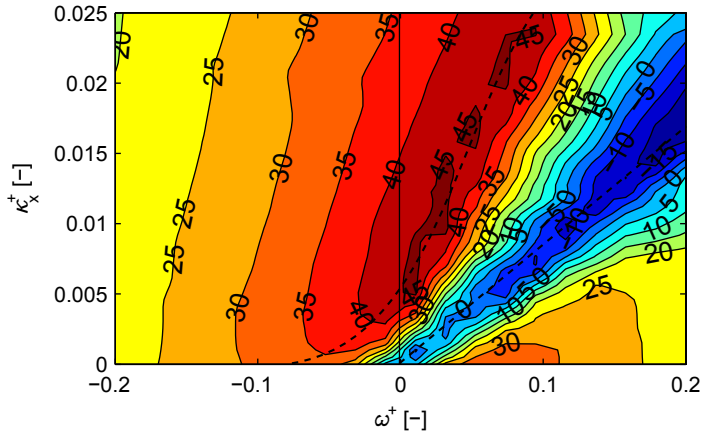

Figure 2.13: Map of percent drag reduction $100R$ as function of the wavenumber $\kappa_x^+ = 2\pi/\lambda_x^+$ and angular frequency ω^+ of the waves. The dashed lines indicate the loci of maximum and minimum drag reduction.

drag increase (DI). Straight and elongated, it is centered about the line at constant wavespeed $c^+ = 10$, which interestingly corresponds to the value of the convection velocity c_w^+. Indeed, when $c^+ = c_w^+$ a sort of phase lock occurs between the near-wall flow structures and the wall waves, which travel downstream at the same (mean) phase speed. The region of DI is the region where the laminar GSL solution of Equation 2.31 ceases to hold, as the one-way is lost and the turbulent flow deforms the spanwise GSL.

The most appealing feature of traveling waves is their very high maximum theoretical net power saving sate S of 26% [132], more than three times higher than the 7% enabled by the oscillating wall. Such high savings are possible since the set of (κ_x^+, ω) which yields the maximum drag reduction requires also the minimum energy expenditure to impose the wall velocity waves.

Auteri *et al.* [8] provide experimental verification of the streamwise traveling waves in a laboratory pipe flow, in which the wave is reproduced by subdividing the wall into thin segments that rotate independently in the azimuthal direction. Reductions up to 33% are observed for control parameters and Re similar to those of the reference DNS by Quadrio *et al.* [132].

The pipe flow being a generalization of the channel flow, the mechanism

with which the streamwise-traveling waves affect near-wall turbulence must be similar to that of the oscillating wall, possibly with additional effects due to the spatial inhomogeneity of the forcing. However, the rationale behind the improved performance of the traveling waves is unknown and only few studies attempted to explain it. The comprehension of the mechanisms with which a thin spanwise unsteady boundary layer interacts with near-wall turbulence to yield drag reduction is of paramount importance to enable the prediction and design of optimal control strategy.

Among the few attempts, Quadrio & Ricco [131] find that drag reduction correlates well with the thickness of the laminar generalized Stokes layer for forcing conditions that verify the condition 2.32 and an optimal thickness δ_{opt} is found. However, multiple combinations of control parameters exist, that yield the same δ but of different values of R, which means that $\delta = \delta_{\text{opt}}$ is a necessary but not sufficient condition for high drag reduction.

Duque-Daza *et al.* [44] use linearized Navier-Stokes equations to investigate streak growth characteristics in the presence of streamwise-traveling waves. The map of streak amplification against the control parameters κ_x and ω strongly resemble the map of drag reduction of Figure 2.13, yet with some important differences. Therefore, even though the linear LSS amplification and lift-up process is surely related to drag reduction, other, possibly nonlinear interactions take place between the GSL and near-wall turbulence.

2.2 Dielectric elastomer actuators

Electroactive polymers (EAP) are particular polymers that react to an electric stimulus, as an electric field or a current flux, with a change of their shape or of their optical, magnetic or dielectric properties. A particular subclass of electroactive polymers, called dielectric elastomer actuators (DEAs), respond to an electric field with an active deformation. The field-induced deformation of a dielectric undergoing an high electric field, already observed by Röntgen [141], has been proposed in [115] as an efficient and versatile means of actuation and, more general, energy transduction.

The following Sections are devoted to a fundamental description of the working principle of DEA. A brief description of the main actuator configurations is given, focusing on the attempts to exploit DEA for aeronautical applications.

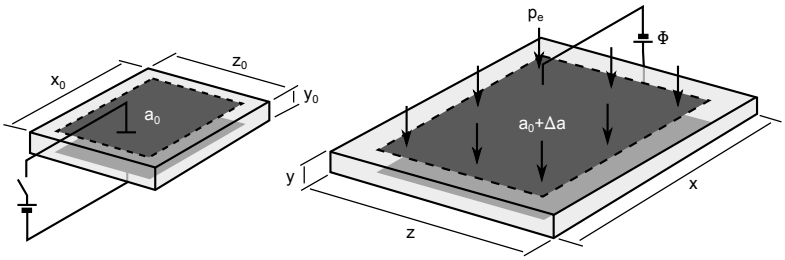

Figure 2.14: Dielectric elastomer actuator before (left) and after (right) imposition of a voltage difference between the electrodes.

2.2.1 Working principle

The basic working principle of a DEA [115, 119], sketched in Figure 2.14, conceptually corresponds to a deformable capacitor. A highly deformable, ideally incompressible, elastomeric film - the dielectric medium - is sandwiched between two electrically conductive, compliant electrodes. When an electric field is applied across the dielectric, the electrodes attract each other and exert a pressure, called the Maxwell pressure, on the underlying dielectric. The pressure causes a thinning of the dielectric and a consequent expansion of its area, to preserve incompressibility of the elastomer.

In spite of the apparent simplicity of the actuation process, the DEA is a complex thermodynamic system [157] capable of converting electrical energy into mechanical energy and vice versa [118]. However, a simplified description of a DEA which explains its main features can be obtained, provided few hypotheses are made. In the following, the DEA of Figure 2.14 is assumed perfectly elastic, free to move and its boundaries are mechanically unconstrained. The electrodes are connected to a supply which delivers a constant voltage difference Φ, causing a change dy of the elastomer thickness.

Electrostatic pressure The total energy of the system U_{tot}, i.e. the sum of mechanical U_{m}, electrical U_{e} and supply U_{s} energy, is conserved:

$$\mathrm{d}U_{\mathrm{tot}} = \mathrm{d}\left(U_{\mathrm{m}} + U_{\mathrm{e}} + U_{\mathrm{s}}\right) = \mathrm{d}U_{\mathrm{m}} + \mathrm{d}U_{\mathrm{e}} + \mathrm{d}U_{\mathrm{s}} \tag{2.33}$$

The variation of the mechanical energy is the work performed by the electrostatic force F_e along the displacement $\mathrm{d}y$:

$$\mathrm{d}U_\mathrm{m} = F_e \mathrm{d}y \tag{2.34}$$

The electric energy U_e is given by:

$$U_\mathrm{e} = \frac{1}{2}\Phi^2 C \tag{2.35}$$

where C [F] is the capacitance of the compliant capacitor. A variation of the electric energy at constant voltage is only caused by changes of C, hence:

$$\mathrm{d}U_\mathrm{e} = \frac{1}{2}\Phi^2 \mathrm{d}C \tag{2.36}$$

The change in capacitance $\mathrm{d}C$ requires the supply to deliver additional charge $\mathrm{d}Q$ [C], since the charge Q and the capacitance C are related by $Q = C\Phi$. Therefore, the following amount of energy needs to be drawn from the supply:

$$\mathrm{d}U_\mathrm{s} = -\Phi i \mathrm{d}t = -\Phi \mathrm{d}Q = -\Phi^2 \mathrm{d}C \tag{2.37}$$

where i [A] is the current delivered during the time span $\mathrm{d}t$. By substituting Equations 2.34, 2.36 and 2.37 into Equation 2.33 one obtains a direct relation between the electrostatic force and the change of capacitance:

$$F_e \mathrm{d}y = \frac{1}{2}\Phi^2 \mathrm{d}C \tag{2.38}$$

If we consider the actuator of Figure 2.14 to be a parallel capacitor, its capacitance can be expressed as:

$$C = \epsilon_0 \epsilon_r \frac{a}{y} \tag{2.39}$$

where a is the area, y the thickness of the elastomer, ϵ_0 is the vacuum permittivity (8.85×10^{-12} F/m) and ϵ_r is the dielectric constant. As the elastomer is ideally incompressible, an expansion of its area corresponds to a thinning of the elastomer, so as to keep the volume constant, as follows:

$$a_0 y_0 = a y = \text{const} \quad \Longrightarrow \quad a = \frac{a_0 y_0}{y} \tag{2.40}$$

a_0 and y_0 being the area and thickness of the elastomer at rest. Combining equation 2.40, 2.39 and 2.38 yields:

$$F_e \mathrm{d}y = \frac{1}{2}\epsilon_0 \epsilon_r a_0 y_0 \Phi^2 \mathrm{d}\left(\frac{1}{y^2}\right) \tag{2.41}$$

Finally, differentiating yields an equation for the electrostatic force F_e as a function of the applied voltage Φ and the geometrical and electrical properties of the actuator, namely:

$$\begin{aligned} F_e &= \frac{1}{2}\epsilon_0\epsilon_r a_0 y_0 \Phi^2 \frac{\mathrm{d}}{\mathrm{d}y}\left(\frac{1}{y^2}\right) \\ &= -\epsilon_0\epsilon_r a_0 \left(\frac{y_0}{y^3}\right)\Phi^2 \end{aligned} \tag{2.42}$$

which is negative, meaning that the electrostatic force is compressive and increases with the thickness y of the dielectric decreases. The (compressive) electrostatic pressure is readily derived, based upon its definition, as:

$$p_e = -\frac{F_e}{a} = \epsilon_0\epsilon_r \left(\frac{\Phi}{y}\right)^2 \tag{2.43}$$

which is twice the pressure generated by a parallel plate capacitor with conventional stiff electrodes.

Active strain If the electrostatic pressure of Equation 2.43 is balanced by the elastic stress of the elastomer, the thickness strain $s_y = (y/y_0) - 1 = \Delta y/y_0$ can be written as:

$$s_y = -\frac{p_e}{Y} = \frac{\epsilon_0\epsilon_r}{Y}\left(\frac{\Phi}{y}\right)^2 \tag{2.44}$$

where Y [Pa] is the Young's elastic modulus of the elastomer. The equation can be solved for the strain s_y, recalling that $y = y_0\,(1 + s_y)$:

$$s_y\,(1 + s_y)^2 = \frac{\epsilon_0\epsilon_r}{Y}\left(\frac{\Phi}{y_0}\right)^2 \tag{2.45}$$

This cubic equation can be further simplified under the additional hypothesis of small strains, for which $(1 + s_y)^2 \approx 1$, to yield:

$$s_y = \frac{\epsilon_0\epsilon_r}{Y}\left(\frac{\Phi}{y_0}\right)^2 \tag{2.46}$$

which depends now on the initial thickness y_0 only. The approximate Equation 2.46 holds for active strains up to about 15%, which is within the operative range of many dielectric elastomer actuators [25, 119].

In order to compute the active strain in the two other perpendicular directions, the incompressibility constraint of Equation 2.40 needs to be rearranged in terms of strains, to obtain:

$$(1 + s_x)(1 + s_y)(1 + s_z) = 1 \tag{2.47}$$

Equation 2.47 can be solved for the unconstrained case of Figure 2.14, where $s_x = s_z = s$ by symmetry, and yields:

$$s = \frac{1}{\sqrt{1 + s_y}} - 1 \tag{2.48}$$

The simplified framework described by equations 2.43, 2.45 and 2.46 already contains some interesting features of dielectric elastomer actuators:

- the electrostatic pressure p_e is proportional to $E^2 = (\Phi/y)^2$, where E [V/m] is the electric field strength;
- the maximum achievable p_e is limited by the dielectric breakdown field strength E_B, the maximum electric field strength that the dielectric can withstand without breaking down;
- a higher dielectric constant ϵ_r results in higher p_e; hence, higher active strain s_y
- the lower the elastic modulus Y of the elastomer, the larger is the active strain at constant electrostatic pressure p_e;
- a maximum thickness strain exists, at which Equation 2.45 admits no physical solution. Beyond the maximum strain, the rapidly growing electrostatic pressure overcomes the elastic restoring stress, yielding a sudden drastic thinning of the elastomer, known as pull-in instability [122, 173]. The large deformation at constant voltage might thin the dielectric beyond its dielectric breakdown strength, causing failure of the actuator.

2.2.2 Actuators at large deformation

While it is useful to understand the main underlying mechanisms of dielectric elastomer actuators, some of the simplifying hypotheses made in the previous section are abandoned in the following, to obtain a more realistic description of a DEA, which will be exploited many times throughout the rest of the present work.

The dielectric elastomer is considered as an incompressible, isotropic, soft material which may undergo large deformations. As a result, the infinitesimal strain theory ceases to apply and the finite strain theory needs to be considered, in order to properly describe the nonlinear mechanics of the system.

Consider a cuboid actuator [85] as shown in Figure 2.15, with initial thickness y_0 and planar dimensions x_0 and z_0. A reference frame coinciding with the three principal directions is chosen. As a result, the projection of the stress tensor onto one endplane of the cuboid results in the normal stress component only, which is aligned with the direction normal to the endplane surface.

The stretch λ along the three principal directions describes the principal deformations of the initial cuboid shape as:

$$\lambda_x = \frac{x}{x_0} \qquad \lambda_y = \frac{y}{y_0} \qquad \lambda_z = \frac{z}{z_0} \tag{2.49}$$

The incompressibility constraint of Equation 2.47 can be here reformulated in terms of principal stretches as:

$$\lambda_x \lambda_y \lambda_z = 1 \tag{2.50}$$

which implies that given two principal stretches, the third automatically follows to satisfy incompressibility. The thickness stretch λ_y is chosen as dependent variable, i.e. $\lambda_y = (\lambda_x \lambda_z)^{-1}$.

The definition of stress is less obvious if non-infinitesimal deformations are present, since the initial and deformed configuration differ significantly.

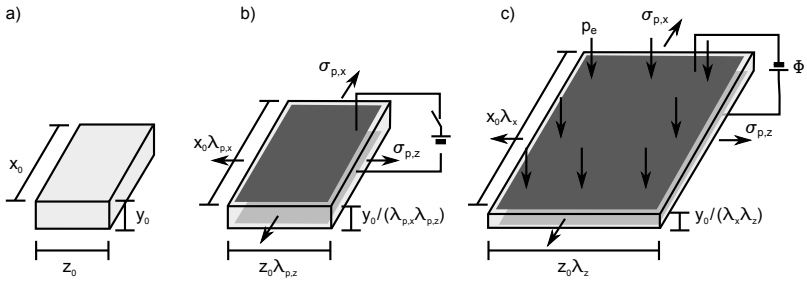

Figure 2.15: Dielectric elastomer cuboid actuator (a) before being pre-stretched, (b) after being pre-stretched and (c) upon actuation.

In an Eulerian framework, the three principal stresses are defined as:

$$s_x = \frac{F_x}{z_0 y_0} \qquad s_y = \frac{F_y}{x_0 z_0} \qquad s_z = \frac{F_z}{x_0 y_0} \tag{2.51}$$

where the principal load F is referenced to the initial, undeformed area of the cuboid. On the other hand, a Lagrangian approach is possible, in which the actual instantaneous area of the cuboid endplanes is used to compute the stresses, as follows:

$$\sigma_x = \frac{F_x}{zy} \qquad \sigma_y = \frac{F_y}{xz} \qquad \sigma_z = \frac{F_z}{xy} \tag{2.52}$$

To avoid confusion, the former are usually referred to as engineering stresses, the latter as true stresses. Hereinafter, stress refers to true stresses, unless otherwise stated.

The principal stress vector $\boldsymbol{\sigma}$, containing the three diagonal components of the stress tensor, is defined for an isotropic, incompressible cuboid as:

$$\boldsymbol{\sigma} = \begin{Bmatrix} \lambda_x \dfrac{\partial W}{\partial \lambda_x} \\ \lambda_y \dfrac{\partial W}{\partial \lambda_y} \\ \lambda_z \dfrac{\partial W}{\partial \lambda_z} \end{Bmatrix} - p\mathbb{I} \tag{2.53}$$

where $\mathbb{I}$ is the identity vector, p is an isostatic pressure and $W = W(\lambda_x, \lambda_y, \lambda_z)$ is the strain energy density function. In the present discussion, consider the strain energy density function as a scalar function of the three principal stretches which describes the hyperelastic behavior of the material. The interested reader can learn more about finite-strain elasticity in Treolar [161] and Basar & Weichert [12].

The real form of the strain energy density function is unknown and several phenomenological hyperelastic models, with different degrees of underlying physical considerations, have been proposed to tentatively describe the nonlinear stress/stretch behavior of hyperelastic materials. Comprehensive reviews of the main hyperelastic models suitable for modeling strain energy density functions of dielectric elastomers can be found in the literature [54, 111, 156]. In the present work, the Gent model [54] is preferred, thanks to its capability of reproducing well experimental properties of elastomers while reducing the number of empirical parameters to a minimum,

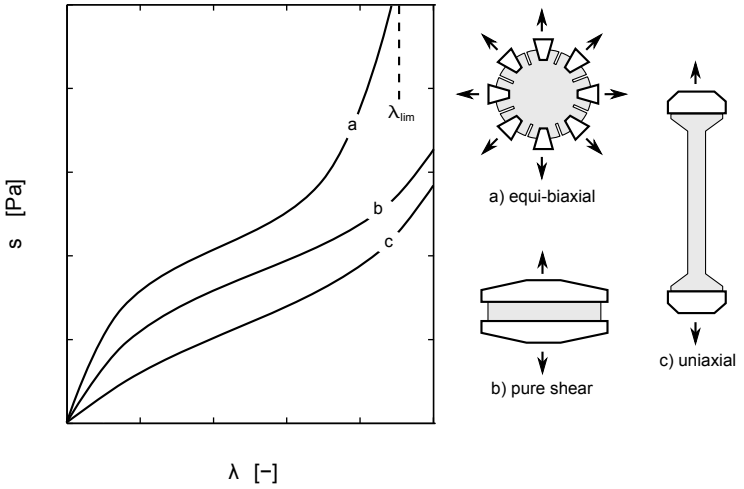

Figure 2.16: True-stress σ - stretch λ curve for three typical load conditions used to characterize hyperelastic materials. (a) equi-biaxial, (b) pure-shear and (c) uniaxial tensile tests.

which made it a common choice in the field of DEAs [3, 142]. The Gent strain energy function takes the following form:

$$W = -\frac{\mu_e J_m}{2} \ln\left(1 - \frac{\lambda_x^2 + \lambda_y^2 + \lambda_z^2 - 3}{J_m}\right) \tag{2.54}$$

where μ_e is the shear modulus and J_m is an empirical constant related to the limiting stretch of the elastomer.

Figure 2.16 sketches the typical engineering stress/stretch curves of an elastomer at the three load configurations that are needed to fully characterize its hyperelastic behavior. Typically, two inflection points are present. An initially linear behavior is followed by a decrease of the slope of the stress/stretch curve. At high stretches, a sudden stiffening of the polymer occurs. In fact, at small stretches, the polymer chains within the elastomer are loose, and the elastomer is compliant. At large stretches, the chains are taut, and the elastomer stiffens steeply. It must be noted that the apparent reduction of stiffness for fairly low stretches is mostly a geometrical

effect, which originates from the common habit of adopting the engineering stress to represent the stress/stretch curve [27]. The first inflection point disappears if true stresses are adopted, meaning that no physical softening in the elastomer occurs at low stretches.

Experimental stress/strain curves, as those sketched in Figure 2.16 are used to find the values of the two empirical coefficients of Equation 2.54 via a nonlinear least-square fitting procedure. The aim is to find the combination of parameters that best reproduces, in a least-square sense, the stress/strain characteristic of an elastomer. The three different, simple and reproducible load scenarios sketched in Figure 2.16 are usually considered in order to improve the predictive capability of the hyperelastic model in a broader range of stretches and more complex deformations.

Provided that the two empirical coefficients of the Gent strain energy density function have been determined experimentally, Equations 2.53 and 2.54 can be combined to yield, after differentiation:

$$\boldsymbol{\sigma} = 2\frac{\mu_e J_m}{J_m - \lambda_x^2 - \lambda_x^{-2}\lambda_z^{-2} - \lambda_z^2 + 3}\begin{Bmatrix} \lambda_x^2 \\ \lambda_x^{-2}\lambda_z^{-2} \\ \lambda_z^2 \end{Bmatrix} - p\mathbb{I} \tag{2.55}$$

The isostatic pressure p is determined by the boundary condition at the two electrode surfaces of the DEA. In fact, the second Equation of the system 2.55 reads:

$$\sigma_y = 2\frac{\mu_e J_m}{J_m - \lambda_x^2 - \lambda_x^{-2}\lambda_z^{-2} - \lambda_z^2 + 3}\lambda_x^{-2}\lambda_z^{-2} - p \tag{2.56}$$

where σ_y the stress at the top and bottom electrode surfaces may be either zero or opposite to the Maxwell pressure p_e. Moving the pressure p to the left-hand side and solving for the Maxwell pressure yields:

$$p = 2\frac{\mu_e J_m}{J_m - \lambda_x^2 - \lambda_x^{-2}\lambda_z^{-2} - \lambda_z^2 + 3}\lambda_x^{-2}\lambda_z^{-2} + p_e \tag{2.57}$$

The pressure p can now be inserted into Equation 2.55 as follows:

$$\begin{Bmatrix} \sigma_x \\ 0 \\ \sigma_z \end{Bmatrix} = 2\frac{\mu_e J_m}{J_m - \lambda_x^2 - \lambda_x^{-2}\lambda_z^{-2} - \lambda_z^2 + 3}\begin{Bmatrix} \lambda_x^2 - \lambda_x^{-2}\lambda_z^{-2} \\ \lambda_x^{-2}\lambda_z^{-2} \\ \lambda_z^2 - \lambda_x^{-2}\lambda_z^{-2} \end{Bmatrix} - p_e\mathbb{I} \tag{2.58}$$

σ_x and σ_z follow from the boundary condition of constant applied forces F_x and F_z, that impose the desired amount of pre-stretch, as:

$$\sigma_x = \frac{F_x}{yz} = \frac{F_x}{y_0 z_0 \lambda_y \lambda_z} = \sigma_{p,x}\frac{\lambda_{p,y}\lambda_{p,z}}{\lambda_y\lambda_z} \overset{Eq.2.50}{=} \sigma_{p,x}\frac{\lambda_x}{\lambda_{p,x}} \tag{2.59}$$

where $\sigma_{p,x}$ is the pre-stress required to impose the pre-stretch $\lambda_{p,x}$ at zero voltage. Analogous calculations can be carried out for σ_z to obtain:

$$\sigma_z = \sigma_{p,z} \frac{\lambda_z}{\lambda_{p,z}} \tag{2.60}$$

The governing system 2.58 is finally rewritten as:

$$\begin{aligned} &\epsilon_0 \epsilon_r \lambda_x^2 \lambda_z^2 \frac{\Phi^2}{y_0^2} \mathbb{I} = \\ &\frac{2\mu_e J_m}{J_m - \lambda_x^2 - \lambda_x^{-2}\lambda_z^{-2} - \lambda_z^2 + 3} \begin{Bmatrix} \lambda_x^2 - \lambda_x^{-2}\lambda_z^{-2} \\ \lambda_x^{-2}\lambda_z^{-2} \\ \lambda_z^2 - \lambda_x^{-2}\lambda_z^{-2} \end{Bmatrix} - \begin{Bmatrix} \sigma_{p,x}\lambda_x\lambda_{p,x}^{-1} \\ 0 \\ \sigma_{p,z}\lambda_z\lambda_{p,z}^{-1} \end{Bmatrix} \end{aligned} \tag{2.61}$$

and completely describes the hyperelastic deformation due to the imposition of a potential difference Φ between the electrodes of a pre-stretched cuboid elastomer.

2.2.3 Fundamental configurations

Thanks to the relatively simple working principle, dielectric elastomers are very versatile and can be the implemented in a large variety of devices, where the desired actuation is achieved by smartly coupling the DEA with proper kinematics. A review of the most interesting actuator configurations, in which DEAs are arranged in clever mechanisms, can be found in Anderson *et al.* [7], focusing on soft robotics, or in a dedicated volume [26]. Among the many proposed solution, few representative configurations with different degrees of complexity are presented in the following.

Bending actuators can be obtained by applying DEAs on a flexible but stiff substrate [90], forming the so-called uni- or bimorph structures. The application of an high electric field across the dielectric, elongates the elastomer membrane, which bends similarly as bimetallic strips upon heating. Unimorph structures, as the one shown in Figure 2.17(a), can bend in one direction only. A bi-directional bending is achieved by sandwiching a stiff substrate between two DEAs.

The two-phase planar configuration, also known as agonist-antagonist actuator, is a dielectric elastomer membrane actuator capable of linear displacement parallel to the elastomer surface, i.e. perpendicular to the mean direction of the electric field (Figure 2.17(b)). It has been first proposed by Pelrine *et al.* [119]. It is made up of a relatively large, pre-stretched dielectric membrane with at least two pairs of independent electrode sets. The

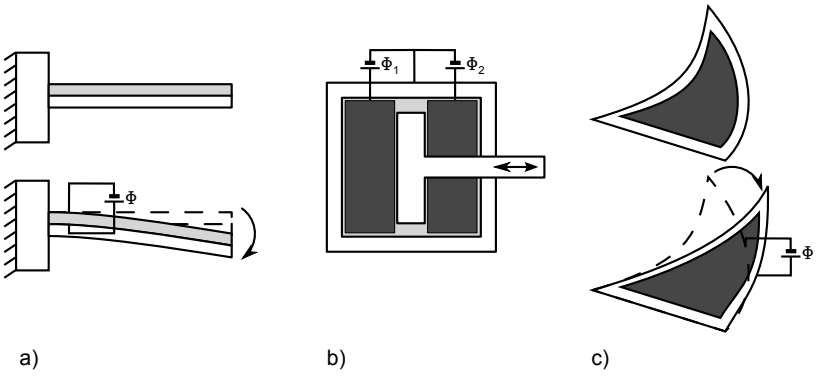

Figure 2.17: Three elemental actuator configurations. (a) bending actuator [115]; (b) two-phase agonist-antagonist planar actuator [119]; (c) dielectric elastomer minimum energy structures (DEMES) [86]

actuation of the agonist electrode set causes the displacement of a central shaft towards the opposite antagonist, and vice versa.

First proposed by Kofod *et al.* [86], Dielectric elastomer minimum energy structures (DEMES) are actuators that usually produce a bending movement or a more complex unfolding of a complex structure. A pre-stretched elastomer is bonded on a stiff but thin and flexible frame with one or more open sections. As the elastomer releases its pre-stretch, the supporting structure folds due to its low bending stiffness. The actuation of the electrode region, usually suspended throughout the open sections, causes a relief of the pre-stress and unfolding of the DEMES structure (Figure 2.17(c)).

Cone actuators (2.18(a)) are capable of linear actuation, normal to the substrate on which the DEA is located [17]. A pre-stretched dielectric elastomer membrane is glued between two concentric rigid circular frames. One frame is fixed and the other connected to a load. Actuator activation causes the membrane to widen and the load to move normally to the surface.

The spider configuration by Poole & Booker [123] achieves linear actuation by coupling a circular membrane with few legs that act as a kinematic amplifier (2.18(b)). On actuation, the electrode area becomes larger, opening the legs and causing a downward motion of the central hinge.

Dielectric elastomer zipping actuators [103] are pre-stretched membranes,

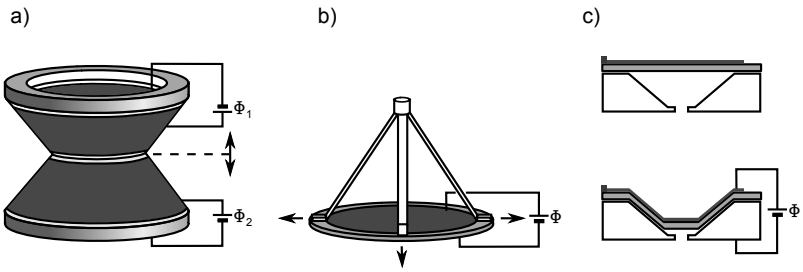

Figure 2.18: Simple configurations capable of moving normally to the surface on which they lie. (a) Cone actuator [17]; spider actuator [123]; (c) zipping actuators [103].

flush-mounted over a metal surface where cavities are located. A compliant electrode is brought on the top surface of the elastomer only. The imposition of an electric field between the top electrode and the metal plate results in a downward movement of the elastomer membrane. An orifice ensures air outflow to improve the displacement (Figure 2.18(c)).

Actuators based on a single elastomer membrane normally produce useful work by converting area strain rather than thickness strain, due to the low thickness of elastomer membranes required to keep the driving voltage to an acceptable level. However, multi-layer actuators, produced by stacking tenths or hundreds of dielectric and electrode layers, can produce significant displacement in the mean direction of the applied electric field, without requiring any kinematic amplifier or pre-stretch.

While the concept of multi-layer actuator had been already introduced by Pelrine *et al.* [115], the first fully-automatic production process for dielectric elastomer stack actuators has been conceived and put into practice by Jungmann [73]. It consists of three main steps, schematically shown in Figure 2.19. A two-component liquid silicone is deposited onto a rotating plate, where it is thinned down to a small dielectric layer by spin-coating. After thermal curing, electrodes are automatically air-brushed onto the dielectric and patterned with by means of a shadow mask. Figure 2.20 schematically shows the final stack actuator, consisting of a monolithic stack of about 100 dielectric layers, from 20 to 50 μm thick, capable of an active thickness strain of 10%.

Kovacs & Düring [92] implemented another production process for ac-

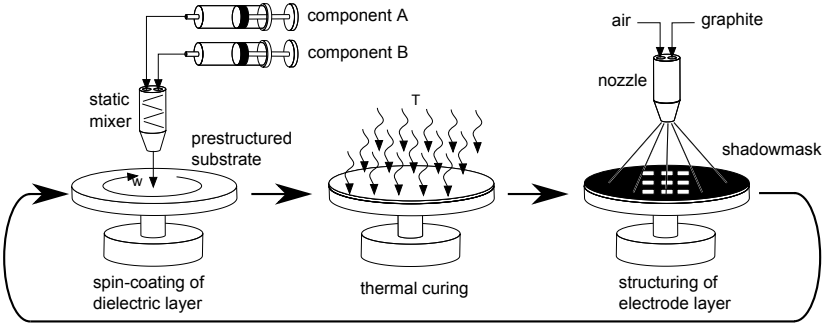

Figure 2.19: Schematic of the fully-automatic dielectric elastomer stack actuator (DESA) fabrication process by Lotz *et al.* [99].

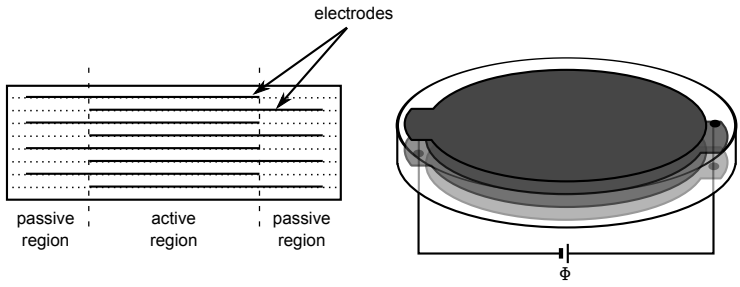

Figure 2.20: Sketch of a dielectric elastomer stack actuator (DESA).

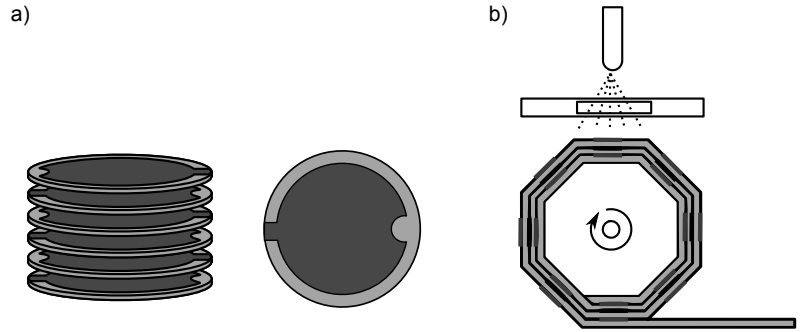

Figure 2.21: Fabrication of dielectric elastomer stack actuators. (a) the concept of Kovacs & Düring [92]; (b) the idea of Randazzo *et al.* [134]

tuators in multi-layer configuration, where single dielectric layers are cut out of larger films and provided with electrodes (Figure 2.21(a)). A semi-automatic roll-to-roll process has been suggested by Randazzo *et al.* [134], which is schematically shown in Figure 2.21(b). While a dielectric acrylic film is rolled on a substrate, electrodes are air-brushed with the aid of a mask.

2.2.4 Aeronautical applications

Actuators based on dielectric elastomers found a broad spectrum of different applications, as haptic feedback devices [107], peristaltic pumps [99], vibration attenuation [74], tunable lenses 35 and muscle-like actuators for soft robotics 36, 121. However, only few noteworthy examples of actuator solutions for aeronautical application can be found in the literature.

Particularly relevant is the research conducted by the flow control research group of Prof. Morrison at the Imperial College. Dearing *et al.* [40] developed the so-called active dimples, scalable actuators aimed at near-wall turbulent flow manipulation and separation control. They consist of a silicone membrane suspended over a circular cavity (Figure 2.22(a)) that can buckle inwards and outwards at frequencies of hundreds of Hz. Large active, asymmetric deflections could be achieved when the actuation is driven at one of its eigenfrequencies. However, this concept suffers from

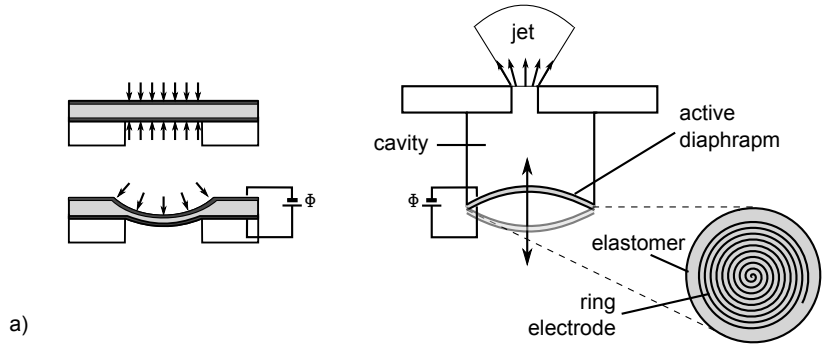

Figure 2.22: DEAs in aeronautic applications: (a) dimple actuator by Dearing *et al.* [40] and (b) micro-fabricated zero-net-mass-flux (ZNMF) actuator of Pimpin *et al.* [120].

complex fluid-structure interactions, which make it difficult to predict the actuator behavior in complex experimental scenarios.

Zaremski & Amitay [171] developed dielectric elastomer actuators similar to the active dimples of Dearing *et al.* [40]. The flow about an active dimple located in a separation bubble was investigated with stereo Particle Image Velocimetry (PIV). A beneficial effect of actuation on the reduction of the separation bubble size was shown.

The micro-fabricated zero-net-mass-flux (ZNMF) actuator of Pimpin *et al.* [120] consists of a dielectric elastomer actuator with metallic spiral electrode, installed in a cavity with an orifice. The dielectric elastomer acts as an active diaphragm capable of producing periodic blowing and suction, with peak jet velocity of 50 mm/s at 1.6 kHz. The actuator configuration is sketched in Figure2.22(b).

Synthetic jet ZNMF actuators similar to, but indeed larger than, those by Pimpin *et al.* [120] have been developed also by Slipher & Hubbard [151], which achieved jet velocity of 25 m/s close to the exit nozzle of a 13 mm cavity at 250 Hz. The actuator is sketched in Figure 2.23

The only implementation with dielectric elastomers of spanwise wall oscillations for turbulent flow-control aimed at skin-friction drag reduction has been attempted by Gouder *et al.* [57, 58]. They adapted the two-phase, agonist-antagonist actuator of Pelrine *et al.* [119] to produce in-plane oscillations of a 30×30 cm^2 soft surface. When the actuator was driven at its

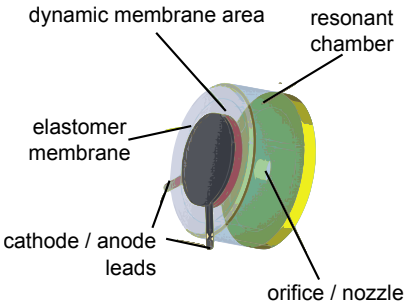

Figure 2.23: Synthetic jet ZNMF by Slipher & Hubbard [151].

mechanical resonance frequency it achieved a peak-to-peak displacement of about 5 mm at a frequency of 40 Hz. However, they found this technology to be unattractive due to the fragility of the actuators, having a lifetime of only a few minutes [57], and electromagnetic linear motors have been preferred instead. The actuator configurations of Pelrine *et al.* [119] and Gouder *et al.* [58] are the starting point of the investigation carried out in Chapter 3, where they are first thoroughly characterized and improved.

3 Development of dielectric elastomer actuators

The simplicity of DEA actuators allows a large number of design choices that can significantly influence their final performance. As a rule of thumb, preserving low mechanical complexity and fabrication processes in a DEA-based device is recommended, as proven in several commercial success stories.

Dielectric elastomers are chosen as building blocks to design active surfaces that are capable of exerting in-plane, unidirectional oscillations. Their dynamic performance, measured using amplitude and frequency of oscillation, must comply with the requirements for flow control applications aimed at turbulent drag reduction via in-plane wall oscillations. Section 3.1 and 3.2 describe the choice of the two main constitutive components of a DEA: the dielectric material and the compliant electrodes. A thorough investigation or development of the best dielectric and electrode material are out of the scope of this work, therefore the available information in the literature, aided by selected investigations, is reviewed to methodically assess promising choices for the present application. In Section 3.3, the controversial effects of pre-stretching the dielectric membrane are studied, with a focus on changes in the dielectric properties (Section 3.3.1), on static (Section 3.3.2) and on dynamic (Section 3.3.3) actuation performance. The mechanisms of dynamic actuation is investigated in Section (Section 3.4), where the active displacement of a membrane actuator is observed in time and space, focusing on its propagation throughout the membrane. Finally, the fabrication process of the DEA active surfaces is described in detail in Section 3.5, followed by an assessment of its mechanical and electrical response. Phenomenological models are found that describe the actuator characteristics and provide insights into the underlying physics. The power required to run the actuator in a typical flow-control scenario is experimentally measured. This parameter is of great importance for flow control applications, as it allows measurement of the net power saving, i.e. the net efficiency of utilizing an active flow-control device.

3.1 Dielectric material

The dielectric, together with the compliant electrodes, is one of the two main components that forms a dielectric elastomer actuator. Its mechanical and electrical properties largely influence the final characteristics and performance of an actuator. In the following, the main available dielectric elastomers are briefly evaluated according to the present requirements for successful turbulent skin-friction drag reduction in low-speed wind tunnel: about 5 mm peak-to-peak maximum planar displacement at a frequency of about 100Hz.

Since the seminal work of Pelrine *et al.* [115], the challenge of finding the most suitable material for DEAs has remained. Ideally, the perfect dielectric has a low linear elastic modulus Y and high relative permittivity ϵ_r and dielectric breakdown field strength E_B [119]. Particular shapes of the hyperelastic stress/stretch characteristics are also desirable for DEA applications [117, 157, 173]. Obviously, the ideal elastomer does not exist and compromises between various mechanical and electrical properties are made, usually tailoring the elastomer to a certain application. From the most common and less exotic choices, three main polymer groups are identified [16]:

- polyacrilates
- polyurethanes (PU)
- silicones (polydimethylsiloxane, PDMS)

The commercial adhesive elastomer VHB© 4910/4905 by 3M™ is the most widespread elastomer in laboratory implementations of DEAs and also unique in the category of polyacrilates. Pelrine, Kornbluh & Heydt [91, 117, 117] discovered its particular capability of reaching high active strains of more than 100%. Sine then, several world records of active deformation with VHB-based DEAs have been documented [56, 77]. Commercially available as a high-performance, double-sided tape, the features of VHB reflect its intended use. For instance, its thickness ranges between 0.5 mm (VHB 4905) and 1 mm (VHB 4910), requiring the imposition of high planar pre-stretches in order to reduce the operating voltage [36, 168]. Simultaneously, the practice of pre-stretching improves the dielectric breakdown field strength [64, 162], which increases from 20 V/μm in the unstretched state up to about 400 V/μm at very high stretches. The relative permittivity of about $\epsilon_r \approx 5$ varied significantly in time, as

the producer 3M, changed the formulation of the VHB tapes [84]. In spite of the attractive achievable active stretches, its very high viscoelastic behavior makes the VHB acrylic unsuited for dynamic applications; typical frequencies of VHB-based actuators being $\mathcal{O}(1)$ Hz.

Polyurethanes (PU) exhibit excellent dielectric properties, such as a high dielectric constant $\epsilon_r > 5$ and very high dielectric breakdown field strength. However, only few examples of PU-based dielectric elastomer actuators can be found in the literature, the attempt by Cameron *et al.* [23] being the most notable one to date. Recently, consortia of industrial and academic partners have attempted to harness the potential of ad-hoc PU formulations and raise the production quality of PU-based DEAs to commercial grade products [125, 166]. At the present stage, however, its favorable dielectric properties are not coupled with same advantageous elastic properties, typical values of the elastic modulus being about 10 MPa, with associated lower maximum stretches at break. The high stiffness enables fast actuation up to the kHz range, although achieving large deformations may be more challenging. Furthermore, the flammability of most PUs, which is a risk factor during operation in the wind tunnel, together with the scarce experience and literature about PU-based DEAs, resulted in the decision to reject them as possible candidates for the present application.

Polydimethylsiloxanes (PDMS), known as silicones, have been widely investigated for application in dielectric elastomer actuators [119] and several applications in commercial products featuring DEAs can be found, such as the haptic ViviTouch technology of Artificial Muscle Inc. and the actuators developed by the companies Danfoss, CTS and Optotune. There is an incredibly large selection of silicones commercially available, and researchers have tested only few of them as dielectric membranes for DEAs, such as Nusil CF19-2186© [116, 143], Dow Corning Sylgard 186© [3, 116, 119, 144], Dow Corning HS2, HS3 and DC3481© [116, 117, 119, 172], Elastosil© P7670 [60, 99], Elastosil© RT625 [71]. Particularly interesting for the present study is also NuSil MED-4905©, used by the Flow Control Group of the Imperial College for turbulent flow control applications [40, 58]. The main elastic and dielectric features may vary between different silicones. However, a somewhat lower dielectric constant of $\epsilon_r \approx 3$ is usually exhibited, while the elastic modulus may vary from 0.1 to more than 1 MPa. The dielectric breakdown field strength correlates well with the elastic modulus [88, 89], being higher for stiffer silicones, and thus ranges from 20 V/μm for the softest to more than 100 V/μm for the stiffer silicones.

Among this vast choice, the focus is now placed on a small selection

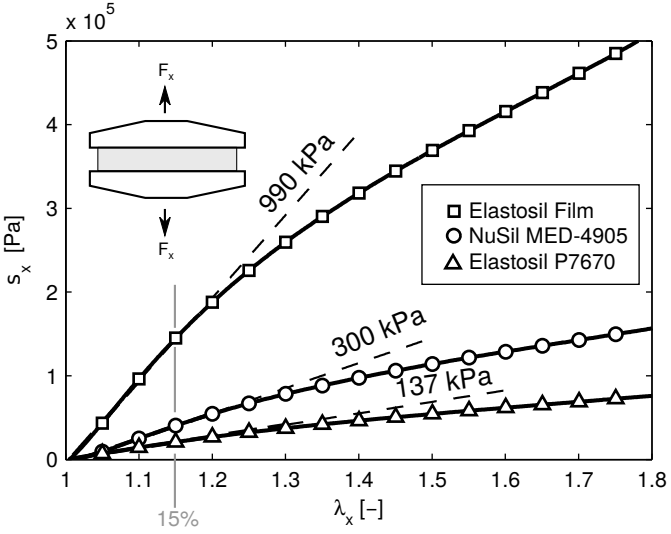

Figure 3.1: Pure-shear tensile tests for three different elastomers up to 80% elongation. Squares: Elastosil Film; Circles: NuSil MED-4905; Triangles: Elastosil P7670. Dashed lines represent the linear least-square fit of the experimental data for elongation up to 15%. Numbers: linear elastic modulus.

of three different elastomers: Elastosil P7670, NuSil MED-4905 and Elastosil Film. The Elastosil P7670 has become the standard material in the fully-automatic fabrication process of dielectric elastomer stack actuators (DESA) at the institute of the electromechanical design (EMK) of the Technische Universität Darmstadt, where the present investigation is conducted. This two-component, addition-curing silicone features a low viscosity in the uncured state (1800 mPa s from data sheet), a short pot life and short curing time within a wide range of temperatures. A large database of its mechanical and dielectric properties has been collected in the past years [60, 99], comprising its dielectric properties as a function of curing parameters.

On the other hand, NuSil MED-4905 is interesting since it has already been employed by Gouder *et al.* [58] for the realization of spanwise oscillating surfaces with DEAs. Both Elastosil P7670 and NuSil MED-4905

are originally developed for prosthetic applications and exhibit mechanical properties close to that of human tissue. However, NuSil MED-4950 is developed for use in injection molding production process and therefore exhibits a 100-fold higher viscosity compared to Elastosil P7670. Standard processing techniques for production of elastomer thin films, such as spin-coating and tape casting, become impractical with highly viscous fluids. Moreover, the problem of air trapping becomes particularly severe, which requires mixing and curing process to be carried out in a vacuum. Finally, Gouder *et al.* [57, 58] reported frequent failures of the dielectric elastomer actuators, which, though not directly ascribable to the particular dielectric material, do not support its choice either.

As of middle 2013, Wacker Chemie started the production of a high-quality, high-precision, already cured silicone film with a specific formulation optimized for DEA applications, commercially named Elastosil Film. In the framework of the project EPoSil (Elektroaktive Polymere auf Silikonbasis zur Energiegewinnung), in which Wacker Chemie is a partner, few samples of a provisional version of Elastosil Film were delivered for testing and characterization.

Figure 3.1 shows the engineering stretch/stress characteristics for all three elastomers in the pure-shear configuration up to 80% elongation. Two aluminium clamps grip a rectangular specimen of 110 mm in width and 10:1 aspect ratio. The slender aspect ratio ensures the pure shear state of strain. The uppermost clamp is connected to a load cell (Hoettinger Baldwin U1A) which can be displaced vertically by a linear motor (Newport MFA-PP) with a prescribed velocity of 0.1 mm/s. The position is computed by counting the number of motor turns with the internal motor encoder. All signals are acquired and generated through a National Instruments 7852R FPGA board that is programmed from a windows desktop computer running LabView 2013. The Mullins effect has been taken into account by repeatedly stretching the elastomer to twice its initial length before conducing measurements. A linear least-square fit of the stress/stretch characteristic up to 15% elongation is used to compute the linear elastic modulus Y for small deformations. Elastosil P7670 and NuSil MED-4950 show comparable values of Y, being for NuSil MED-4905 approximately twice as large. Elastosil Film, on the other hand, is much stiffer and exhibits an elastic modulus in pure-shear mode of $Y = 990$ kPa. As mentioned in Chapter 2.2.1, a first figure of merit (FOM) to evaluate the capability

of an elastomer to actively deform is:

$$FOM = \epsilon_0 \epsilon_r \frac{E_B^2}{Y} \tag{3.1}$$

where E_B is the dielectric breakdown field strength and ϵ_0 and ϵ_r the vacuum and relative permittivity.

The dielectric breakdown field strength in the undeformed state is 30 V/μm for Elastosil P7670 and NuSil MED-4905 [98], while it is larger than 100 V/μm for Elastosil Film. Assuming that the dielectric constant ϵ_r does not change significantly among silicones, Elastosil Film shows the best figure of merit and NuSil MED-4905 the worst. Therefore, Elastosil P7670 is preferred to NuSil MED-4905 and the promising Elastosil Film has been investigated and adopted according to with its availability.

3.2 Compliant electrodes

Compliant electrodes are the second constitutive part of dielectric elastomer actuators, which allow the deposition of electric charges on the elastomer surface and consequently active deformation. In a seminal paper, Pelrine *et al.* state that "the ideal electrode is highly conductive, perfectly compliant and patternable, and should be made thin relative to the polymer thickness" [119]. In fact, the electrode must sustain the large deformation of the polymer to which it is bonded while remaining conductive and without significantly influencing the stiffness of the system. While considerable research efforts have been spent in the search of an electrode formulation that fulfills the stringent requirements for DEA applications, several techniques of fabricating compliant electrodes have been established in laboratory implementations of DEAs, where compromises between ease of fabrication, compliance and conductivity are made.

A comprehensive review of the abundant number of available solutions can be found in Rosset & Shea [145]. The present work is not focused on researching new electrode formulations and the most common choice in laboratory implementations of DEAs, the carbon-based electrodes, has been adopted.

Graphite flakes (MF2, NGS Naturgraphit GmbH) with a typical size of 2 μm are deposited as loose particles onto the surface of the elastomer, to which they spontaneously stick, or sprayed in a 20:1 mixture with isopropyl alcohol, aided by a shadow mask. The electrodes exhibit a fairly high sheet resistivity of 10 k$\Omega_\square$ [98] with a thickness in the order of the particle size.

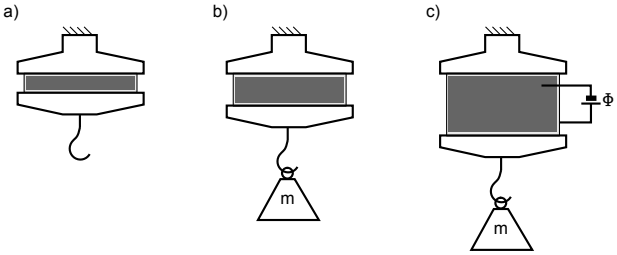

Figure 3.2: Typical actuation scenario of a dielectric elastomer membrane. A membrane without a pre-stretch cannot exert compressive forces (a). The imposition of pre-stretch at constant force (b) results in an elonation of the membrane upon actuation (c).

We recall that the bulk resistivity ρ_s is related to the sheet resistivity R_s as follows:

$$\rho_s = R_s \, t_e \tag{3.2}$$

where t_e is the electrode thickness. The electrode resistivity is known to increase upon deformation, showing a two-fold increase for an area stretch of 1.25 [98]. The electrode fabrication and deposition processes, which have been last optimized by Matysek [106], prove to be suitable, though not optimal, for the present application, for which actuation frequencies of about 100Hz and active strains of about 20-30% are required. Moreover, thanks to their simplicity, graphite electrodes allowed a rapid production of various prototypes of DEAs at a relatively low cost.

3.3 Effect of the pre-stretch

Most dielectric elastomer membranes capable of planar linear actuation need to be given a certain amount of pre-stretch in the two planar directions, which is usually maintained either by a supporting frame on which the elastomer is bonded (see for instance [4, 5, 119]) or by a constant force ([15]). In both cases, actuation can be interpreted as a decrease in stiffness of the electrode area of the dielectric elastomer [114], as sketched in Figure 3.2. The need for pre-stretching is evident, as the membrane cannot overcome compressive stresses at its ends without buckling, resulting in an

out-of-plane movement.

The practice of pre-stretching also affects the geometric [85], mechanical [85, 97, 121] and eventually dielectric [64, 98, 121, 162] properties of the elastomer and can significantly influence the final performance of a DEA. The pre-stretch influence on actuation has been tested primarily on the 3M VHB 4910 acrylic elastomer, for which pre-stretching is indispensable to reduce its large initial thickness, and is very material dependent. Therefore, in order to find the combination of this important parameter that maximize static and dynamic actuation, the rest of this section is devoted to investigating its effect on actuators based on the Elastosil P7670 silicone elastomer.

3.3.1 Dielectric breakdown field strength

As anticipated by the small strain approach in Section 2.2.1, the dielectric breakdown strength is the ultimate physical limit that hinders the possibility of actively stretching a dielectric elastomer up to its mechanical failure and, therefore, is of paramount importance in defining the actuator performance bounds [3, 157]. It does not depend solely on the chemical properties of the material, but also on its physical properties, such as mechanical stiffness [88, 89], thickness [2, 38, 45, 55, 61, 78] and stretch state [64, 87, 122], the latter of great interest for dielectric elastomer actuators (DEAs) due to its beneficial effects on actuation [3, 85, 122, 157]. In literature, the

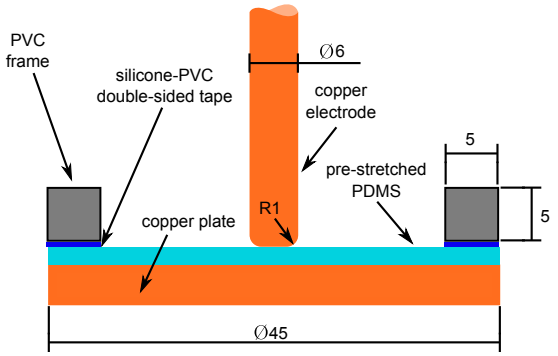

Figure 3.3: Schematic of the test stand used for dielectric breakdown field strength. Dimensions in mm.

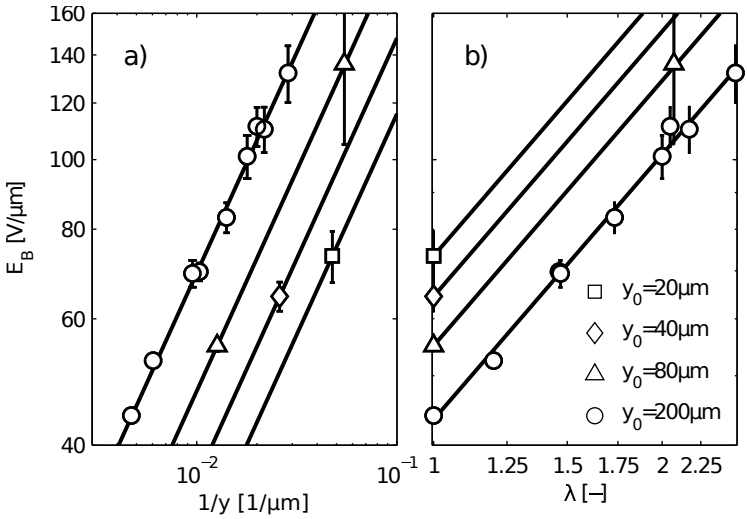

Figure 3.4: (a) Dielectric breakdown field strength E_B of the silicone elastomer Elastosil P7670 as a function of the (reciprocal of the) thickness $1/y$ after pre-stretch. (b) Dielectric breakdown field strength E_B of the silicone elastomer Elastosil P7670 against the equivalent stretch λ.

combined effect of dielectric thickness and pre-stretch on the breakdown strength has been studied mostly for the acrylic elastomer VHB 4910, for which it greatly improved at high pre-stretches and thinner membranes. However, data on more reliable silicones eligible to be used as actuators are missing.

Therefore, the dielectric breakdown field strength of Elastosil© PDMS sheets with 4 different initial thicknesses of 20 μm, 40 μm, 80 μm and 200 μm is investigated. The thicker foils are doctor-bladed onto a 90 mm×1000 mm glass substrate while the thinner foils are directly spin-coated onto Ø45 mm circular copper substrates, according to the process described by Lotz *et al.* [99]. The 80 μm specimens are fabricated as a single-layer film and as two-layer 40 μm films, directly superimposed during spin-coating. The thickness of the unstretched samples is precisely measured with a Veeco Dektak 150+ surface profilometer, using a stylus force of 1 mg, while for the stretched samples a thickness gauge is used. The applied pre-stretches are mostly biaxial, with some additional uniaxial and anisotropic

cases, to verify the effect of an eventual anisotropy. The equi-biaxial pre-stretches are imposed with a multi-clamp, circular pre-stretch jig. A circle of 30 mm initial diameter d_0 is drawn on the unstretched specimen and its deformation is used to measure the pre-stretch ratio, defined as $\lambda_{bi} = d_1/d_0$, where d_1 is the diameter of the circle after pre-stretch. A four-clamp rectangular pre-stretch jig is used to uniaxially and anisotropically stretch rectangular samples of 90 mm× 80 mm. A 50 mm×50 mm square is painted onto the PDMS unstretched film to verify homogeneity and amount of pre-stretch. In this case $\lambda_x = x_1/x_0$ and $\lambda_z = z_1/z_0$ are the pre-stretches in x- (width) and z- (length) planar direction respectively. In order to compare the amount of pre-stretch of specimens stretched with different stretching techniques, an equivalent stretch ratio λ is introduced, defined as the square root of the area stretch. If we assume the material to be incompressible, the equivalent stretch for equi-biaxial state is simply $\lambda = \lambda_{bi}$ while for the anisotropic case $\lambda = \sqrt{\lambda_x \lambda_z}$. Once stretched, the PDMS films are placed on copper plates, cleaned with isopropyl alcohol, to which they firmly stick. The plate constrains active displacement during the measurements and avoids crack propagation after breakdown.

The experiment is aimed at measuring the breakdown voltage strength by limiting the active thinning of the dielectric, which can become extreme after electromechanical instabilities occur, documented by Stark & Garton [155], and can lead to premature failure [20]. The dielectric-breakdown test stand is sketched in Figure 3.3. The copper plate acts as a bottom electrode, while the top electrode consists of a copper cylinder of 6 mm diameter, lowered onto the specimen from the top. The cylinder is polished and has rounded edges in order to reduce field inhomogeneities due to the presences of tips that cause charge accumulation and local deformation. The experiment consists of increasing the voltage (in-house 0-15 kV DC voltage amplifier) stepwise from a safe low limit until the breakdown voltage is reached. The voltage is held constant for 20 s before increasing in steps of 100 V. We define the breakdown as the moment when a sudden and steep increase in leakage current occurs and set the breakdown voltage to the previous voltage level. The nominal dielectric breakdown field strength is then defined as the breakdown voltage Φ_B divided by the measured height y after pre-stretch:

$$E_B = \Phi_B/y \tag{3.3}$$

The results (Figure 3.4(a-b)) show that the breakdown field strength of the Elastosil P7670 PDMS elastomer can be significantly enhanced either by decreasing its thickness (Figure 3.4(a)) or by increasing the pre-stretch

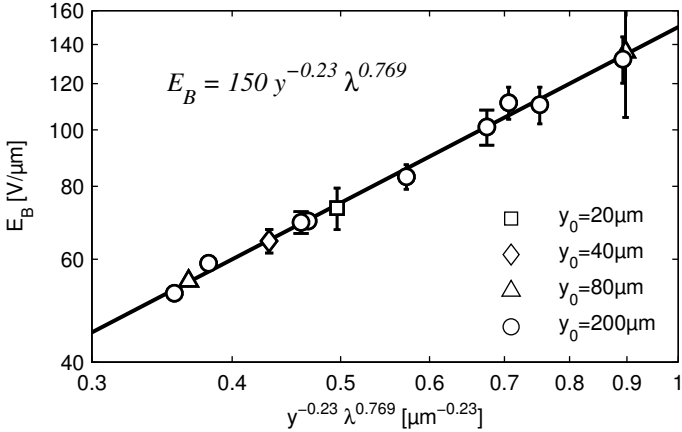

Figure 3.5: Dielectric breakdown field strength E_B of the silicone elastomer Elastosil P7670 against the empirically found scaling parameter $y^{-0.23}\lambda^{0.77}$. When multiple lines are present, their slope is obtained from a linear least squares fit to the data for thickness $H = 200\mu m$. Each line is offset vertically to pass through the data point corresponding to the respective thickness.

ratio (Figure 3.4(b)). A three-fold change in E_B has been observed over the investigated parameter range of y and λ. The breakdown field strength exhibits a clear trend for samples with the same initial thickness y_0, which implies that the dielectric breakdown field strength depends on both thickness and stretch simultaneously, as found by Huang *et al.* [64] for the VHB 4910 polyacrylate elastomer. All the data at different thicknesses y and stretch ratios λ collapse onto a single line (Figure 3.5) if the empirical relation $E_B = Cy^{\alpha}\lambda^{\beta}$, proposed by Huang *et al.* [64], is adopted. The empirical coefficients α and β are found by a least-square fit of the entire experimental dataset and lead to the following relation for the dielectric breakdown strength of the Elastosil P7670 silicone elastomer:

$$E_B = 147\, y^{-0.23\pm0.02}\, \lambda^{0.77\pm0.03} \tag{3.4}$$

where y is expressed in μm and E_B in V/μm, and the confidence level is 95%. This empirical fit is shown in Figure 3.5 as a straight line.

The initial thickness $y_0 = \lambda^2\, y$ can be used instead of the thickness after

pre-stretch h in Equation 3.4, leading to the correlation:

$$E_B = 147\, y_0^{-0.23\pm0.02}\, \lambda^{1.23\pm0.03} \tag{3.5}$$

This relation indicates that, as far as an increase in dielectric breakdown field strength is concerned, a higher stretch ratio is more effective than the use of an initially thinner elastomer film.

Electric field inhomogeneities are investigated as a possible factor that may bias the present measurement of the dielectric field strength, using finite element modeling of the experimental setup with the software CST Studio Suite. The PDMS layer is modeled as a dielectric with constant relative permittivity $\epsilon_r = 3$ and the electrodes are modeled as ideal conductors, while all dimensions are equal to the physical setup (Figure 3.3).

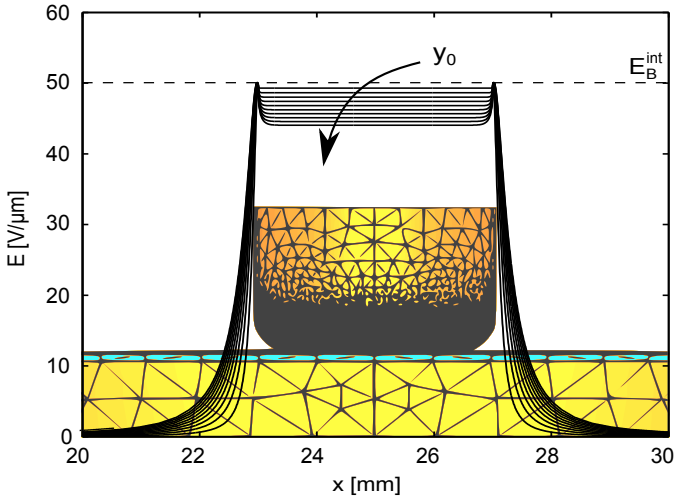

Figure 3.6: Magnitude of the electric field E in $V/\mu m$ along a diameter on the top face of the silicone membrane for various thicknesses y_0 of the dielectric; a section of the simulated setup and its numerical discretization is also shown in the background. Two spikes in the electric field strength are present in the vicinity of the top electrode edge, and their amplitude increases with the thickness of the elastomer if the maximum E is kept constant for all simulations.

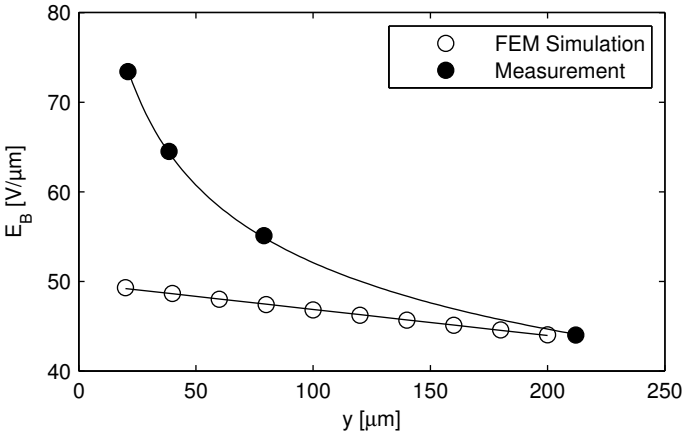

Figure 3.7: Trends of the apparent dielectric breakdown field strength against the dielectric thickness. Empty circles: data from a finite element simulation where a real breakdown strength E_B^{int} = 50 is assumed; filled circles: experimental data for unstretched (λ = 1) Elastosil P7670 silicone membranes.

Figure 3.6 shows the magnitude of the electric field E along a diameter on the top surface of the dielectric for silicone layers of thickness ranging from 20 to 200 μm. In the vicinity of the top electrode edge E presents two local spikes. Here the real dielectric breakdown limit E_B^{int} (assumed to be 50 V/μm in Figure 3.6) is reached first and is higher than the nominal dielectric breakdown field E_B estimated with Equation 3.3 at the center of the membrane. The relative difference between E_B^{int} and E_B increases with the dielectric thickness, possibly leading to an apparent thickness-dependent dielectric field strength.

Figure 3.7 shows the trends of the nominal dielectric breakdown field strength against the thickness for unstretched silicone membranes; both experimental and numerical datapoints are plotted. In simulations, the nominal dielectric field strength is defined as the magnitude of the electric field in the central part of the membrane when the constant intrinsic breakdown field of E_B^{int} = 50 V/μm is reached in proximity to the electrode edge. We observe that the boundary effects cause a mild thickness-dependence of the dielectric field strength, which is much steeper for experimental data.

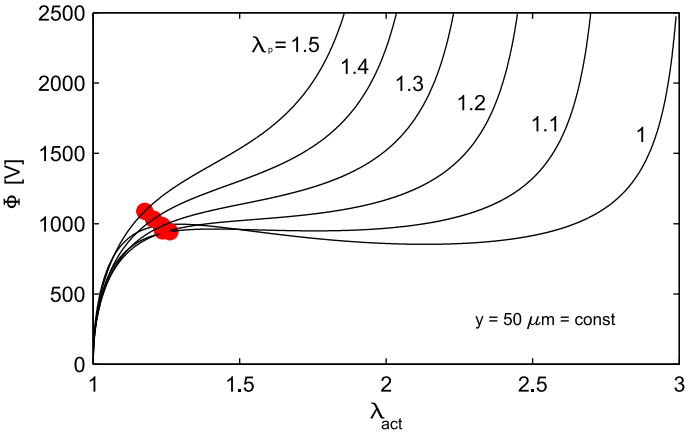

Figure 3.8: Predicted voltage Φ against actuation stretch λ_{act} assuming a constant dielectric breakdown field strength of 70 V/μm. Red circles: failure due to dielectric breakdown; Red cross: failure due to dielectric breakdown during a pull-in instability.

This means that the particular choice of electrode shape only marginally affects the measured breakdown strength or the estimated dependence on the thickness.

The importance of considering and measuring the pre-stretch and thickness dependency of the dielectric breakdown field strength can be highlighted by a simple idealized actuation scenario that can be analytically treated. A circular membrane of initial diameter d_0 is pre-stretched untill a diameter d_1 under a constant force F is reached. After imposition of an electric field, its diameter will further increase to d_{act}. Equation 2.61, which describes the active hyperelastic deformation of a dielectric elastomer actuator under constant pre-load condition, can be rewritten for equi-biaxial conditions ($\lambda_x = \lambda_z = \lambda$) as follows:

$$\epsilon_0 \epsilon_r \lambda_{act}^4 \frac{\Phi^2}{y_0^2} = f(\lambda_p \lambda_{act}) - f(\lambda_p)\lambda_{act} \tag{3.6}$$

where $\lambda_{act} = d_{act}/d_1$ is the equi-biaxial active stretch, $\lambda_p = d_1/d_0$ is the equi-biaxial pre-stretch and $f = \mathrm{d}W/\mathrm{d}\lambda$ is the derivative of the Gent strain energy density function W, whose empirical coefficients are found by fitting

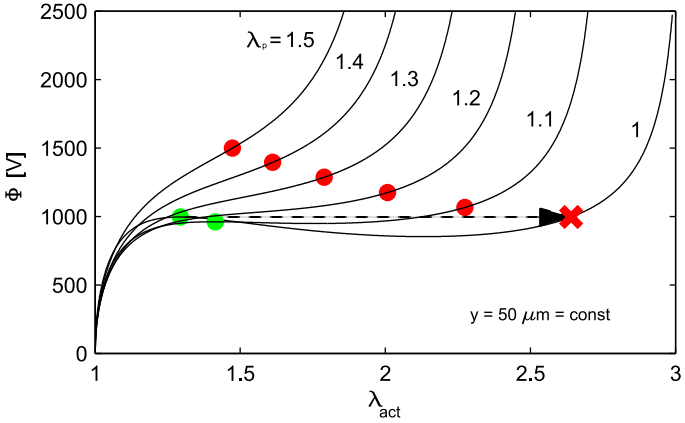

Figure 3.9: Voltage Φ against actuation stretch λ_{act}, assuming a variable dielectric breakdown field strength according to Equation 3.4. Symbols as in Figure 3.8.

high-precision uni-, bi-axial and pure-shear tensile tests.

The voltage - active stretch curve for an Elastosil P7670 dielectric elastomer actuator under the aforementioned actuation condition is shown in Figure 3.8, assuming a constant dielectric field strength of $E_B = 70V/\mu$m, and in Figure 3.9, allowing a variable dielectric field strength according to the proposed empirical law. The failure mode of the dielectric elastomer actuator is represented with symbols. Green triangles mark the onset of a pull-in instability, whose consequent large deformation at constant voltage might thin the dielectric beyond its dielectric breakdown strength. Red dots mark the failure due to dielectric breakdown during a stable condition, i.e. when $\mathrm{d}V/\mathrm{d}\lambda_{act} > 0$. We again emphasize the fact that in this framework the only failure mode is dielectric breakdown failure. The electromechanical pull-in instabilities do not directly imply actuator failure, which actually only occurs if the thinning due to the active stretch is so extreme that the breakdown field strength limit is then reached (red crosses).

When a constant dielectric breakdown field strength is assumed (Figure 3.8), maximum active stretches of only 1.3 are reached, the only failure mechanism is the dielectric breakdown and the actuator never survives pull-in instabilities. If we account for a variable electric dielectric breakdown field (Figure 3.9) the scenario is completely different. The stretch

state of the elastomer, i.e. product of its pre-stretch λ_p and active stretch λ_{act}, might increase the dielectric breakdown field strength and allow the actuator to survive a pull-in instability and reach very large field-induced deformations.

3.3.2 Static actuation

The improvement of the dielectric breakdown field strength partially explains the increase in actuation performance of the elastomer with incorporated pre-stretch, thanks to the higher applicable electric field and resultant Maxwell pressure. However, pre-stretching also directly affects the electromechanical coupling of a DEA, due to its nonlinear hyperelastic and electrostatic properties.

Consider again the actuation scenario treated in the previous section and introduced in Section 2.2.2, in which a circular membrane of initial diameter d_0 and thickness y_0 is imposed an equi-biaxial pre-load ($F_x = F_z = F$) that stretches it up to a diameter d_1, resulting in a pre-stretch $\lambda_p = d_1/d_0$. The imposition of a voltage difference Φ between the electrodes results in an active stretch $\lambda_{\text{act}} = d_{\text{act}}/d_1$, where d_{act} is the diameter upon actuation. In this condition, equation 2.61 reads

$$\epsilon_0 \epsilon_r \lambda^4 \frac{\Phi^2}{y_0^2} = \frac{2\mu_e J_m \left(\lambda^2 - \lambda^{-4}\right)}{J_m - 2\lambda^2 - \lambda^{-4} + 3} - \sigma_p \lambda \lambda_p^{-1} \tag{3.7}$$

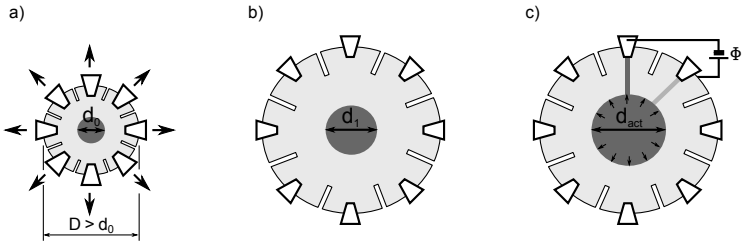

Figure 3.10: Sketch of equi-biaxial pre-load and actuation of a dielectric elastomer membrane. (a) A circular membrane is equi-biaxially pre-stretched to a diameter $d_1 > d_0$ (b). Upon actuation, the electrode area enlarges while the inactive part of the membrane shrinks (c).

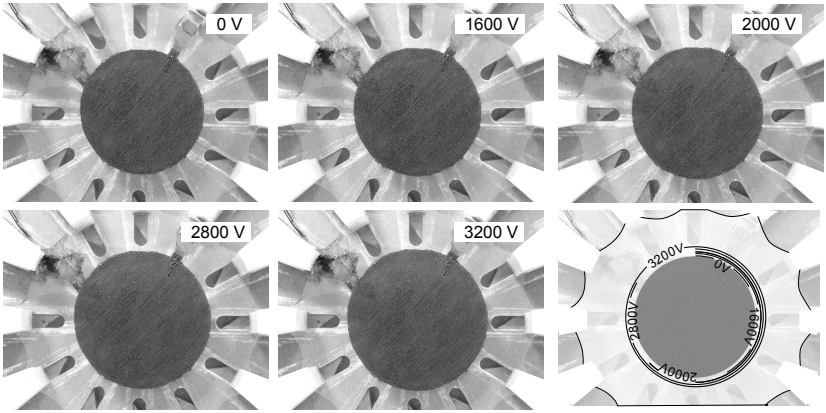

Figure 3.11: Picture of an equi-biaxially pre-stretched membrane actuator. The potential difference between the electrode is increased from top-left to bottom-right. As a consequence, the electrode area increases.

where $\lambda = \lambda_p \lambda_{\text{act}}$ is the total stretch and σ_p the imposed equi-biaxial pre-stress, solution of the Equation 3.7 for $\Phi = 0$ and $\lambda = \lambda_p$.

In the governing Equation 3.7 the pre-stretch λ_p, also included in the total stretch λ, plays a very important role in determining the active stretch; hence, the total deformation of the actuator. In fact, an optimum pre-stretch might exist for a certain actuation condition that results in a higher active deformation of the elastomer.

The existence of an optimal pre-stretch in the actuation direction is investigated by experimentally reproducing an actuation scenario similar, yet not identical, to that of Equation 3.7 and shown in Figure 3.10. Two pairs of circular compliant electrodes of diameter $d_0 = 24$ mm are deposited onto the two sides of a circular 200 μm-thick Elastosil P7670 silicone membrane with outer diameter $D = 50$ mm, by smearing a carbon-based conductive grease (Nyogel 753G) using a Q-tip and an adhesive shadow mask. Carbon grease electrodes are preferred because they support very high deformations while remaining conductive and providing good homogeneous coverage. This allowed application of all electrodes onto the elastomer in the unstretched state. Moreover, their high viscoelasticity does not represent a problem in static actuation tests. The circular membrane is equi-biaxially stretched to several different pre-stretches $\lambda_p = d_1/d_0$, d_1 being the elec-

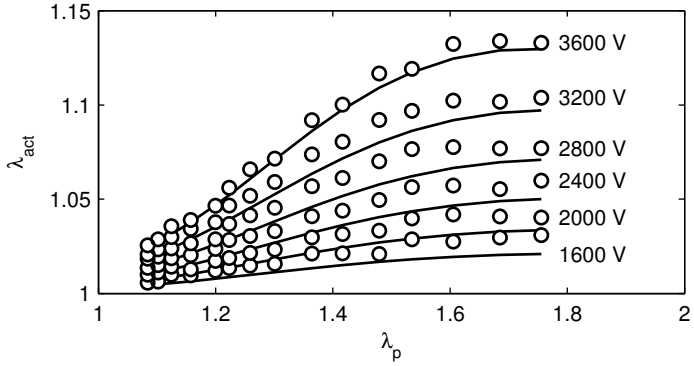

Figure 3.12: Active stretch λ_{act} as a function of the equi-biaxial pre-stretch λ_p. Symbols: experimental data; solid line: prediction of Equation 3.7.

trode diameter after being pre-stretched. At each given pre-stretch the voltage difference Φ across the electrodes is stepwise increased from 0 to 3600 V, causing the electrode area to expand to a diameter d_{act} (Figure 3.11). The active stretch is defined as $\lambda_{\mathrm{act}} = d_{\mathrm{act}}/d_1$. An overhead mounted CMOS camera (Nikon D3000, 3.872 × 2.592 pixels, Nikon 85 mm AF micro NIKKOR f/2.8D lens) is used to record the undeformed, pre-stretched and active electrode area. An automatic post-processing procedure, developed in MATLAB and relying upon the MATLAB imaging toolbox, effectively computes the diameters d_1 and d_{act} in a three-step procedure.

The greyscale image is converted into a binary image, blackening pixels whose brightness is below a certain threshold. The choice of this threshold has little influence on the result, thanks to the strong contrast between the electrode area and the background. The coordinates (x_i, z_i) of the electrode boundary are detected and the best-fitting circumference passing through them is computed in a least squares sense. Finally, outliers lying more than two standard deviations away from the circumference are statistically eliminated, starting from the most unlikely value, and the best-fit circle is iteratively recomputed after each removal, until no outlier is detected. The difference between the present experiment and the actuation scenario described by Equation 3.7 is the boundary condition at the side of the membrane: in the former the radial and tangential stresses at the boundaries of the active electrode vary upon actuation and are equal to the

restoring elastic stresses of the inactive part of the membrane; in the latter a constant pre-stretch force is applied, which results in increasing stresses for increasing thinning of the elastomer. However, it must be noted that in the unactuated case the boundary conditions at the electrode border are completely equivalent in both cases.

Figure 3.12 shows the measured (symbols) active stretch against the pre-stretch for various actuation voltages, together with the prediction (solid lines) of Equation 3.7. In spite of the slightly different boundary conditions, the experiment and analytical solution show good agreement, both exhibiting a plateau at high pre-stretches for low-voltage curves, after which increasing pre-stretch at constant voltage does not improve the active stretch λ_{act} any further. At higher voltages, the scenario is slightly different and an optimal pre-stretch of about $\lambda_p = 1.75$ appears to exist, which represents the maximum active stretch at a given voltage Φ. This experimental result can be explained as follows. Pre-stretching the elastomeric film changes its geometric properties, namely reduces its thickness y and extends its diameter d. If a constant voltage is maintained during pre-stretching, the electric field $E = \Phi/y$ increases as the elastomer thickness decreases, inducing a steep rise of the Maxwell pressure $p_e = \epsilon_0\epsilon_r(\lambda_{\mathrm{act}}\lambda_p)^4\,(\Phi/y_0)^2$. On the other hand, from low to moderate stretches the elastic response of the elastomer is almost linear, which yields large λ_{act} in order to preserve equilibrium.

The stretch/strain hyperelastic characteristic of the elastomer, shown in Figure 3.13(a), explains the existence of an optimal pre-stretch in the constant-voltage framework. Starting from $\lambda \approx 1.7$ the elastomer stiffness steeply increases, owing to the approaching limiting stretch. In this range the elastomer easily balances an increase of Maxwell stresses with a fairly low additional deformation.

In the literature, the beneficial effect of stretching has often been erroneously motivated [21, 57, 58], asserting that a fairly low amount of pre-stretch moves the working point to a less steep portion of the stretch/strain curve, such as the one of Figure 3.13(a). However, the initial flattening of the engineering stress/strain characteristics of most elastomers is an artifact that originates from referring the stress to the initial undeformed area of the elastomer and does not correspond to a real softening. This can be verified by computing the real stress/strain characteristic (Figure 3.13(b)), which exhibits a linear behavior up to $\lambda \approx 1.7$, where the typical stiffening of many polymeric materials occurs.

The real effect of the pre-stretch can be evaluated in Figure 3.14, where the active stretch is plotted against the electric field $E = \lambda^2\Phi/y_0$. A com-

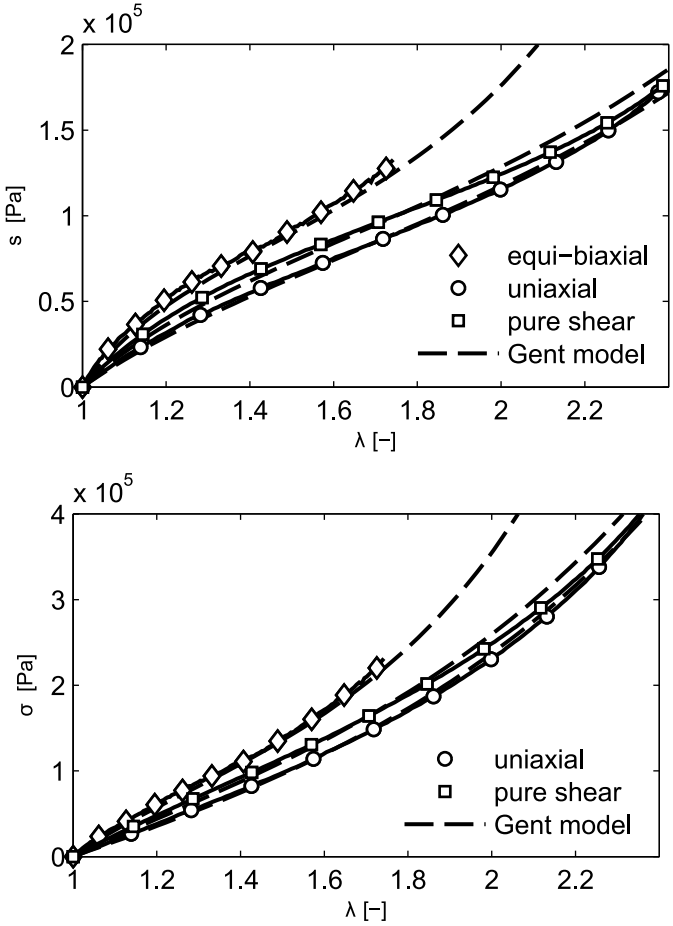

Figure 3.13: Engineering (a) and true (b) stress - strain curves for the three typical load configurations in hyperelastic characterization.

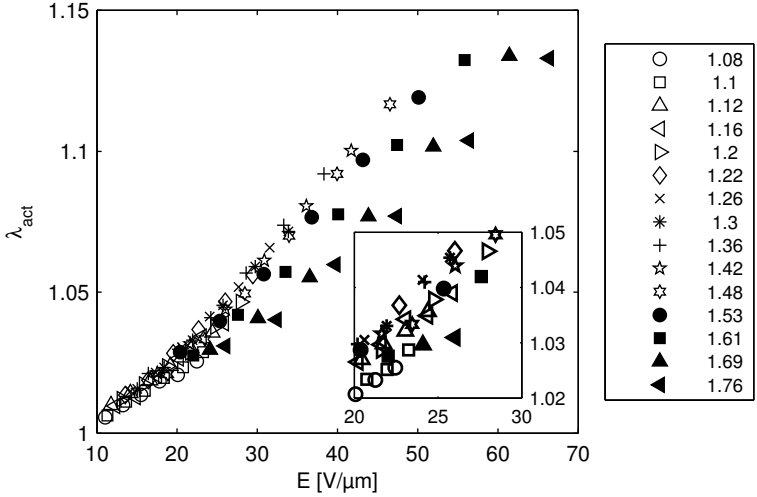

Figure 3.14: Active stretch λ_{act} against the imposed electric field $E = \lambda^2\Phi/y_0$ for several equi-biaxial pre-stretch ratios.

pletely different picture emerges once the purely geometric effects are removed. Pre-stretches between 1.2 and 1.3 reach the highest λ_{act} for a given constant electric field (and hence electrostatic stresses). Moreover, Figure 3.14 clearly shows how specimens at high pre-stretches achieved a higher field strength, thanks to the stretch-induced increase in the dielectric breakdown field strength.

In conclusion, the present investigation shows that a fairly low level of pre-stretch ($\lambda_p = 1.2 \div 1.3$) improves the actuation stretch of the Elastosil P7670 silicone elastomer, essentially agreeing with the theoretical analysis of Akbahri *et al.* [3]. Highly pre-stretched specimens required higher electric field strengths E than their lower stretched counterparts, in order to achieve a given active stretch λ_{act}. However, their concomitantly higher dielectric breakdown strength allows the imposition of higher electric fields, possibly leading to improved actuation. It is therefore important to investigate the combined effects of the pre-stretch on dielectric properties and electromechanical coupling, as done for instance in Figure 3.9, which indeed confirms the present experimental results and predicts improved performance at low voltages for $\lambda_p = 1.2$.

3.3.3 Dynamic actuation

Although the effects of pre-stretch on static actuation have been widely investigated in the literature, mostly focusing on the electromechanical instability (EMI) [174], its influence on dynamic actuation has received much less attention. Recent contributions to the topic are those by Mockensturm & Goulbourne [109], Rosset *et al.* [142], Hodgins *et al.* [63] and Sheng *et al.* [147].

In the following, a simple, planar membrane actuator is chosen as a model tool to experimentally investigate the effect of varying the in-plane pre-stretch on dynamic actuation. The model actuator is a precursor of the final actuator developed for exerting in-plane wall oscillations aimed at turbulent skin-friction drag reduction.

The actuator and the experimental setup are sketched in Figure 3.15. An

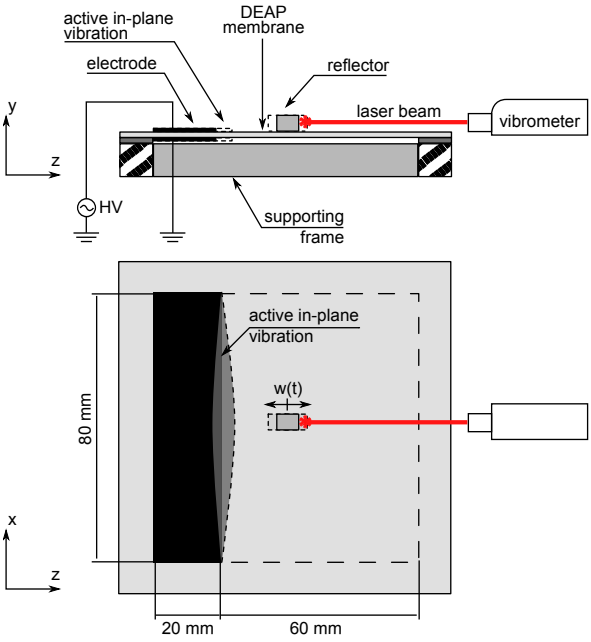

Figure 3.15: Experimental setup for the dynamic characterization of dielectric elastomer membrane actuators.

initially 200 μm-thick membrane of the Elastosil P7670 silicone elastomer is anisotropically pre-stretched in the two planar directions x and z by means of a self-made 4-clamp pre-stretch jig. A 50 mm×50 mm square is painted onto the 120 mm×95 mm PDMS unstretched film to verify homogeneity and the amount of imposed pre-stretch. The stretched membrane is glued onto a square polyvinylchlorid (PVC) supporting frame of 80 mm×80 mm inner size, covered with the special acrilate/silicone, 3M™ 9731 double-sided tape and endowed with thin aluminium contact lines. One electrode on the top and bottom face of the dielectric elastomer membrane is brought by brushing graphite flakes (MF2, NGS Naturgraphit GmbH) onto a surface with a Q-tip and a loosely adhesive mask. The electrodes cover one side of the membrane and lie against the supporting frame. Their width (z-direction in Figure 3.15) is 20 mm and length (x-direction) is 80 mm, i.e. the whole length of the membrane. Carbon electrodes based on loose particles are chosen, as they practically do not stiffen the electrode, add negligible mass and are not viscoelastic [145]. However, their sheet resistivity increases exponentially with the stretch [99] and makes them a viable choice only for active strains below 20%, nevertheless a relatively high value for silicone elastomers in dynamic actuation. While able to resist the active strain, the loose graphite electrode would not guarantee coverage and conductivity if prior pre-stretching was imposed. Therefore, electrode deposition has been conducted after pre-stretch. The thickness of the actuator membranes are measured with a thickness screw gauge at the end of the actuator fabrication process.

A square membrane actuator very similar to the present one can be found in the seminal paper of Perline *et al.* [119], where it is described as one of the most simple forms of a DEA. Figure 3.15(b) shows the actuation principle: upon activation, the electrode area expands, mainly in the z-direction due to the imposed boundary conditions, increasing its original stretch. The inactive area, where no electrodes are deposited, must reduce its length, thus relaxing part of the initial pre-stretch. Upon imposition of an AC voltage difference across the electrodes, a periodic deformation of the elastomeric membrane is achieved.

The influence of certain pre-stretch combinations on the frequency response of the membrane actuator are studied by producing several actuators at different pre-stretches. A chirp signal, increasing its frequency f_e at 0.5 Hz/s from 1Hz to 200 Hz, is amplified to a high voltage signal by a Trek 609-E high-voltage amplifier and fed to the membrane actuator. Its amplitude is adapted case by case to yield a constant maximum electric field

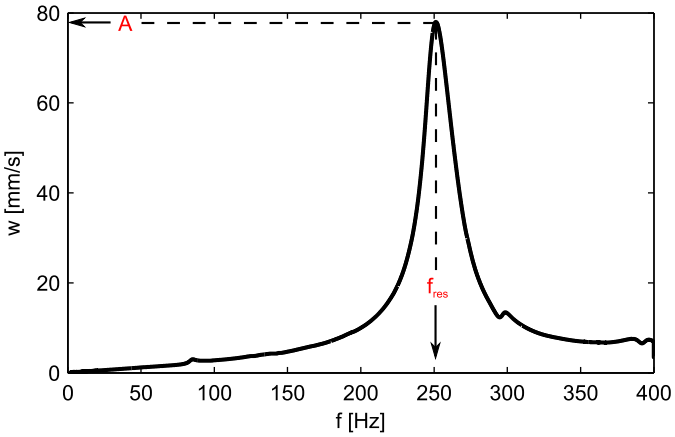

Figure 3.16: Dynamic response of a dielectric elastomer membrane actuator as maximum velocity w [mm/s] against the frequency of oscillation f [Hz].

strength of 15 V/μm among different actuators, according to their membrane thickness. The Maxwell pressure is proportional to the square of the impose electric field, therefore the mechanical response of the actuator to an excitation at frequency f_e has a frequency $f = 2f_e$. A laser Doppler vibrometer (Polytec OFV-3001 controller with OFV-534 measuring head) measures the active displacement by tracking the velocity w [mm/s] of a small 125 mm^3 balsa wood dice, located at the center of the membrane and covered with an adhesive reflective paper.

Figure 3.16 shows a typical dynamic response of the membrane actuator, similar to the one of an underdamped, mass-spring-damper mechanical system. The actuation speed increases linearly with the frequency, meaning constant displacement, up to the neighborhood of the resonance frequency f_{res}, where the maximum amplitude A of oscillation is reached. At resonance, a large planar displacement of the whole dielectric elastomer membrane is observed. It is clear that, in order to maximize performance and amplitude of actuation, the actuator needs to be excited at its mechanical resonance frequency. Therefore, the mechanical resonance frequency f_{res} and the maximum amplitude (velocity) of oscillation A are chosen as indicators for evaluating dynamic performance at various combinations of $\lambda_{\text{p,x}}$

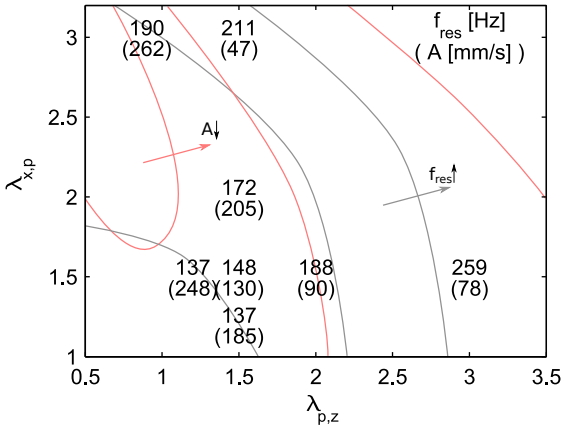

Figure 3.17: Resonance frequency f_{res} [Hz] and maximum amplitude of oscillation A [mm/s] for several combination of $\lambda_{p,x}$ and $\lambda_{p,z}$, the pre-stretch in x- and z- direction respectively.

and $\lambda_{\text{p,z}}$, the pre-stretches along the x- and z- directions respectively.

Similar to static actuation, dynamic actuation is significantly altered by a change of pre-stretch, as the results in Figure 3.17 show. When $\lambda_{\text{p,z}}$, the pre-stretch along the main direction of actuation (Figure 3.15), is increased at constant $\lambda_{\text{p,x}} = 1.5$, a rapid increase of f_{res} is observed, which almost doubles from 137 Hz at $\lambda_{\text{p,z}} = 1.2$ to 259 Hz at $\lambda_{\text{p,z}} = 3$. At the same time, the maximum amplitude of oscillation A reduces to about 1/3 of the value at low pre-stretches. A similar behavior occurs if $\lambda_{\text{p,z}} = 1.5$ is kept constant and $\lambda_{\text{p,x}}$ is increased, yet with a milder improvement of f_{res}. More interesting is the combination of very low pre-stretches in the z-direction $\lambda_{\text{p,z}} \leq 1$ and high pre-stretches in the x direction $\lambda_{\text{p,x}} = 3$. Here, both f_{res} and A are improved, being an interesting combination for dynamic applications where high deformations are desired.

Once again, the principal consequence of pre-stretching is a change in the elastomer geometry. The area density of the membrane actuator decreases with the pre-stretch, as:

$$\rho_e y = \rho_e \frac{\lambda_x \lambda_z}{y_0} \tag{3.8}$$

where ρ_e is the density of the elastomer (approximately 1.05 g/m^3). As a result of the reduced area density, the mechanical resonant frequency

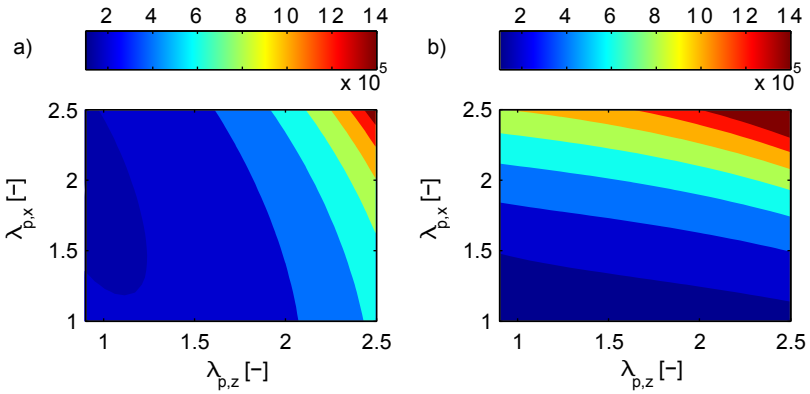

Figure 3.18: Contours of the linear elastic modulus $E_{\mathrm{lin,z}}$ and the pre-stress $\sigma_{p,x}$ for varying pre-stretch ratios $\lambda_{\mathrm{p,x}}$ and $\lambda_{\mathrm{p,z}}$.

increases. Equation 2.61, describing the deformation of a cuboid DEA, is differentiated to compute a local linear elastic modulus

$$E_{\mathrm{lin,z}} = \left.\frac{\partial \sigma_z\left(\lambda_x, \lambda_z\right)}{\partial \lambda_z}\right|_{\Phi=0} \tag{3.9}$$

which is representative of the stiffness in the z-direction after anisotropically pre-stretching. The contours of $E_{\mathrm{lin,z}}\left(\lambda_x, \lambda_z\right)$ are shown in Figure 3.18(a). A region of high $\lambda_{\mathrm{p,x}}$ and $\lambda_{\mathrm{p,x}}^{-1/2} < \lambda_{\mathrm{p,z}} < 1$ exists, where the stiffness in z-direction is lower than the one exhibited by the elastomer at both the unstretched and highly stretched state. Pre-stretch combinations that lie in this region yield higher active stretches, as the data point at $\lambda_{\mathrm{p,x}} = 3$ and $\lambda_{\mathrm{p,z}} = 0.9$ in Figure 3.17 shows. The reduction in stiffness for very low $\lambda_{\mathrm{p,z}}$ is milder than the geometric effect of pre-stretching, which explains how an active stretch and resonant frequency could be increased at the same time.

3.4 The dynamic actuation process

The present section focuses on the main phenomena underlying dynamic actuation of the dielectric elastomer membrane actuator presented in Section 3.3.3. Instead of assessing the actuation process in terms of few indicators,

such as the maximum speed at a given point or the resonance frequency of the system, the short- and long-term deformation of a wide portion of the membrane is observed, in order to gain insight into the transient and fast response to dynamic excitation.

The experimental setup adopted in the present investigation is shown in Figure 3.19. The actuators developed in Section 3.3.3 undergo an additional preparation step. A 10 × 20 array of 1 mm-diameter dot markers is deposited onto the inactive part of the dielectric membrane by spraying the mixture of graphite flakes (MF2, NGS Naturgraphit GmbH) and isopropyl alcohol also utilized for patterning compliant electrodes. A 100 μm-thick steel shadow mask is used for structuring the marker array. A distance of 4 mm is observed between the centers of two adjacent markers. An over-

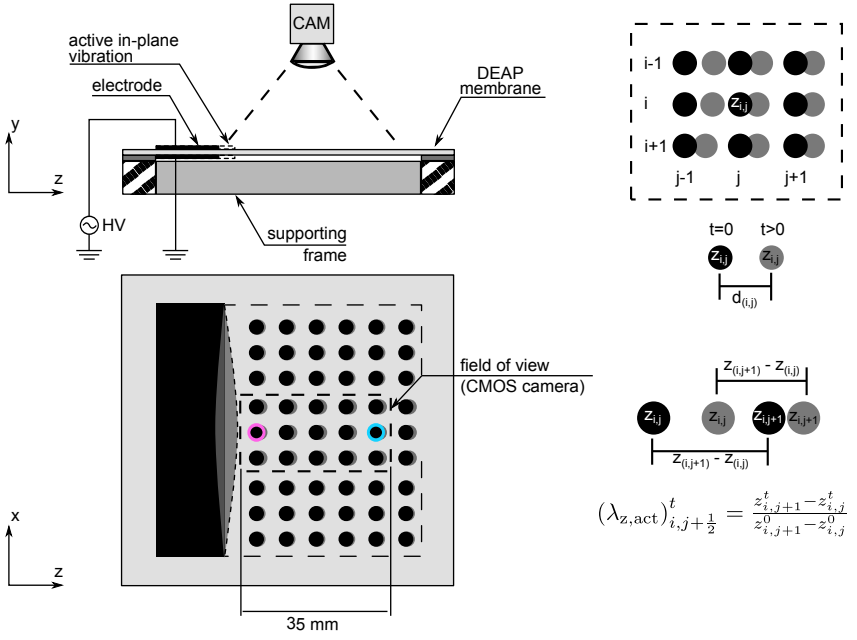

Figure 3.19: Experimental setup for the space and time characterization of the membrane active deformation. An overhead camera (CAM) is used to track the displacement of a marker array. The main derived quantities by post-processing are graphically explained.

head high-speed CMOS camera (Mikrotron MotionBLITZ Cube 4, 1280 × 1024 pixels, 12 x 12 μm pixel size, mounting a Nikon 85 mm AF micro NIKKOR f/2.8D lens with a 28mm extension tube) acquire images of the membrane during actuation at 7000 frames per seconds (fps) with a resolution of 50 μm. Sufficient illumination is provided by an off-the-shelf 13W LED-lamp, located below the membrane, thus improving contrast between the transparent membrane and the dark graphite-covered marked regions.

An ad-hoc, automatic, post-processing procedure is developed to track the position of each marker during actuation and thus obtain a 2D active displacement field. At each timestep, the greyscale frame is converted into binary image, blackening pixels whose brightness is below a certain threshold. The choice of this threshold has little influence on the result, thanks to the strong contrast between the electrode area and the background. Connected regions, the markers, are found through a flood-fill algorithm and their centroid is defined as the marker mid-point. The marker centers are stored after being sorted in a two dimensional array, according to their initial position, following the scheme sketched in Figure 3.19. The center position $\mathbf{r}_{i,j}^t$ of a marker belonging to the i-th row and j-th column at time t is:

$$\mathbf{r}_{i,j}^t = \left\{ x_{i,j}^t, \quad z_{i,j}^t \right\}^T \tag{3.10}$$

Once the position in time of each marker center is educed, two useful quantities can be derived: the displacement and the local stretch. The displacement vector $\mathbf{d}_{i,j}^t$ maps the active displacement of the (i,j)-th discrete marker respect to its initial position in the unactuated state at time $t = 0$ and reads:

$$\mathbf{d}_{i,j}^t = \mathbf{r}_{i,j}^t - \mathbf{r}_{i,j}^0 = \left\{ x_{i,j}^t - x_{i,j}^0, \quad z_{i,j}^t - z_{i,j}^0 \right\}^T \tag{3.11}$$

The local stretch $\lambda_{z,\mathrm{act}}$ is an estimation of the local state of stretch in the z-direction obtained by comparing the position of two neighboring markers as follows:

$$\left(\lambda_{z,\mathrm{act}}\right)_{i,j+\frac{1}{2}}^t = \frac{z_{i,j+1}^t - z_{i,j}^t}{z_{i,j+1}^0 - z_{i,j}^0} \tag{3.12}$$

where the subscript $j + \frac{1}{2}$ indicates that the stretch value, derived through Equation 3.12, is spatially collocated at the midpoint between the two neighboring markers j and j+1.

Step response The active dynamic response to an input voltage step is studied first and indeed reveals many interesting aspects. Figure 3.20 shows

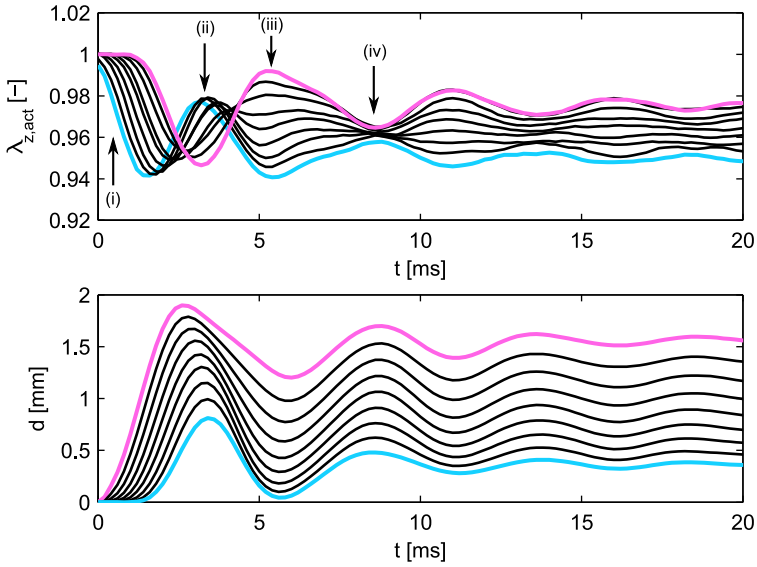

Figure 3.20: Active stretch $\lambda_{z,act}$ (a) and displacement d (b) in actuation direction against time. Cyan line: marker closest to the electrode; magenta line: marker farthest from the electrode; black lines: other markers.

the temporal (and spatial) evolution of the local active stretch $\lambda_{z,act}$ (Figure 3.20(a)) and z-component of the displacement d_z (Figure 3.20(b)). For sake of clarity, only information concerning the central row of markers is shown, without loosing generality. Henceforth, the marker $j = 1$, which is closest to the active electrode, is represented by a cyan line; while the rightmost, the farthest from the electrode area, in magenta. Data corresponding to other markers are shown in black.

The active displacement (Figure 3.20(b)) shows that the region of the membrane close to the active electrode (the magenta marker) reacts first to a step voltage, followed by the rest after a time lag, which linearly increases with the distance from the electrode. After the initial transient, an almost steady state is achieved after about 20 ms, in which the active displacement is nonuniformly distributed throughout the membrane, being maximum close to the electrode and decaying towards the supporting frame, where it is zero. The spatial phase lag of the initial response supports the idea that

a planar acceleration wave exists, which is generated by the initial sudden movement of the activated electrode and travels in the z-direction with a finite speed. This is confirmed from the time history of the local active stretch $\lambda_{z,\mathrm{act}}$ (Figure 3.20(a)). While the initial rate of stretch $\dot{\lambda}_{z,\mathrm{act}} = \mathrm{d}\lambda_z/\mathrm{d}t$ is constant for all markers, the time lag with which a marker is observed to respond to the initial forcing is proportional to its distance from the electrode.

Four phases, marked by arrows in Figure 3.20(a), can be identified in the initial transient response, according to how the traveling acceleration wave interacts with the initial movement:

i the sudden voltage step and consequent electrode displacement generate an acceleration wave that travels along the membrane;

ii the wave reaches the supporting frame, at the opposite side of the electrode, where it is reflected;

iii during its backward travel it interferes with the oscillation of the membrane;

iv the wave has been reflected again and yields to the second elongation of the electrode.

The interference with the acceleration wave is probably the origin of the difference noticed by Rosset *et al.* [142] between the response of a spring-mass-damper system and that of a dielectric elastomer planar actuator.

The traveling acceleration may explain also the existence of the mechanical resonance frequency. The highest mechanical admittance is achieved when the forcing through the imposed AC voltage difference and the traveling wave are in-phase. This condition occurs when the period of forcing equals the time needed by the wave to travel forward and backward to its initial position. Thus, the resonance frequency can be estimated as follows:

$$f_{\mathrm{res}} = \frac{c_w}{2\,(z_{pas})} \tag{3.13}$$

where c_w is the wavespeed and z_{pas} the extent of the inactive area in the z-direction.

In Table 3.1 the resonance frequency measured in Section 3.3.3 is compared to the prediction of equation 3.13. The wavespeed c_w has been computed by shifting the $\lambda_{z,\mathrm{act}}$-curves to find the best match, in a least-square sense, limiting to $\lambda_{z,\mathrm{act}} < 0.96$ (Figure 3.21). The agreement is surprisingly

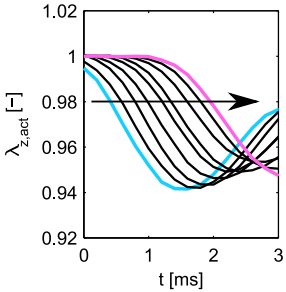

Figure 3.21: Time lag between the onset of strain at different markers after sudden actuation.

$\lambda_{p,x}$	$\lambda_{p,z}$	f_{res} [Hz]		
		exp	Eq. 3.14	Eq. 3.13
1.2	1.5	140	138	147
1.5	2.0	160	170	172
0.9	3.0	190	190	179

Table 3.1: Mechanical resonance frequency of the membrane actuator at various pre-stretches. Experimentally-measured value (Exp) is compared to the prediction of Equations 3.14 and 3.13.

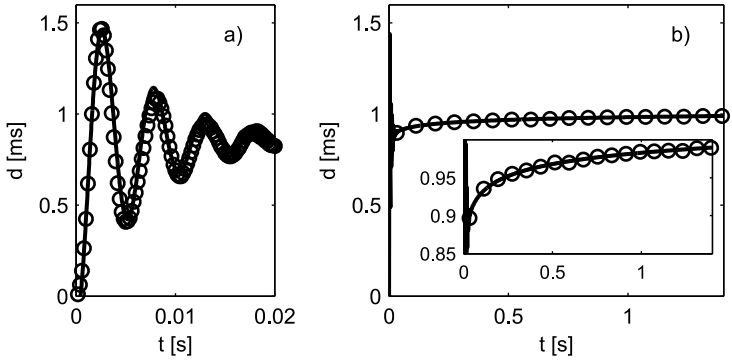

Figure 3.22: Short term (a) and long term (b) response to a voltage step at the center of a dielectric elastomer membrane actuator. Symbols: undersampled experimental data; solid line: Equation 3.14.

good and not expected to be spot-on, due to the difficulty in accurately measuring c_w, which range between 18 and 22 m/s.

Figure 3.22(a-b) shows the short-time and long-time response to a voltage step at the center of the membrane. After 20 ms the active displacement seems to have settled to the final steady value of static actuation. However, if the time window is enlarged to 1.5 s, a much slower, viscoelastic response appears, during which the displacement increases of further 20%. Rosset *et al.* [142] modeled the local dynamic response by combining the canonical solution of a spring-mass-dashpot mechanical system with an additional term in charge of accounting for viscoelastic creeping, as follows:

$$\frac{d(t)}{d_{\max}} = \left[1 - c_1 \frac{e^{-\xi\omega_0 t}}{\sqrt{1-\xi^2}} \sin\left(\omega_0\sqrt{1-\xi^2} + c_2\right)\right]\left(1 - e^{\frac{-tc_3}{c_4}}\right) \tag{3.14}$$

where $d_{\max}$ is the maximum local displacement, $\omega_0 = 2\pi f_0$ is the natural angular frequency of the undamped system, ξ is the damping coefficient. c_1, c_3 and c_4 are empirical coefficient obtained through fitting of the experimental data, while $c_2 = \tan^{-1}(\sqrt{1-\xi^2}/\xi)$. The resonance frequency of the damped system can be deduced from Equation 3.14 as:

$$f_{\text{res}} = \sqrt{1-2\xi^2} f_0 \tag{3.15}$$

and is reported in Table 3.1, along with the experimentally measured value. Rosset *et al.* [142] reported a slight disagreement between Equation 3.14 and the short-time response of a dielectric silicone membrane actuator, which has been also observed here whenever fitting the response of markers close to the electrode (not shown). However, the response at the center of the membrane is almost perfectly fitted by Equation 3.14, as shown in Figure 3.22(a-b).

Resonant response A fast, large, planar and practically unidirectional periodic oscillation is achieved by the dielectric elastomer membrane actuator under excitation at its mechanical resonant frequency.

Figure 3.23 presents the time-resolved displacement for the central row of markers aligned with the z-direction. The actuator, with pre-stretches $\lambda_{p,x} = 2$ and $\lambda_{p,z} = 1.5$, is excited at its resonant frequency $f_{\text{res}} = 160$ Hz and exhibits a maximum peak-to-peak displacement of 5.7 mm, corresponding to 23 % active strain.

The active displacement is not homogeneous throughout the membrane: it is maximum at the center, decreasing towards the borders, where it must

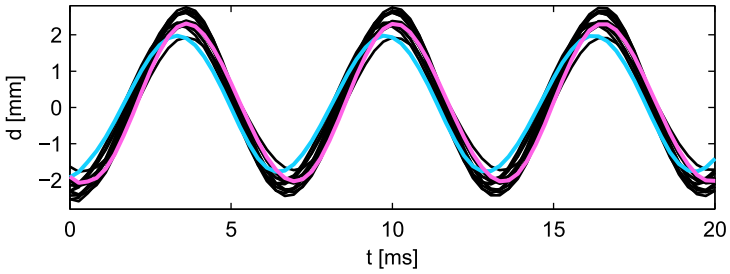

Figure 3.23: Resonance response of the membrane actuator: active stretch $\lambda_{z,act}$ (a) and displacement d (b) against time. Cyan line: marker closest to the electrode; magenta line: marker farthest from the electrode; black lines: other markers.

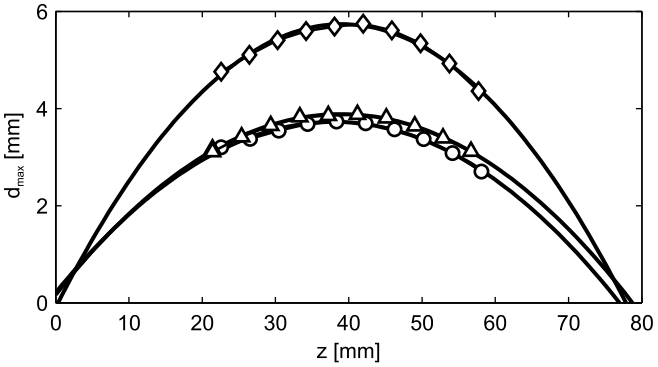

Figure 3.24: Local maximum deformation d_{max} at resonance at various position in the actuation direction.

be zero. Figure 3.24 shows the maximum achieved peak-to-peak active deformation along a z-slice of the membrane. The data for three different actuators cover only the non-electroded central region of the membrane, which corresponds to the field of view of the high-speed camera. However, in all cases a parabola fits the experimental data remarkably well, suggesting that the maximum active displacement quadratically increases towards the center of the membrane. A similar behavior is observed in the x-direction.

In conclusion, the simplest membrane actuator can already realize fast and large wall oscillations at frequencies above 100 Hz, and thus meets the requirements for low-speed wind-tunnel testing of turbulent drag reduction via spanwise wall forcing. However, the oscillations are not spatially homogeneous, which may represent a limitation for flow-control applications, where homogeneous oscillations are usually assumed. Particularly critical is the inhomogeneity of the oscillation amplitude along the direction of actuation, which generates wall-normal velocity components, as will be discussed in Chapter 5.

3.5 Spanwise oscillating actuators

The knowledge gathered throughout this Chapter is exploited in the following to design actuators capable of exerting unidirectional (spanwise) wall oscillations, eligible for laboratory implementation of turbulent flow control. First, the fabrication process is described, focusing on the most critical steps that may influence the reliability of the actuator. Then, the electromechanical characterization is performed, in order to compute the power consumption, input power, and some electromechanical characteristics that impact on the actuator performance.

3.5.1 Fabrication

The actuator system designed in the present work is a further development of the building block analyzed in Sections 3.3.3 and 3.4. It is based on the original two-phase, planar actuator concept presented by Pelrine *et al.* [119] and first used by Gouder *et al.* [58] for flow control applications.

Two different actuator models, named WT1 and WT2, are produced for wind-tunnel testing. They share most design parameters, except for their slightly different final size. A detailed description of the fabrication of WT1

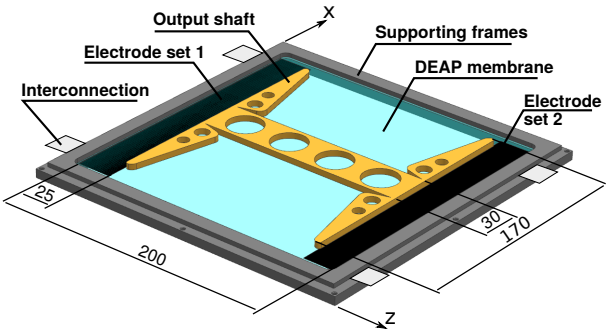

Figure 3.25: Sketch of the DEA drive unit of a WT1 actuator. Dimensions in mm.

actuators follows, while the description of the few geometrical differences are demanded to Figure 3.28.

A 270 mm × 250 mm membrane of the dielectric silicone elastomer Elastosil Film (Wacker Chemie), initially 100 μm thick, is anisotropically pre-stretched with a four-clamp rectangular pre-stretch jig in the two perpendicular planar directions, z and x, here after called the longitudinal and transverse direction respectively. Elastosil Film has been preferred to Elastosil P7670 since its availability, as it is delivered as a roll of high-purity, high-quality silicone film, immediately exhibited high robustness and performance. The main steps of the fabrication process are sketched in Figure 3.27(a-f), together with a schematic of the pre-stretch jig.

A 230 mm × 210 mm square marker is painted onto the silicone unstretched film to verify homogeneity and amount of pre-stretch. The pre-stretch ratios in the longitudinal and transverse direction are $\lambda_z = z/z_0 = 1.0$ and $\lambda_x = x/x_0 = 1.75$ respectively. The high pre-stretch ratio λ_x pre-load and stiffen the elastomer in the transverse direction and therefore hinders any field-induced deformation, which occurs mostly in the less pre-stretched longitudinal direction. Combined with a low pre-stretch in the longitudinal direction has been shown to improve the dynamic performance (Figure 3.3.3) of the DEA. The thickness of the elastomer after being pre-stretched is about 56 μm, as measured with a thickness screw gauge. A mixture of graphite and isopropyl alcohol is brushed onto the membrane with a Q-tip at particular positions, in order to create a thin conductive bridge between

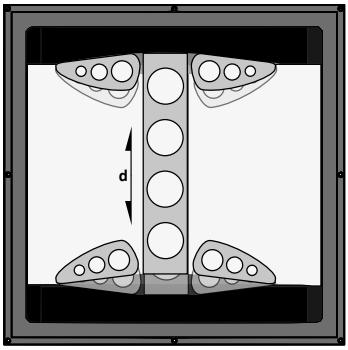

Figure 3.26: Sketch of the active displacement during push-pull periodic excitation.

the compliant electrodes and the leading wires.

The stretched membrane is glued onto two square PMMA (polymethylmethacrylat) frames of 200 mm × 200 mm internal size and 20 mm width, covered with the special acrilate/silicone, 3M 9731 double-sided tape and endowed with thin aluminium contact lines. The contact between the aluminium lead and the graphite contact bridges should occur between the two PMMA frames, as the stiff, thin and sharp aluminium lead could damage the active dielectric elastomer membrane by abrasion or through electric sparks. Small amounts of the low viscosity, two component liquid silicone Elastosil P7670 (Wacker Chemie) is cured at room temperature to repair small imperfections on the membrane, visible by simple inspection. The treatment reduced premature failure of the actuators during their preliminary testing.

Two pairs of electrodes, 25 mm wide and 185 mm long, are brought onto both faces of the silicone membrane, along the two opposite sides of the frame aligned with the transverse direction, by manually sputtering graphite flakes (MF2, NGS Naturgraphit GmbH) with a Q-tip and the aid of an adhesive shadow mask to obtain sharp electrode edges. The overlap region of the top and bottom electrode is 25 mm × 170 mm and constitutes the active region. The electric interconnection between the graphite electrodes and the aluminium foil electric lines occurs between the two plastic frames in a region where top and bottom electrodes do not

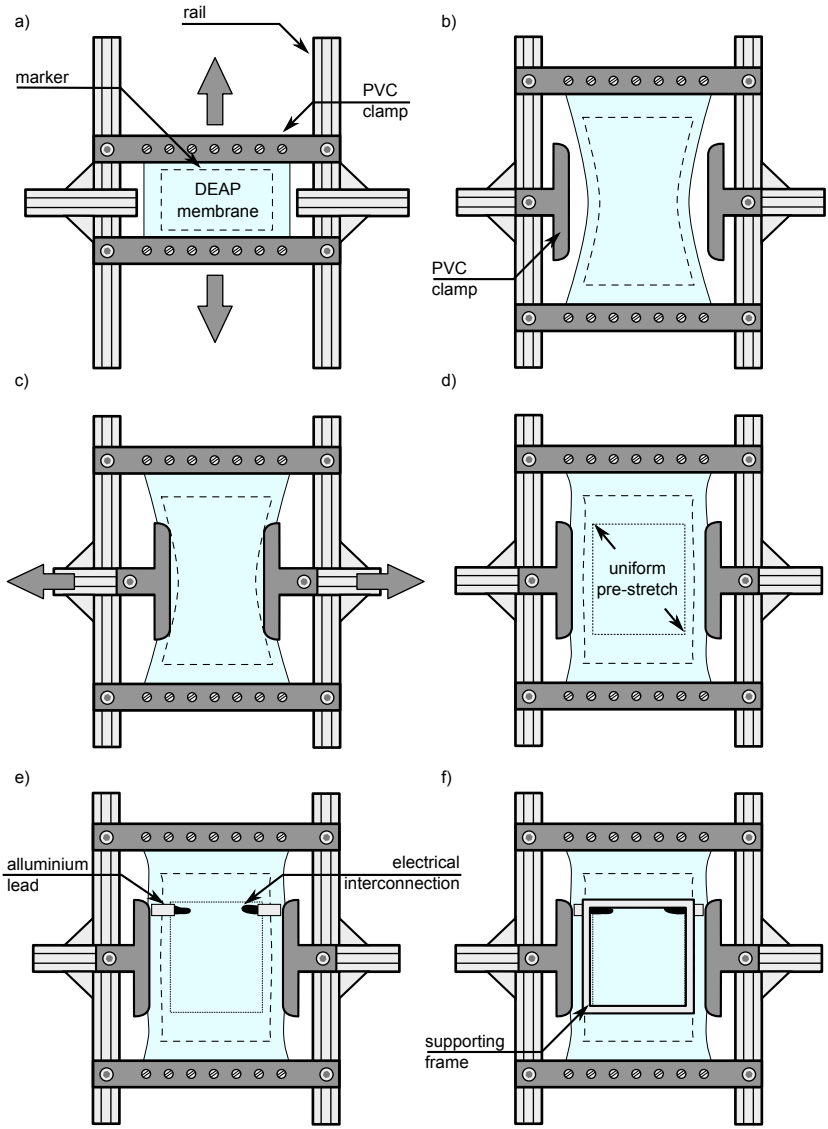

Figure 3.27: Main steps of the actuator fabrication process.

overlap.

A 4 mm thick, lightweight, balsa-wood output shaft, shaped as suggested by Gouder *et al.* [58], is glued with the same two-component liquid silicone, in order to ensure a soft and stable contact region, onto the dielectric elastomer membrane, so as to couple the movement of the two electrode active areas. The fabrication process takes approximately 3 h of manual work per actuator, plus an additional 1 h for the first electromechanical testing before proceeding to the integration into the wind tunnel.

The final actuator is sketched in Figure 3.25, where also the composing parts are indicated along with their size. The main difference with the actuator configuration studied in Section 3.4 is the presence of a mechanical part, the output shaft, which directly couples the displacement of the electrode sets. It is worth noting that in-plane actuation is obtained also without the output shaft, as obtained in Section 3.4. Its presence is mainly required as out-of-plane stiffener.

The DEA drive unit is mounted onto a PVC plate and combined with a passive flush-mounted surface to form the actual oscillating wall exposed to the air flow (Figure 3.28). The passive surface is made up of an initially 50 μm-thick silicone membrane, equi-biaxially pre-stretched to $\lambda_x = \lambda_z = 1.3$, bound onto a 26 mm-wide square plastic frame with a special double-sided tape. The elastomer and the double-sided tape used here and in the active drive unit are of the same kind. A 200 mm × 200 mm stiff polyethylene plate of 150 μm thickness is brought onto the inner face of the passive membrane, onto which it spontaneously stick (Figure 3.29). Trapped air bubbles are removed. The role of the stiff plate is to produce a homogeneous region of the passive membrane that moves homogeneously in the spanwise direction. The stiff plate is finally coupled with the output shaft of the drive unit with a general purpose spray adhesive.

Figure 3.28 also shows the main differences between WT1 and WT2 actuators, with the latter featuring a slightly larger outer frame compared to the stiff plate and the drive unit. This characteristic eases the installation into the wind tunnel and enables the achievement of larger deformations at lower applied voltages, thanks to the reduced shear forces that are generated between the outer frame and the (moving) stiff plate.

3.5.2 Electromechanical characterization

Figure 3.26 shows the active actuator displacement. Upon static actuation of one electrode set, the underlying elastomer is squeezed by the Maxwell pressure, resulting in lower tensile stresses on the activated area. As a

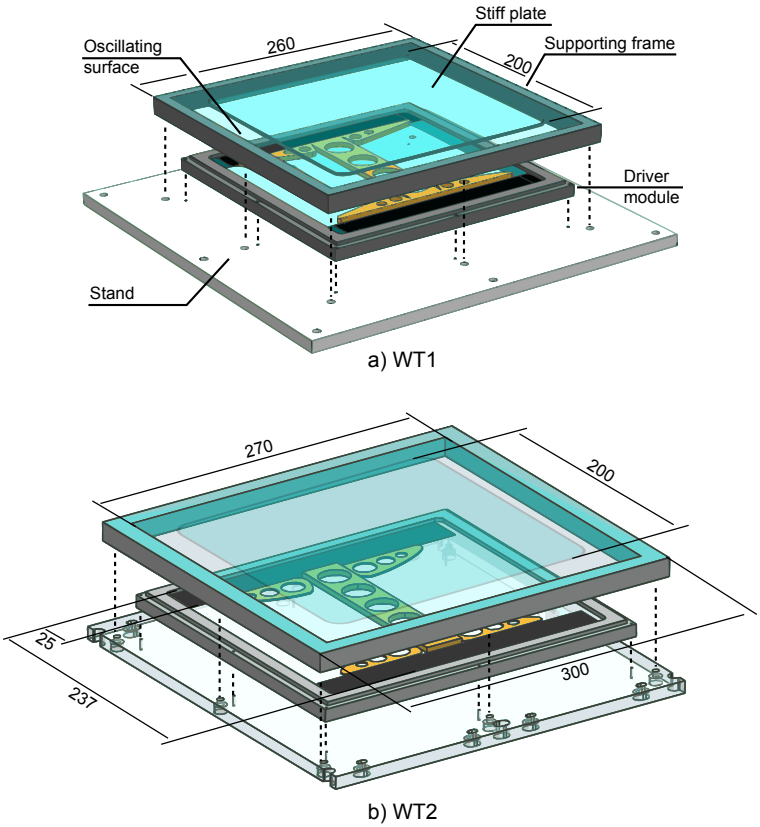

Figure 3.28: Exploded view of the drive unit combined into the oscillating surface assembly for WT1 (a) and WT2 (b) actuators. Dimensions in mm.

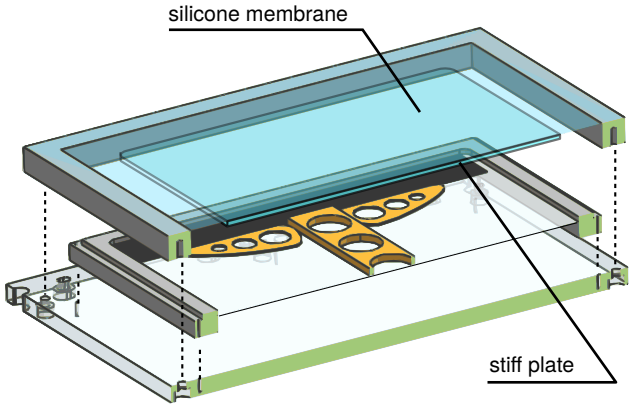

Figure 3.29: Cross-setional exploded view of the complete WT2 actuators.

consequence, the shaft moves towards the non-activated side to restore equilibrium. A large periodic oscillation of the output shaft with peak-to-peak displacement d and velocity amplitude A at frequency f is achieved by imposing on the two electrode sets two push-pull, DC-shifted, sinusoidal high-voltage signals as follows:

$$\Phi_1 = \frac{\Phi}{2} + \frac{\Phi}{2}\sin(2\pi f) \tag{3.16}$$

$$\Phi_2 = \frac{\Phi}{2} + \frac{\Phi}{2}\sin(2\pi f + \pi) \tag{3.17}$$

where Φ_1, Φ_2 are the potential differences between the electrodes of the first and second set respectively and Φ is the maximum applied voltage.

Mechanical response The dynamic response of a WT1 actuator, shown in Figure 3.30(b), is measured at the output shaft with a laser Doppler vibrometer (Polytec OFV-3001 controller with OFV-534 measuring head) while a chirp signal, from 10 to 100 Hz with rate 1Hz/s and maximum voltages 1500 and 2000V, is applied in a push-pull manner at both electrodes. The actuator shows a strongly underdamped response with maximum oscillation velocity A_{res} at the resonant frequency $f_{\text{res}} \approx 75$ Hz.

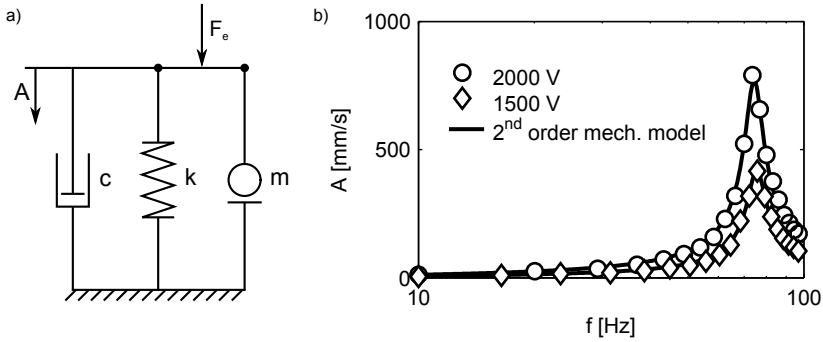

Figure 3.30: (a) Phenomenological mechanical model of the actuator. (b) Dynamic response of the actuator: oscillation amplitude A (mm/s) against frequency f (Hz) at two different actuation voltages.

Phenomenologically, this behavior can be modeled as a spring-mass-dashpot system, shown in Figure 3.30(a), governed by the following equation:

$$\frac{F_e(j\omega)}{A(j\omega)} = Z_{\text{mech}} = j\omega m + c + \frac{k}{j\omega} \tag{3.18}$$

where j is the imaginary unit, F_e is the applied electrostatic force and A is the amplitude of oscillation. The argument $(j\omega)$ is chosen to highlight response in the frequency domain. The parameters m, c and k are respectively the lumped effective mass, damping and stiffness of the actuator. They are found through least-square fitting of Equation 3.18 to the experimental data. The ratio $F_e(j\omega)/A(j\omega)$ represents the complex mechanical impedance of the system Z_{mech}. As Figure 3.30(b) shows, the phenomenological model fits very well the experimental data. However, the damping coefficient c and the stiffness k proved to be mild functions of the applied voltage, which results in a drop of the resonance frequency for increasing voltages.

Electrical response DEAs are attractive for active flow control applications thanks to their relatively low energy consumption and high power density compared to other traditional technologies, such as electromagnetic linear motors or piezoelectric devices. In fact, the actuator shown in Figure 3.25 can be electrically outlined as a standard RC circuit, where the serial

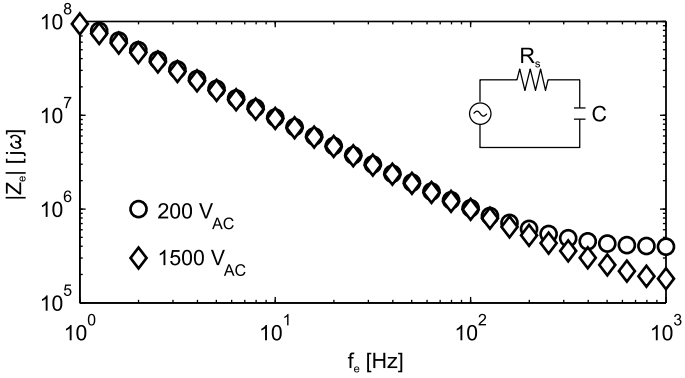

Figure 3.31: Modulus of the electrical impedance $|Z_e|$ $(2\pi f_e)$ as a function of the actuation frequency f_e (Hz) for two actuation voltages.

resistance R_s consists of the interconnection resistance and the electrode resistance, and the capacitance C refers to the actual active deformable capacitor. This can be verified in Figure 3.31, where we report the modulus of the measured electrical impedance $|Z_e(j\omega)|$ against actuation frequency f_e (Hz) and the actuator equivalent circuit. A first-order roll off can be clearly seen up to the electrical limiting frequency, where the actuation period is close to the RC charge-discharge time constant. Together with the mechanical resonance frequency, the RC time constant is another limiting factor for dynamic performance that has to be taken into account during the design phase of the actuator. In fact, the limiting frequency of an RC circuit, beyond which the capacitor can not be charged up to at least 66% of the driving voltage, is $f_{\mathrm{e,lim}} = (2\pi R_s C)^{-1}$.

The electrical impedance of the circuit in Figure 3.31 is:

$$Z_e(j\omega) = \frac{1}{j\omega C} + R_s \tag{3.19}$$

and can be used to compute the capacitance C and serial resistance R_s by fitting the experimental data, which result in to C = 1.69 nF at 400 V and $R_s \approx 200$ kΩ. The capacitance agrees well with the parallel-plate capacitor estimation $C = \epsilon_0 \epsilon_r a_e / y_1$ = 1.7 nF, where a_e is the electrode area and y_1 is the thickness of the membrane after being pre-stretched. The electrical limiting frequency is then $f_{\mathrm{e,lim}}$ = 580 Hz and confirms that the

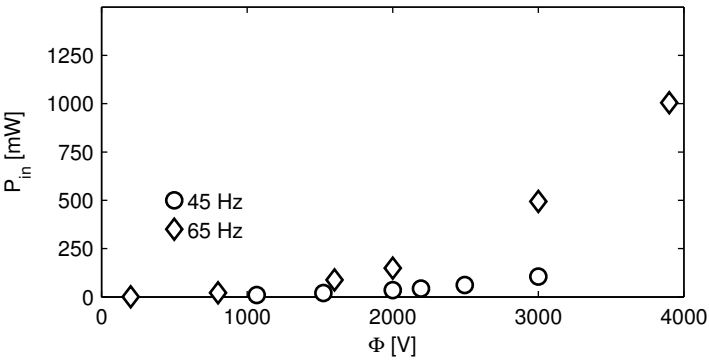

Figure 3.32: Real power P_{in} (mW) against voltage Φ for the WT1 and WT2 actuator at various maximum voltages Φ.

present electrode and contact design is largely sufficient for the present application.

The real power P_{in} required to run both the WT1 and WT2 actuators at their mechanical frequency confirms the expectation and is shown in Figure 3.32 to be in the order of hundreds of mW. In particular, actuators of the WT1 series, due to their higher in-plane stiffness, required to be driven at Φ = 4000 V in order to achieve a sizable oscillation velocity of 820 mm/s. This resulted in a somewhat higher power consumption of 1200 mW compared to about 200 mW for the WT2 actuators, which could be effectively driven starting from Φ = 2000 V.

The input power P_{in} can be further reduced by refining the mechanical design or improving the electrical interconnection, thereby reducing the serial resistance R_s. In fact, energy is dissipated at the electrical interconnection as heat. Figure 3.33 shows a thermographic close-up of the interconnection region. At the interface between the aluminium connector and the graphite electrode the temperature is higher than on the active region and, at high actuation frequency and voltage, it can increase up to 80 °C. This is a site of premature failure if the interconnection conductivity is too low.

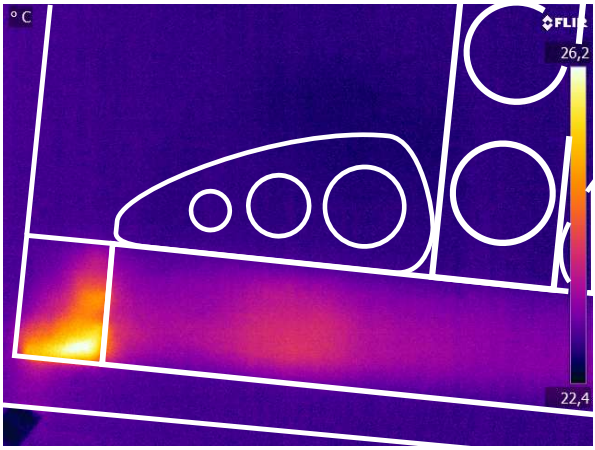

Figure 3.33: Termographic picture of the actuator in the vicinity of an electrical interconnection.

4 Wind tunnel testing of DEA-based spanwise oscillating surfaces

The challenge of achieving an active control technique for turbulent skin-friction drag reduction, which is both practical to implement and exhibits an acceptable net efficiency, is a very important topic in modern fluid-mechanics and aeronautics [28, 49, 62]. On the one hand, space- and timescales of turbulence make the physical parameters of most active controls very difficult to achieve. On the other, novel technologies are needed to develop actuators capable of operating so efficiently that the net power balance between power saved and expenditure is still positive.

Spanwise wall oscillations, in spite of their low theoretical gain, are chosen in this chapter as a model, and they represent a relatively simple technique to evaluate the suitability of dielectric elastomer for turbulent flow control applications. The spanwise oscillating surfaces based on dielectric elastomer actuators, developed in Chapter 3, are tested in a laboratory experiment conducted in a fully turbulent air channel flow. The aims are to both quantify the achievable drag reduction and to assess positive and negative aspects of the present actuator choice, from a practical and energetic standpoint.

The wind tunnel adopted in the present work is first described in Section 4.1. Details about the active test section with integrated DEA follow in Section 4.2. The experimental procedure is presented in Section 4.3, together with the fundamental parameters of the imposed wall oscillation. The validation of the base flow is carried out in Section 4.4. Subsequently, the results concerning drag reduction are presented in Section 4.5, followed by a critical discussion in section 4.6. Finally, the power budget, measured for the first time in the present work, is presented and discussed in Section 4.7.

4.1 Wind tunnel

The following laboratory investigation is conducted in a fully developed turbulent air channel flow, contrary to most previous work on spanwise

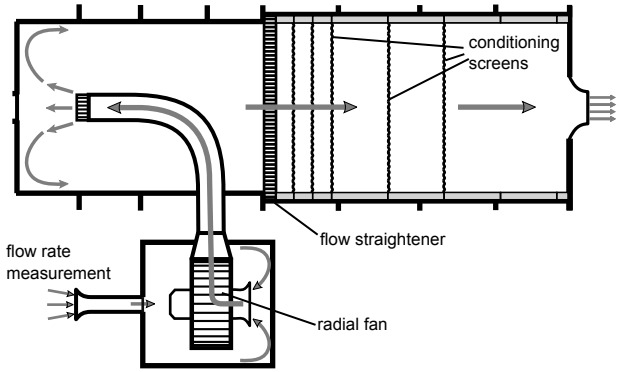

Figure 4.1: Sketch of the working principle of the wind tunnel

wall forcing, where either water is chosen as medium ([8, 34, 136, 163]) or external wall-bounded flows ([31, 32, 41, 58, 136, 163]) were preferred.

The wind tunnel employed in the following laboratory investigation is a high-accuracy, open-circuit, blower tunnel which has been specifically developed by Güttler [59] for accurate measurement of small changes in skin-friction drag. The interested reader can learn about the main advantages of blower tunnels for low-speed wind tunnel testing in Barlow *et al.* [10] and Bradshaw & Metha [22].

A schematic of the wind tunnel is given in Figure 4.1. A centrifugal compressor, controlled by a frequency converter, draws air from the environment through an inlet nozzle against the backside wall of a large settling chamber (1.67 m × 4.8 m). A polycarbonate honeycomb flow straightener and five stainless-steel conditioning screens are located along the path to its outlet, so as to guarantee low turbulence levels and no large-scale swirlimg motion. Interchangeable working sections can be mounted at the outlet of the settling chamber, where the actual experiment takes place. In this work, a flat duct is chosen, to create a quasi-2D channel flow.

The channel instrumentation is schematically depicted in Figure 4.2. At the channel inlet two different, pressure-based, flow-rate measurement devices are alternatively installed, according to the needs: an orifice and a nozzle flow meter. Irrespective of the device chosen, the pressure drop Δp_{fm} it generates is measured with one of two Setra 239D differential pressure transducers, with measurement ranges from 0 to 125 Pa and 625 Pa respectively. The most appropriate measurement range is chosen in order

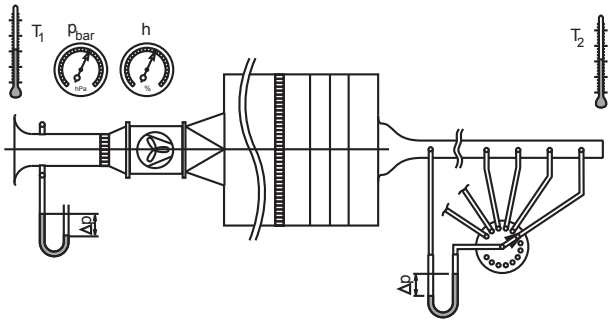

Figure 4.2: Schematic sketch of the measurement equipment

to maximize accuracy, which is ±0.07% of the full-scale for both transducers. The ambient absolute pressure data is supplied by the "Hessisches Landesamt für Umwelt und Geologie" with an accuracy of 1 hPa and is corrected to account for the absolute altitude at which the experimental facility is located. Moreover, two PT100 thermocouples measure the ambient temperature close to the inlet and the outlet of the wind tunnel, while two hygrometers are employed to measure the relative humidity. The ambient parameters are needed for the indirect measurement of the air kinematic viscosity and density, which in turn allow estimation of the Reynolds number Re_b, based on the mean bulk velocity U_b. Finally, two MKS Baratron 698A, heated, high-accuracy, unidirectional differential pressure-transducers, with 133 and 1333 Pa maximum range respectively and an accuracy of 0.12% of the reading, measure the pressure drop along the working section and thus can be used to estimate the skin-friction drag.

Two personal computers control the wind tunnel and the measurement equipment in the working section, through a user interface programmed with LabVIEW. Analog signals are acquired and digitalized by 16 bit DAQ modules.

4.2 Test-section

The wind tunnel test section consists of a flat duct of 12:1 aspect-ratio. Its inner width W and height H are 25.2 mm and 300 mm respectively. It is made up of four independent aluminium plates and extends in the streamwise direction for about 3950 mm, corresponding to $158H$. The test

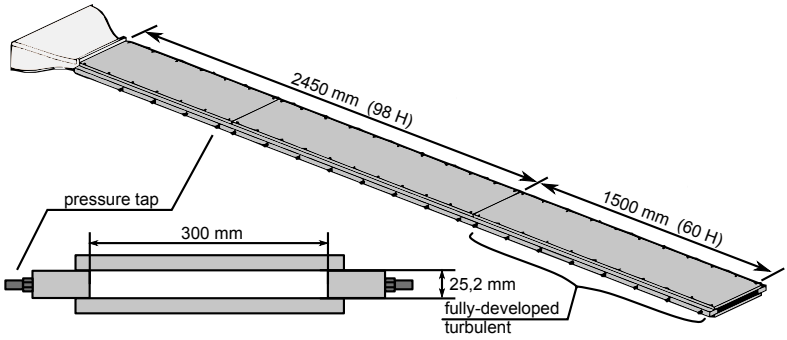

Figure 4.3: Perspective view of the wind-tunnel working section and its cross-sectional view. Dimensions in mm.

section is connected to the settling chamber of the wind tunnel by a glass-fiber nozzle with a contraction ratio of 6:1. Air is driven into the nozzle through an aluminium inlet that extends into the settling chamber. The nozzle ends in a permanent, 40 mm-long portion of test section, ensuring a high quality connection. The glass fiber part fits well into the inlet with less than 0.05 mm play, thanks to a careful filling and polishing of the connection.

The narrow channel height poses stringent requirements on the tolerances of the channel side walls. Its deviations have been kept within 0.02 mm about the nominal value, thanks to the special method with which the side walls are produced. They were cut from the same plate in direction of grain and extend over the entire channel length. Conversely, the plates that constitute the top and bottom walls are divided into sections of 950 mm, 1500 mm and 1500 mm respectively. These sections are screwed to the side walls and thus can be replaced. The smooth plates on top and bottom are made from cast, precision-milled aluminium. Their surface roughness is $Ra = 0.4\ \mu$m.

21 pairs of Ø0.3 mm pressure taps are located along the side walls. This choice eases the exchange of the channel plates. The first pressure tap is at 100 mm after the leading edge of the working section, while the streamwise distance between taps is 200 mm. A distance of 100 mm is left between two pressure taps that are located across the connection between two plates, in order to observe eventual local misalignment that may result in additional

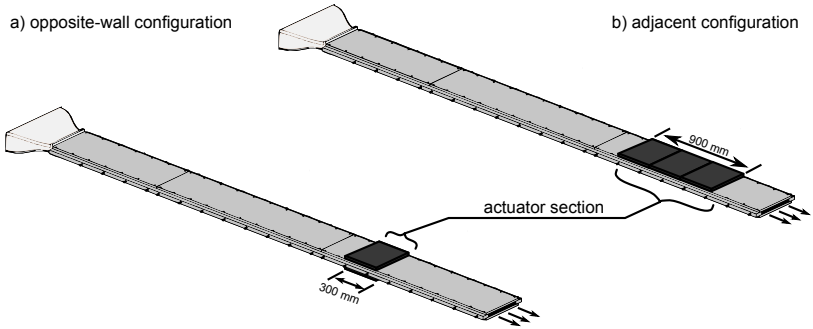

Figure 4.4: Wind tunnel test section equipped with DEA based spanwise oscillating surfaces in two different arrangements: a) two actuators facing each other at the same streamwise position; b) array of three-actuator juxtaposed downstream on one side of the channel only.

pressure losses. After positive testing, taps facing each other at a given streamwise position are connected and their pressure line fed to the pressure transducer. An air tight connection between the pressure line and the pressure tap is ensured by a snap-fit joint between the former, a Ø1.3 mm silicone tube, and a Ø1.5 mm brass tube.

A trip of 13% blockage is installed at the entrance of the channel and provides a fully developed turbulent flow for $Re_b > 4500$ and at least $80H$ beyond the channel entrance. The spanwise oscillating surfaces are installed at least $100H$ downstream of the channel entrance.

4.2.1 Active test section

The DEA based spanwise oscillating surfaces are installed into the wind tunnel in two different arrangements, shown in Figure 4.4, called opposite-wall and adjacent configuration. In the former, two actuators face each other at the same streamwise position. In the latter, three actuators are juxtaposed to form an array that extends downstreams on one side of the channel only.

A detail of the opposite-wall configuration is given in Figure 4.5. Each of the two WT1 DEA actuators is flush-mounted into a slot of a 25 mm thick plexiglass plate (575×350 mm^2), which constitutes the inactive part of the channel wall. A 0.1 mm play between the actuator and the slot edges is

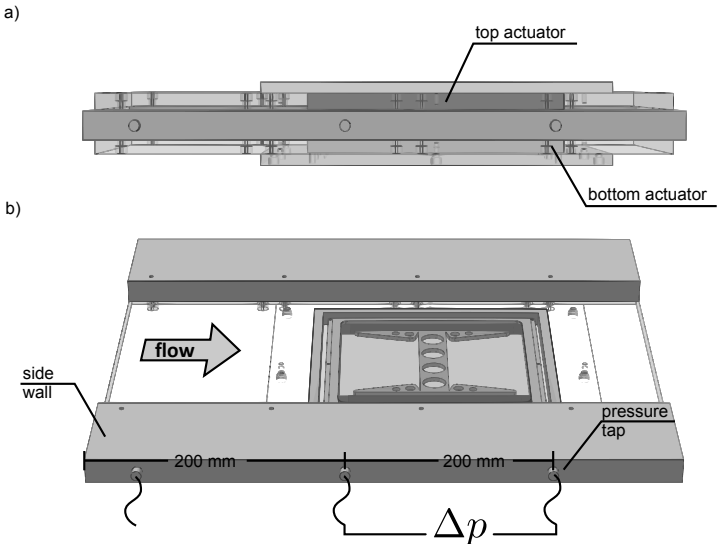

Figure 4.5: Active wind tunnel test section with actuators in opposite-wall configuration. a) Side view; b) Top view cut at the semi-height of the tunnel. Only the bottom is visible.

allowed, so that the static pressure can balance between the two sides of the DEA actuator, in order to avoid inflation or deflation of the membrane. The actuator assemblies are placed at the same streamwise location and their leading edge is located 107H after the channel inlet. The pressure taps are positioned to measure the pressure difference across a 200 mm-long channel slice that starts 10 mm after the leading edge of the actuator stiff plate, i.e. just after the homogeneously moving region.

This arrangement is relatively close to what is usually done in the large database of numerical experiments available in literature, where a spanwise wall velocity is imposed on both walls of a (doubly periodic) turbulent channel flow (see, for example [53, 130, 132, 138, 160]).

The adjacent configuration, on the other hand, does not require additional components other than the three WT2 actuators. Their width (307 mm) is larger than the channel width, so that the actuators themselves represent the complete channel wall. The supporting plate of the actuators is designed to be directly screwed to adapters located on the side

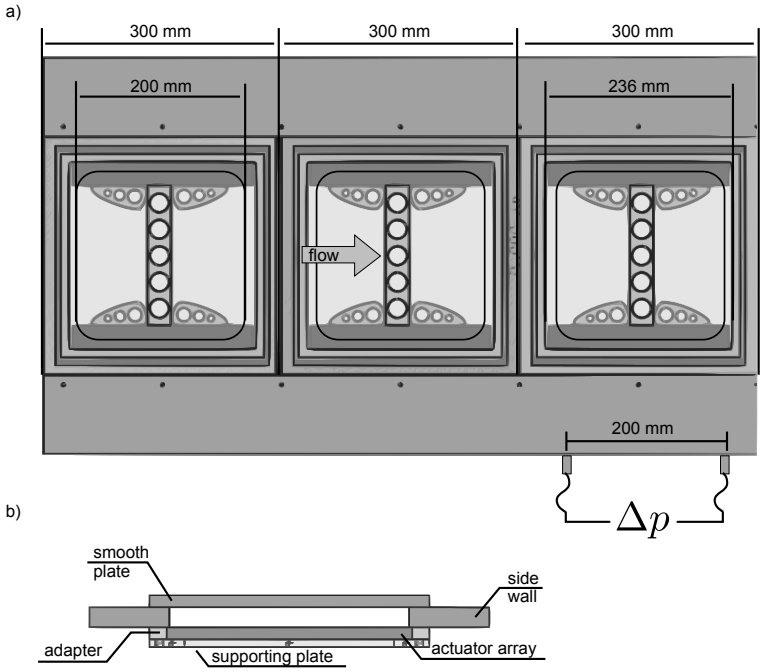

Figure 4.6: Active part of the wind-tunnel test section with actuators in adjacent configuration. a) Top view cut at the semi-heiht of the tunnel. Only the bottom wall is visible; b) Front view. Dimensions in mm.

walls of the channel. Figure 4.6 sketches the experimental setup for the second arrangement. Compared to the opposite-wall case, the streamwise extent of the controlled region is larger, at the expense of the symmetry about the channel mid-plane. Moreover, the location of the pressure taps is similar to the opposite-wall case and only the pressure difference across the homogeneously-moving region of the downstream actuator is measured. This reduces effects of eventual streamwise spatial transients, where the effect of the control may vary downstream.

The active section contains many features that are not present in a normal smooth, plane wall, like small gaps or unevenness at the wall/actuator interfaces and the actuator itself with its compliance. The actuator can then become perceptible as a roughness leading to an higher skin-friction

opposite-wall configuration							
		A [mm/s] 820				A [mm/s] 820	
Re_b	T^+	A^+	L_A^+	Re_b	T^+	A^+	L_A^+
4520	33	4.6	2404	5900	53	2.8	3050
5870	53	3.6	3034	6740	68	2.5	3419
6680	67	3.2	3427	7580	83	2.2	3817
8380	100	2.6	4170	9250	118	1.8	4546
10040	137	2.2	4881	10930	158	1.6	5256
11700	179	2.0	5582	12610	203	1.4	5961
13340	226	1.7	6257	14290	252	1.2	6641
				15140	279	1.2	6992

Table 4.1: Parameters of wall oscillation at each wind tunnel bulk Reynolds number Re_b for actuation in opposite-wall configuration. T^+ and A^+ are the nondimensional period and amplitude of wall oscillation. L_A^+ is the streamwise length of the actuator homogeneously moving region.

compared to a smooth wall, posing an additional technological problem especially for high Reynolds number applications. In order to monitor this effect, the pressure drop Δp_{ref} across a reference section of identical streamwise length, but located upstream, has been constantly measured with one of the two available MKS Baratron pressure transducers.

4.3 Experimental procedure and parameters

The measurement procedure consists of six measurement sessions, each three minutes long, during which the pressure drop across the actuator and the reference sections are simultaneously acquired with the two independent pressure transducers, alternating activation and deactivation of the actuators. The pressure drop across the flow meter is measured by using the pressure transducer with the most appropriate measurement range, in order to minimize uncertainty. Temperature at the inlet and outlet of the wind tunnel, as well as humidity and absolute pressure are measured at the beginning and end of the measurement procedure to correct the value

adjacent configuration					
		A [mm/s]			
		280	420	560	
Re_b	T^+		A^+		L_A^+
3960	37	1.8	2.7	3.5	2404
4370	44	1.6	2.5	3.3	3034
5000	48		2.3		3427
5400	55	1.5	2.2	2.9	4170

Table 4.2: Parameters of wall oscillation at each wind tunnel bulk Reynolds number Re_b for actuation in adjacent configuration. T^+ and A^+ are the nondimensional period and amplitude of wall oscillation. L_A^+ is the streamwise length of the actuator homogeneously moving region.

of air density and viscosity. The skin friction can be computed as:

$$C_f = \frac{WH^3}{\rho L_{\text{tap}} Q^2} \Delta p \tag{4.1}$$

where Δp is the pressure drop over the distance L_{tap} between the two consecutive pressure taps, W is the channel width, H the channel height and Q the volumetric flow rate. Henceforth we indicate with C_f the skin-friction in the actuator section and with $C_f^{(r)}$, the skin friction in the reference smooth section. In both cases, the additional subscript 0 refers to the unactuated case. The drag reduction rate reads then

$$R = 1 - \frac{C_f}{C_{f,0}} \tag{4.2}$$

and is evaluated for several wind tunnel flow rates.

In order to attain the maximum amplitude and efficiency of wall oscillation, the actuators have been driven at their resonance frequency, 65 Hz and 45 Hz for WT1 and WT2 respectively. During the test in opposite-wall configuration, the actuation voltage has been kept close to the breakdown voltage of the DEA membrane, i.e. $\phi = 4000$ V, which yields a maximum amplitude of wall oscillation of $A = 820$ mm/s. Inversely, measurements at three different driving voltages, $\phi = 2000$, 2200 and 2500 V, have been carried out with the actuators in the adjacent configuration, to verify that

the drag reduction rate is a monotonically increasing function of the oscillation amplitude, thus prooving causality. The amplitude of the resulting wall oscillation at the three driving voltages are 280, 420 and 560 mm/s respectively.

Several tests at different wind tunnel flow rates are conducted. As the Reynolds number changes, the nondimensional amplitude A^+ and period T^+ of wall oscillation, expressed in viscous units, change. We are then able to test different forcing conditions by simply changing the bulk Reynolds number, since the achievable drag reduction depends on the forcing parameters in viscous units. Strictly speaking, the Reynolds number also influences the amount of drag reduction that can be achieved [30, 53, 130], R being lower at higher Re for constant control parameters in viscous units. Therefore R is also influenced by Re during the sweep at different flow rates, which may confuse the scenario. However, the present range of Re, less than a decade of Re_τ, is narrow enough to consider the this influence negligible. A more extensive discussion on the effects of the Reynolds number can be found in Chapter 6.

An overview of the nondimensional control parameters for every measurement can be found in Tables 4.1 and 4.2, for the opposite-wall and adjacent configuration respectively. All quantities have been nondimensionalized by the kinematic viscosity ν and friction velocity $u_\tau^{(r)}$ in the smooth section.

4.4 Base flow validation

Figure 4.7 shows the skin friction coefficient $C_{f,0}$ (empty symbols), measured across the inactive actuator section compared to $C_{f,0}^{(r)}$ (filled symbols), the one measured across a section of the same length located just upstream the actuator section, and to the Dean's correlation [39] (solid line).

The good agreement between the Dean's correlation and the skin friction over the reference section confirms the flow to be a fully-developed turbulent channel flow, at least $80H$ after the tripping located at the upstream part of the measurement section, where the measurement takes place. The skin friction coefficient over the actuator section agrees well with the one of the reference flow up to $Re_b \approx 8000$, where the unevenesses introduced by the actuators start to act as a roughness element, resulting in a higher friction than over the reference section. The fine adjustment of the actuator section is crucial, as small unevenness lead to visible changes in the skin friction. This can be appreciated by comparing the two measurement series in Figure 4.7, represented by circles and diamonds, acquired before

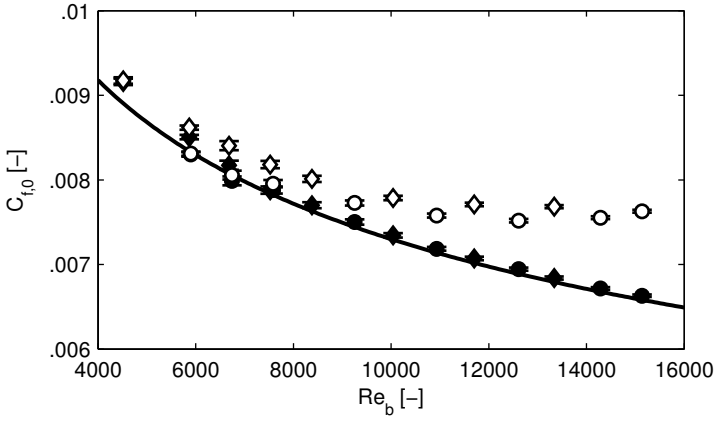

Figure 4.7: Skin-friction coefficient against the bulk Reynolds number Re_b. Empty symbols: $C_{f,0}$ at the inactive actuator section; filled symbols: $C_{f,0}^{(r)}$ at the reference section. Circles and diamonds refer to different measurements series, after having reassembled the actuator section. The error bar is not shown if smaller than the symbol size and represent the error at 90% confidence interval.

and after having reassembled the actuator section. Probably due to an irregularity introduced during reassembling, one data series shows a higher friction over the inactive actuator section than the other. On the other hand, the friction over the reference section does not change, confirming that the small differences between the two measurement series are due to the actuators themselves, rather than to any other source of random error, as zero-point drift of the pressure sensors.

The effect of the electromagnetic field generated by the high-voltage power supply across actuators and high-voltage cables on the pressure transducers has been tested. The skin-friction over the reference section is used as an indicator, as it should not change upon actuator activation. The results are reported in Figure 4.8, where the percent change in skin friction measured at reference section before and after actuator activation is shown. After actuator activation, the change in skin-friction is always smaller than 0.5% and is always within the measurement uncertainty. Moreover, the

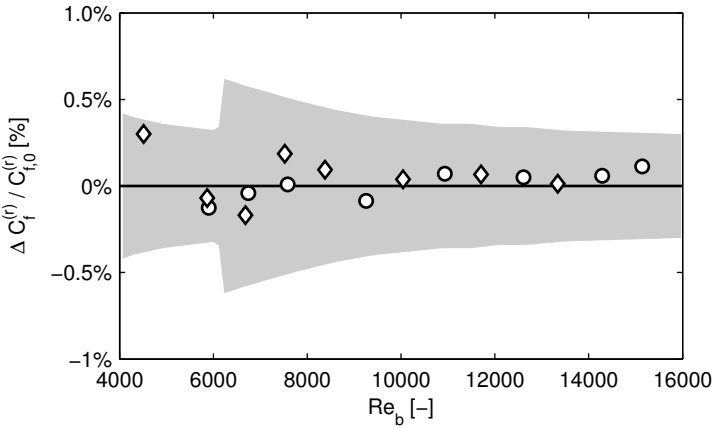

Figure 4.8: Percent change $\Delta C_f^{(r)}/C_{f,0}^{(r)}$ of the skin-friction over the reference section before and after actuator activation. The shaded area represent the confidence interval at 90% confidence level.

data scatter is mostly confined to the very low Re_b-range, basically due to temporal fluctuations of flow rate.

Figure 4.8 also indicates the accuracy with which a close-to-zero variation of skin friction can be determined and reproduced, which gives us confidence of being able to detect up to the smallest amount of actively induced drag reduction.

4.5 Drag reduction

Figure 4.9 reports the experimental results, plotted as drag reduction ratio 100R against the Reynolds number Re_b, for actuators in the opposite-wall configuration. The nondimensional amplitude A^+ and period T^+ of wall oscillation, nondimensionalized by the kinematic viscosity and the friction velocity in the reference section, is reported for each measurement. As A and T are constant in dimensional units, it is important to note that T^+ rapidly increases from left to right, i.e. for increasing Reynolds number, due to the increment of the viscous time u_τ^2/ν. The raising u_τ with Re acts on $A^+ = A/u_\tau$ in the opposite way, resulting in a lower A^+ at higher Re.

Therefore, at lower Re_b the small friction velocity u_τ yields higher values of the nondimensional amplitude A^+ of wall oscillation than at higher Re_b.

The two measurements series are shown with different symbols. In both cases, the results indeed show the traits that one would expect from DNS. The drag reduction ratio increases for rising Re_b first, as T^+ is approaching the optimal value of T^+, before starting the decay at even higher Re_b, where the nondimensional period gets too large. Similarly, the negative trend of R at higher Re is magnified by the decrease of A^+, which gets too small to achieve significant drag reduction. In fact, the observed optimal period of $T^+ \approx 75$ results from the trade-off between oscillating at a sufficiently high A^+ and getting sufficiently close to the real optimal period $T^+_{\text{opt}} \approx 100$, as measured in Direct Numerical Simulations by Quadrio & Ricco [130].

On the other hand, the rightmost datapoints show a plateau which is an unexpected feature, deemed to be an artifact and a consequence of the significantly higher friction generated by the actuators acting as roughness elements at high Re_b. However, we decided to retain the datapoints, which indeed show that wall oscillations may yield skin friction drag reduction also in significantly modified flows.

The results of the two actuator series exhibit qualitatively good agree-

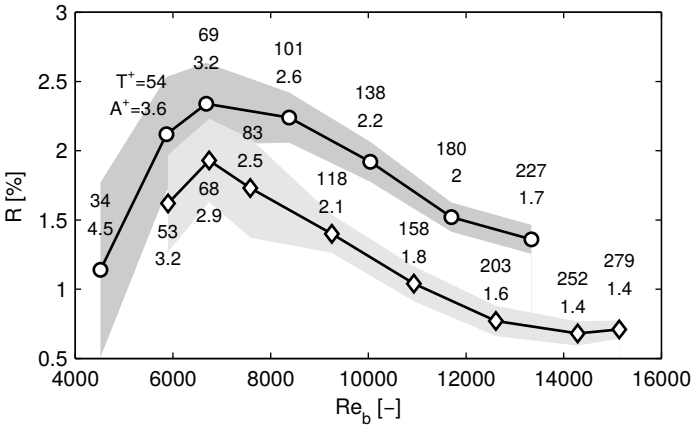

Figure 4.9: Drag reduction $100R$ against the bulk Reynolds number Re_b. The shaded area represents the confidence interval at 90% confidence level. Circles and diamonds refer to different measurement series, conducted before and after having reassembled the actuator section.

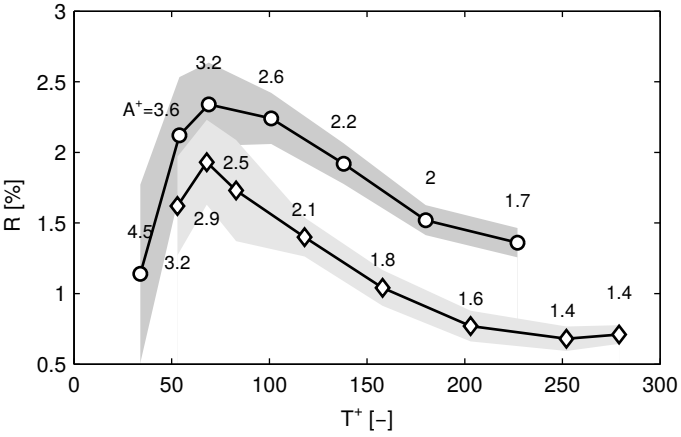

Figure 4.10: Drag reduction $100R$ as a function of the nondimensional period of wall oscillation T^+ for actuators in opposite-wall configuration. Symbols as in figure 4.9.

ment, especially concerning the position of the maximum of drag reduction; although the second batch were less effective. The difference is motivated by the manual process with which the actuators are produced and coupled with the passive flush-mounted top surface, which makes the production of identical actuators very difficult. After re-installing the actuator into the wind tunnel the second series exhibited a slightly lower displacement which yielded a slightly lower drag reduction.

Under the assumption that the change of Re within the present range only marginally affects R in a different way than by simply affecting T^+ and A^+, we are allowed to disregard the Re-dependency and represent the drag reduction as a function of the nondimensional period of wall oscillation. The result is shown in Figure 4.10. The existence of an optimal period is confirmed, which is reasonably constant among the two measurement batches.

Figure 4.11 reports the drag reduction results as function of the nondimensional period of wall oscillations for tests with actuators in adjacent configuration. The three measurement series at diverse A are represented with distinct symbols.

A maximum drag reduction of 4.4% ±0.72 is observed at the highest A^+

and T^+ that have been investigated. A further increase of U_b would have led to even higher T^+, closer to the optimal period T^+_{opt}, thereby yielding to an even higher drag reduction. However, while WT1 actuators withstood the whole measurement campaign without failures, WT2 actuators turned out to be more fragile and underwent frequent failures. This forced us to limit the measurement campaign in the adjacent wall configuration to a few values of U_b (and hence T^+ and A^+).

Nonetheless, important information can be deduced from Figure 4.11. In the adjacent configuration, a longer streamwise portion of the channel is actively controlled by spanwise oscillation, whereas the pressure drop over the most downstream actuator is measured. By doing so, we discard large part of the streamwise spatial transient of drag reduction, where the friction decreases from the uncontrolled value to a steady, lower value. As a result, larger values of drag reduction are obtained for the adjacent configuration with period and amplitude of oscillation comparable to those of the previous opposite-wall case. The achieved drag reduction always increases if T^+ is increased towards the optimal value T^+_{opt}. Moreover, higher amplitude of wall oscillation always resulted in higher R, which

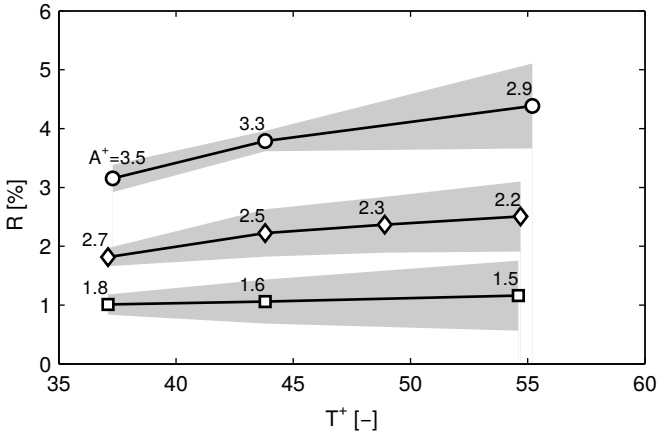

Figure 4.11: Drag reduction $100R$ as function of the nondimensional period of wall oscillation T^+ for actuators in adjacent configuration. Circles: A = 560 mm/s; diamonds: A = 420 mm/s; squares: A = 280 mm/s. The shaded area represents the confidence interval at 90% confidence level.

confirms that the reduction of the skin-friction drag is a consequence of the imposed spanwise wall velocity.

4.6 Discussion

The present data can be compared against the available literature database with the well-established empirical correlation proposed by [130]:

$$R = 1.31S^{+} - 0.027 \tag{4.3}$$

based on the scaling factor S^{+} proposed by [30] and defined as:

$$S^{+} = \frac{a_m^{+}\,\ell^{+}}{A^{+}} = 2\sqrt{\frac{\pi}{T^{+}}}\ln\left(\frac{A^{+}}{A_{th}^{+}}\right)\exp\left(-\overline{y}^{+}\sqrt{\pi/T^{+}}\right) \tag{4.4}$$

where $A_{th}^{+} = 1.2$ is a threshold velocity and $\overline{y}^{+} = 6.3$ a given distance from the wall. The parameter S^{+} is constructed by combining a wall-normal length scale ℓ^{+}, related to the distance at which the wall oscillation affects the turbulent structures, and a local spanwise acceleration a_m^{+} within the Stokes layer. The rationale behind the definition of S is the idea that the spanwise wall motion directly affects only wall turbulence that lies within the Stokes layer, while the spanwise acceleration within it is related to the strength of the spanwise forcing.

Equations 4.3 and 4.4 are evaluated at constant A and T in the Re_b-range at which the experiment has been conducted. No Re-effect is accounted than the change in A^{+} and T^{+} due to the change in friction velocity, estimated by computing C_f with the Dean's correlation [39]. The result is shown as a solid line in Figure 4.12 along with the present experimental data for the opposite-wall configuration.

Neither quantitative nor qualitative agreement is evident. Both the magnitude of drag reduction and the location of the drag reduction maximum do not correspond to the prediction of Equation 4.3. Several arguments are relevant to explain such discrepancies.

A laboratory experiment necessarily differs from the idealized setting of a Direct Numerical Simulation (DNS), the tool that generated the database upon which the empirical correlation of Equation 4.3 has been constructed. Most important is the effect of actuating a limited portion of the wall. In fact, the turbulent friction of the flow influenced by the actuator gradually changes from the unperturbed level of the steady channel flow down to the reduced level induced by the wall forcing. Such transients are absent in

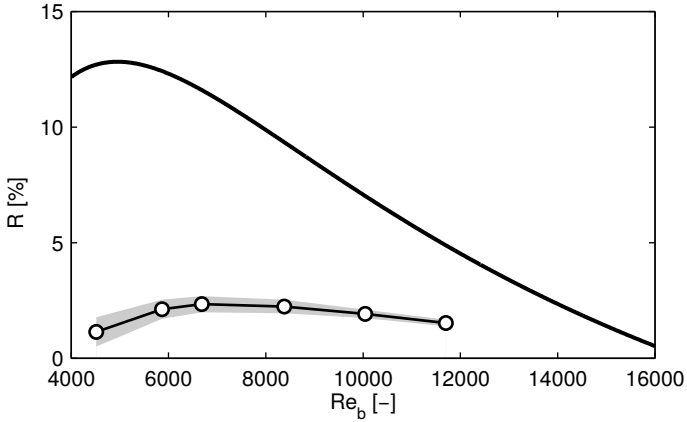

Figure 4.12: Drag reduction ratio R for wall oscillations at $A \approx 820$ m/s and $T = 1/65$ s against the bulk Reynolds number Re_b. Solid line: empirical correlation $131\,S^+ - 2.7$ suggested by Quadrio & Ricco [130]; open circles: present experimental results. The shaded area represents the confidence interval at 90% confidence level.

the indefinite geometry considered in the spatially periodic DNS and has often been used to explain the disagreement observed between DNS results and experimental measurements (see for example [8, 130]). Only a few laboratory [33, 58, 139] and numerical [94, 150] experiments attempted to measure the effect of the finite size actuation surface limiting to the onset spatial transient of drag reduction in the streamwise direction.

First evidence that the streamwise onset transient of drag reduction is largely responsible for the underestimated and skewed experimental data compared to Equation 4.3 is obtained by relating the streamwise onset length to a transient time interval by using the concept of convection velocity of near-wall turbulent skin friction fluctuations ([80, 127]). The DNS by [129] contains information on the temporal long-term transient during which the turbulence friction decreases from the initial value to its minimum value: this transient depends on the control parameters and for $A^+ = 3 - 6$ is about 300-400ν/u_τ^2. Since the convection velocity is about $10u_\tau$ ([127]), the transient length can thus be estimated to be approximately $3500\nu/u_\tau$. The DNS by Gatti & Quadrio [53] show the temporal transient to scale in viscous units at different Re; we assume therefore the

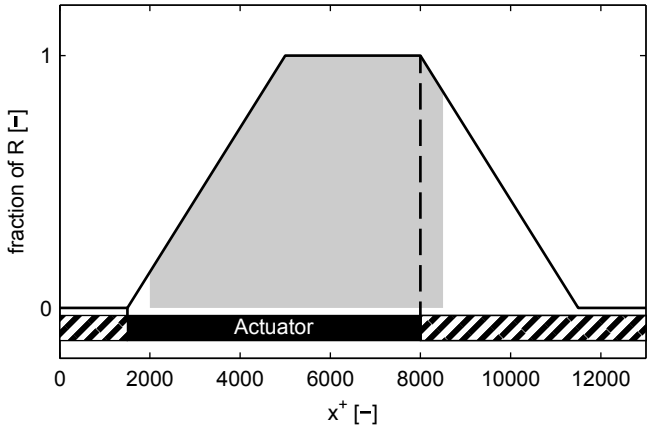

Figure 4.13: Sketch of the streamwise evolution of the synthetic spatial transient of drag reduction. The local fraction of the steady drag reduction is represented as a function of the streamwise coordinate x^+ in wall units. 4.12.

streamwise onset length to be constant in viscous length. The empirical correlation 4.3 can then be qualitatively corrected to account for the onset transient if we additionally assume a linear onset of drag reduction starting from the leading edge of the actuator and compute the integral drag reduction along the 20 cm-long interval, starting 10 mm after the homogeneously actuated region over the actuator. The 10 mm position is the location of the first pressure taps in the experimental setup.

Figure 4.13 schematically shows the artificial spatial transient that has been assumed to correct Equation 4.3. The drag reduction is assumed to increase linearly from 0 at the leading edge of the actuator to the value obtained in a homogeneously controlled channel-flow, as predicted by Equation 4.3, after $3500\nu/u_\tau$. It remains constant until the actuator trailing edge, where it starts to decrease with an identical but opposite transient. The spatially varying drag reduction is integrated over the region between the two pressure taps to yield the integral drag reduction. The sketch of Figure 4.13 represents an actuator whose streamwise extent, in viscous units, exceeds the spatial transient length. This may not be always the case. In fact, the nondimensional streamwise extent of the actuator L_A^+ is

proportional to u_τ/ν, i.e. it can be as small as 2400 viscous lengths at the lowest Re tested, hence, be smaller than the streamwise spatial transient.

Figure 4.14 compares the present experimental data for the opposite-wall configuration with the original and corrected empirical correlations based on S^+, represented by a solid and dashed line respectively. Despite the difference in magnitude of drag reduction, the experimental data and the corrected empirical correlation now qualitatively agree, especially as regards the position of the drag reduction maximum, shifted towards higher Re_b. A further qualitative correction can be applied by multiplying the predicted drag reduction by 2/3, which is the ratio between the actuator and channel width, and yields the dotted curve of Figure 4.12, which is remarkably close to the experimental data.

The residual discrepancy can not be readily explained and is a common feature of experiments aimed at measuring drag reduction capabilities of wall oscillations (as reported by Ricco & Quadrio [138] and in later studies [8, 58]). The present qualitative analysis is based on a rather naive estimation of the streamwise transient and is intended for validation and understainding of the present results. Moreover, the flow over a finite size

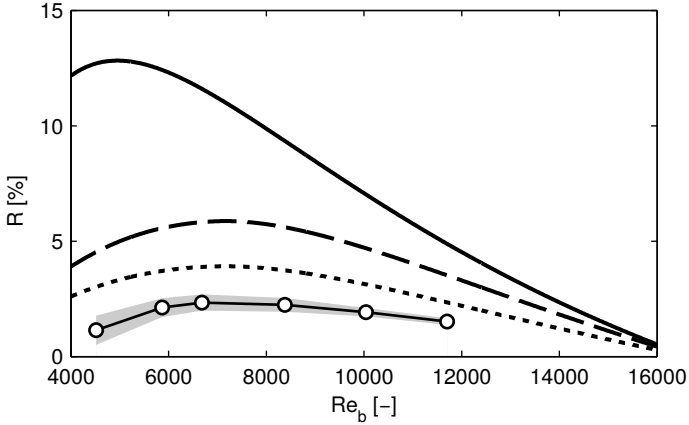

Figure 4.14: Drag reduction ratio R for wall oscillations at $A \approx 820$ m/s and $T = 1/65$ s against the bulk Reynolds number Re_b. Dashed line: modified empirical correlation to account for spatial transient; dotted line: modified empirical correlation to account for both spatial transient and % actuated area. Other symbols as in figure 4.12.

actuator may be more complex than the flow above an unlimited actuator, the usual setting of DNS. In particular, the finite, relative narrow spanwise extent of the actuator may also play a role, which has been disregarded here. An analysis of the effects of finite size actuation on the achievable drag reduction is presented in Chapter 5, where DNS are used.

4.7 Power Budget

Besides the system integrability, a reason for choosing actuators based on DEAs is the promisingly low power consumption. In fact, the net power saving S, per unit pumping power is the decisive figure of merit to evaluate the efficiency of an active control technique aimed at turbulent drag reduction.

In spite of the importance of energetic figures of merit, no direct measurement of the power spent to apply the control is available in the literature, where only few indirect estimations can be found for laboratory experiments. On the other hand, in numerical experiments the power expended to apply the control only accounts for power losses due to the generated spanwise wall shear, thus disregarding any mechanical and electrical losses. In the present work, the net power budget is experimentally measured for the first time.

The control performance is evaluated according to the notation introduced by Kasagi *et al.*[75], in terms of three dimensionless indicators (R, S, G). For the sake of clarity, we recall their definitions here. From an energetic standpoint, the imposition of the control results in a change of the power P needed to pump the flow across the channel, henceforth pumping power,

			WT1	WT2		
f	[Hz]		65	45	45	45
Φ	[V]		4000	2000	2200	2500
A	[mm/s]		820	280	420	560
P_{in}	[mW]	per actuator	1200	36	46	64
		total	2400	108	138	192

Table 4.3: Input power P_{in} at given values of the maximum actuation voltage Φ for WT1 and WT2 actuators.

defined as:

$$P = Q\,\Delta p \tag{4.5}$$

If P_0 and P are the pumping power of the unmanipulated and controlled flow respectively, the drag reduction rate can be conveniently defined as:

$$R = \frac{P_0 - P}{P_0} \tag{4.6}$$

which is the relative change in pumping power. This definition is completely consistent and equivalent to that of Equation 4.2, provided the flow rate is kept constant throughout the experiment.

The power needed to apply the control, or input power P_{in}, is the real active electric power after the HV-amplifiers, which has been defined and measured in Chapter 3 for both WT1 and WT2 actuator series.

The budget between the normalized power saving and expenditure results in the net power saving rate S:

$$S = R - \frac{P_{\text{in}}}{P_0} \tag{4.7}$$

A positive S means that power has been saved by applying the control, whereas $S < 0$ indicates that the energy expenditure is larger than the obtained saving.

The gain G is the power saved per unit control input power and is a measure of the overall efficiency of the control strategy, combination of the electromechanical conversion efficiency, the fluid mechanic efficiency and the control efficiency. It is defined as:

$$G = \frac{P_0 - P}{P_{\text{in}}} \tag{4.8}$$

At this stage, all the dimensional quantities needed to compute S and G are at hand. Table 4.3 summarizes the input power requirements of both WT1 and WT2 actuator models at each relevant working condition. In the range of very low Re that we investigated, the power P_0 required to drive the flow was 13 mW and 400 mW at the lowest and highest Re respectively, which is a relatively small amount, compared to P_{in}. The power saved $(P_0 - P)$, equal to $R\,P_0$, is only few percent of the pumping power P_0, which results in net savings between 0.2 and 3.9mW. This tiny amount of energy describes well the challenge of achieving a positive net power saving via active flow control at low Re.

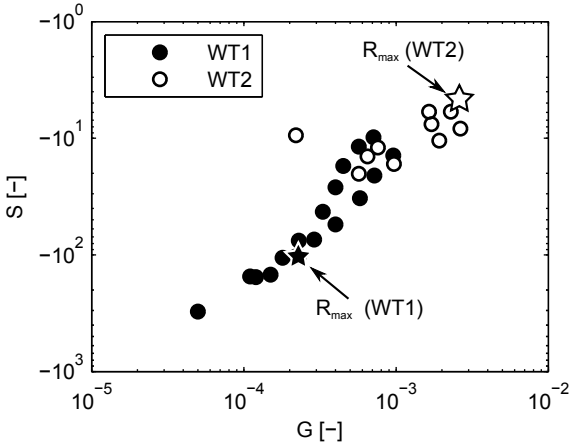

Figure 4.15: Experimentally measured map of net power saving rate S against control gain G. Filled circles: measurements with WT1 actuators in opposite-wall configuration; empty circles: measurements with WT2 actuators in adjacent configuration. A star marks the point for which maximum drag reduction R is achieved.

An overview of the global energetic performance of the control is given by the (S, G) map of Figure 4.15. All the datapoints lie in the quadrant $S < 0$, which means that no net energy saving has been achieved. The measurements made with WT1 actuators have both smaller S and G due to a combination of higher input power and lower drag reduction rate than WT2 actuators. The value of U_b; hence T^+ and A^+, at which the maximum drag reduction is achieved does not coincide with either the value for maximum S, or the one of maximum G, as might be expected whenever the control parameter are kept constant in dimensional units. This is because R is relatively small compared to the second term of Equation 4.7 and relative insensitive to a change of Re_b. When Re_b is increased beyond values that lead to $T^+ > T^+_{opt}$, R decreases and rapidly vanishes. The same occurs for the term P_{in}/P_0, which is negative in the present case and approaches zero very fast with Re. This can be easily explained for constant P_{in} by rearranging Equation 4.7, assuming $R \approx$ const. and developing P_0

as follows:

$$S = R - \frac{P_{\text{in}}}{\rho\, L_{\text{tap}}\, W\, U_b^3\, C_{f,0}} \tag{4.9}$$

Additionally highlighting Re_b and estimating $C_{f,0}$ with the Dean's correlation ([39]) yields:

$$S = R - 13.7 \frac{P_{\text{in}}}{\rho\, L_{\text{tap}}\, W} \left(\frac{H}{\nu}\right)^3 Re_b^{-11/4} \tag{4.10}$$

It is now evident that, for constant actuation parameters in dimensional units, i.e. for constant P_{in}, the change in S with Re_b is mainly due to the rapid increase of P_0 with Re_b. However, S would not become positive if Re were increased further, because the nondimensional control parameters T^+ and A^+ at higher Re are too far from the optimal ones and are not expected to lead to drag reduction.

The measurement series with WT2 actuators has been limited to a range of low values of Re_b that deliver nondimensional periods of oscillation closer to, but indeed slightly smaller than, the optimal $T^+_{\text{opt}} = 75$. As a consequence, the highest value of Re_b tested, where the ratio P_{in}/P_0 is lowest, is also the one that delivers the best drag reduction. Therefore, maximum R, S and G occur for the same forcing condition. Most interestingly, the WT2 actuators, thanks to their improved design, required very low active power which resulted in an interestingly high, yet still negative, maximum S of -4.63. The corresponding maximum G is $G = 0.003$, which means 0.3% global efficiency.

The still negative S represents a significant step forward towards $S = 0$ enabled by DEAs, which is indeed attractive if compared to $S = -10^5$ and $G = 10^{-5}$ of other proof-of-principle experiments (see for example [8]). A critical step towards a positive S is the achievement of sizable drag reduction, higher than the few percent achieved here, which is indeed attainable also by passive means. Moreover, higher Re could ease the conquest of $S > 0$, since the power saved, expressed in mW, rapidly increases with Re. On the other hand, it poses other technological problems, not least of which is the drastic decrease of the timescales of actuation, which, beside being a challenge for any conceivable device, also raises its power requirement.

5 Influence of inhomogeneous actuation on control performance

Spanwise wall oscillations are mostly tested in numerical experiments, where they are implemented as a periodic, spanwise wall velocity imposed on an indefinitely large wall. While useful to study the effect of a homogeneous spanwise Stokes layer on near-wall turbulence in a very defined and controlled framework, this idealization can not be emulated in a laboratory experiment, where only a portion of the wall is displaced. Among the most important consequences of leaving the idealized setting of a DNS is the presence of a spatial transient at the beginning of the active section, where the turbulent friction gradually decreases from the unperturbed level of the steady smooth channel down to the reduced level induced by the wall forcing. This spatial transient has been invoked in Chapter 4.6 and in some other experimental investigations (see, for example, [8, 58]) to explain the discrepancy between the lower drag reduction usually observed in laboratory experiments and DNS results.

Few attempt have been made with different success, to experimentally measure the development length of the wall shear stress after the leading edge of a spanwise oscillating surface ([33, 58, 139]). They all agree on the existence of such spatial transient, while none provides the possibility to verify to which extent it is responsible for the discrepancies. A peculiar aspect of the experimental investigation presented in Chapter 4 is the combination of the low Re (Re_τ is in the range 150-450), the relative small actuated area, and the channel geometry, which enables us to numerically represent, to some extent, the experimental conditions. In the present Chapter we use DNS of a fully-developed turbulent channel flow to study the effect of inhomogeneous actuation on control performance and directly compare to the experimental results of Chapter 4, to investigate whether inhomogeneous actuation alone explains the discrepancies between numerical and laboratory experiments.

As a real actuator is always localized and finite in size, the assessment of the effects of inhomogeneous actuation raises interest also for other practical, more general reasons, besides the direct comparison of numerical and

laboratory experiment. The question whether the local amount of achievable drag reduction, beyond spatial transients, is equal for inhomogeneous and homogeneous actuation has not been answered yet. Moreover, no information on the spatial transient at the rearmost edge of the actuation region is available, where the turbulent friction recovers from the drag-reduced level to the value of the smooth channel.

The structure of the present Chapter is as follows. In Section 5.1 the numerical method and the computing system used to run the present simulations is first described. Then, we present the numerical strategy adopted to numerically mimic an actuator of finite-size, followed by a detailed description of the numerical procedure, along with the main discretization and control parameters. Section 5.2 describes the main results in terms of the streamwise and spanwise development of the longitudinal wall shear stress about an actuator of finite size. In the same section, the results are also commented in detail. Finally, Section 5.3 describes the spatial development of the phase-averaged spanwise velocity and shear induced by the wall oscillations.

5.1 Problem definition

5.1.1 Numerical method and computing system

Direct Numerical Simulation of turbulent flows in doubly periodic channels is used to study the drag reducing properties of spatially inhomogeneous spanwise wall oscillations. Two sets of simulations have been run with the DNS code developed by Luchini & Quadrio [102], and adapted to allow the imposition of inhomogeneous spanwise wall velocity. The code is a mixed-discretization parallel solver of the incompressible Navier-Stokes equations, based on Fourier expansions in the homogeneous directions and high-order explicit compact finite-difference schemes in the wall-normal direction. If exception is made for the particular boundary conditions at the channel walls, discussed below, the present set of calculations is relative standard. The nonlinear terms of the equations are evaluated in a pseudo-spectral way, and the related aliasing error [24] (in the homogeneous directions) is exactly removed by expanding the number of Fourier modes by a factor of at least 3/2 before transferring from Fourier space into physical space. Time integration of the equations is performed with the classical partially implicit approach [81], in this case using a third-order low-storage Runge-Kutta method for the convective terms, and a second-order Crank-Nicolson

scheme for the viscous terms.

The numerical simulations described in this paper have been performed on the Lichtenberg High-Performance Computer (LHPC) of the Technische Universität Darmstadt, made by 706 computing nodes, each endowed with 2x 8-cores 2.6GHz Intel© Xeon© Processor E5-2670. The computing nodes are connected together with both a FDR-10 Infiniband and a 10GBit-Ethernet links. Each computation run on a smaller island of the cluster, composed by 2 E5-2670 processors, for a total of 32 cores.

5.1.2 Modeling the finite-size actuation

From a numerical perspective, the homogeneous spanwise wall oscillation translates into imposing the following boundary condition for the spanwise wall velocity w_w:

$$w_w(t) = A \sin\left(2\pi \frac{t}{T}\right) \tag{5.1}$$

where A and $T = 2\pi/\omega$ are the well-known amplitude and period of wall oscillation, t is the time and ω is the angular frequency.

Equation 5.1 can be extended to represent inhomogeneous wall oscillations through a profile function Ψ, that serves as a filter to select the domain where the oscillation takes place. The form of the boundary condition is:

$$w_w(t) = A\,\Psi(x,z) \sin\left(2\pi \frac{t}{T}\right) \tag{5.2}$$

where Ψ is function of x and z, the streamwise and the spanwise coordinate respectively.

In order to separately address the effect of limiting the streamwise and spanwise extent of the controlled region, two independent simulations are run, named limited-length (LL) and limited-width (LW) actuation. In the former case, the function Ψ is $\Psi_{LL}(x)$, function of the streamwise coordinate x only. In the latter, the oscillation amplitude modulation occurs in the spanwise direction z only, hence $\Psi = \Psi_{LW}(z)$.

Both $\Psi_{LL}(x)$ and $\Psi_{LW}(z)$ are based on a continuous step function $f(\hat{x})$, of the generic variable $\hat{x}$, that linearly rises from zero for negative $\hat{x}$ to unity for $\hat{x} > 1$. The expression of $f(\hat{x})$ is

$$f(x) = \begin{cases} 0 & \hat{x} < 1 \\ \hat{x} & 0 \le \hat{x} \le 1 \\ 1 & \hat{x} > 1 \end{cases} \tag{5.3}$$

Re_b [−]	U_b m/s	Re_τ [−]	ν [m^2/s]	ρ [kg/m^3]	A^+ [−]	T^+ [−]	L_A^+ [−]	Δ_{ramp}^+ [−]
5870	3.51	190	1.494×10^{-5}	1.203	3.6	53	3034	303

Table 5.1: Summary of the flow and oscillation parameters of the particular laboratory experiment case of Chapter 4 which is taken as model for the present DNS investigation. Δ_{ramp}^+ is the distance between the edges of the homogeneously moving and fixed part of the actuator (see Figure 5.1).

Finally, the profile function $\Psi_{LL}(x)$ takes the form:

$$\Psi_{LL}(x) = f\left(\frac{x - x_{\text{start}}}{\Delta_{\text{ramp}}}\right) - f\left(\frac{x - x_{\text{end}}}{\Delta_{\text{ramp}}}\right) \tag{5.4}$$

Here x_{start} and x_{end} denote the streamwise extent of the region where a non-zero spanwise wall velocity is imposed. Δ_{ramp} is the rise (or fall) distance of the profile function.

The spanwise profile function, which modulates the spanwise oscillation amplitude along the spanwise direction, takes the slightly more complicated form:

$$\Psi_{LW}(z) = f\left(\frac{z - z_{\text{start}}}{\Delta z_{\text{ramp}}(t)}\right) - f\left(\frac{z - z_{\text{end}}}{\Delta z_{\text{ramp}}(t)}\right) \tag{5.5}$$

where $\Delta z_{\text{ramp}}(t)$ is now function of time and reads:

$$\Delta z_{\text{ramp}}(t) = \Delta_{\text{ramp}} - \frac{A}{\omega}\sin(\omega t) \tag{5.6}$$

here Δ_{ramp} is the average rise (or fall) distance at the oscillation phase of $\pi/2$. Since $\Delta z_{\text{ramp}}(t)$ must be positive for every t, the following congruence condition for Δ_{ramp} must be veryfied:

$$\Delta_{\text{ramp}} > \frac{A}{\omega} \tag{5.7}$$

Both $\Psi_{LL}(x)$ and $\Psi_{LW}(z)$ have been defined so as to reproduce the streamwise or spanwise extent, in wall units, of a WT1 actuator during one particular laboratory experiment described in Chapter 3, whose main flow, size and actuation parameters are summarized in Table 5.1. A sketch of the actuator with its size in dimensional and viscous units is reported in

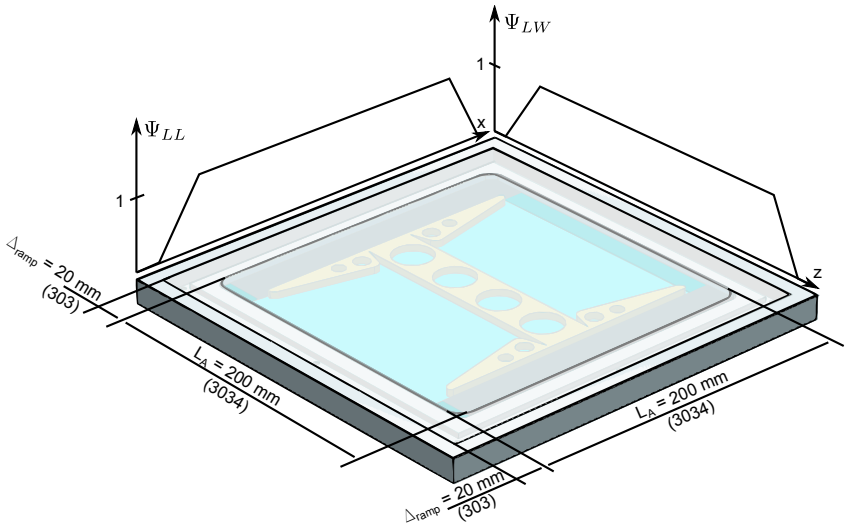

Figure 5.1: Schematic of a WT1 actuator with its size in dimensional and viscous units. The development of the functions $\Psi_{LL}(x)$ and $\Psi_{LW}(z)$ along the actuator surface is also shown.

Figure 5.1, together with a sketch of the functions $\Psi_{LW}(x)$ and $\Psi_{LW}(z)$. The imposed amplitude of wall oscillation is constant and maximum over the stiff plate at the center of the actuator, that oscillates rigidly in plane; linearly decreasing when moving from the edge of the stiff plate towards the edge of the actuator; is zero elsewhere.

5.1.3 Discretization and computational procedures

The need to represent spatial transients and accommodate the actuated region poses strict requirements on the size of the computational domain, in order to avoid non-physical effects of the periodic boundary conditions. Therefore, the domain size along the direction where the imposed spanwise wall velocity is inhomogeneous is largely extended with respect to common DNS. The streamwise (x) length of the computational domain is $L_x = 76.8\,h$ for the LL case, while the spanwise (z) width is $L_z = 28.4\,h$ for the LW case. The size along the homogeneous directions is chosen following Kim, Moser & Moin [82] to be $L_x = 4\pi$ in the LW case and $L_z = 2\pi$ in the LL case. The

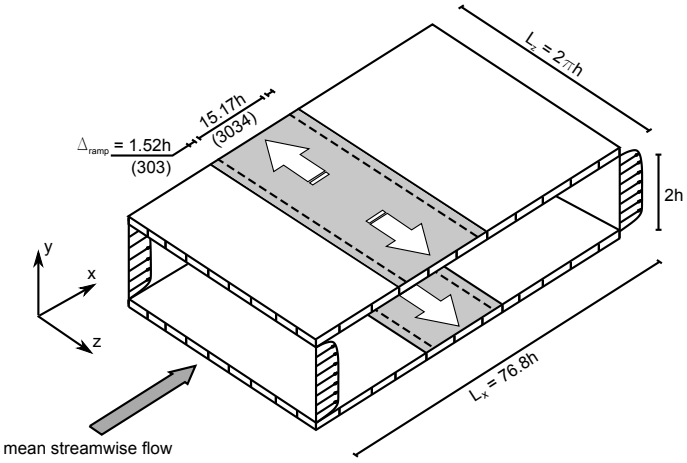

Figure 5.2: Sketch of the computational domain adopted for the limited-length (LL) simulation: the actuated region is evidenced in gray.

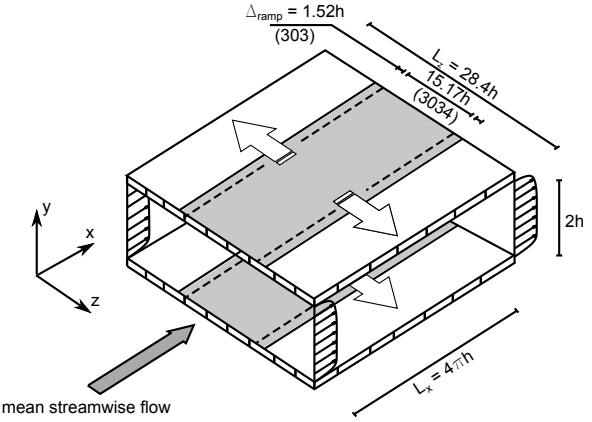

Figure 5.3: Sketch of the computational domain adopted for the limited-width (LW) simulation: the actuated region is evidenced in gray.

Case	L_x	L_z	L_x^+	L_z^+	Δx^+	Δz^+	Δ^+_{ramp}	L_A^+
LL	$76.8\,h$	$2\pi\,h$	15360	1257	10	5	303	3034
LW	$4\pi\,h$	$28.4\,h$	2513	5680	10	5	303	3034

T	T^+	A	A^+
$6.45\,h/U_P$	54	$0.151\,U_P$	3.6

Table 5.2: Computational domain size, spatial resolution and parameters of wall oscillation for the 2 simulations carried out at the same value of $Re_P = 4760$.

number of Fourier modes in the wall-parallel directions is changed so as to to keep a constant resolution of $\Delta x^+ = 10$ and $\Delta z^+ = 5$ (nondimensionalization in + inner units is performed with the friction velocity of the uncontrolled flow and the kinematic viscosity ν of the fluid). 1537 and 257 Fourier modes (before de-aliasing) are used in the LL case to discretize the x- and the z-direction respectively. In the LW case 257 modes are used in the x-direction, while 1137 modes discretize the z-direction. The number of collocation points in the wall-normal (y) direction is 129 and is equal for both simulations. The wall normal resolution is $y^+ = 0.8 - 5.4$.

The spanwise wall velocity is imposed via the boundary condition of Equation 5.2. The period T and amplitude A of wall oscillation are $6.45\,h/U_P$ and $0.151\,U_P$ respectively. U_P is defined as the centerline velocity of a laminar Poiseuille flow with the same flow rate as the present one. They are chosen to result in the same nondimensional control parameters, in viscous unit, investigated in the comparison experiment and recalled in Table 5.2. A summary of the main simulation parameters is given in Table 5.2, together with the parameters that define the wall oscillation and the profile functions Ψ_{LL} and Ψ_{LW}. Figures 5.2 and 5.3 present a sketch of the computational box and its controlled region. Figure 5.4 shows the profile functions that modulate the actuation amplitude along the walls for the LL and LW cases. The boundary condition 5.2 needs to be transformed into Fourier space for use in the pseudo-spectral computation. However, its Fourier expansion converges exactly only point-wise and not globally, which yields a Fourier representation of the original function containing a spurious ripple. This phenomenon, known as Gibbs phenomenon, results from the attempt to represent the continuous, periodic, yet non-differentiable function 5.3 of class $\mathcal{C}^0$ through a series of more regular, indefinitely differ-

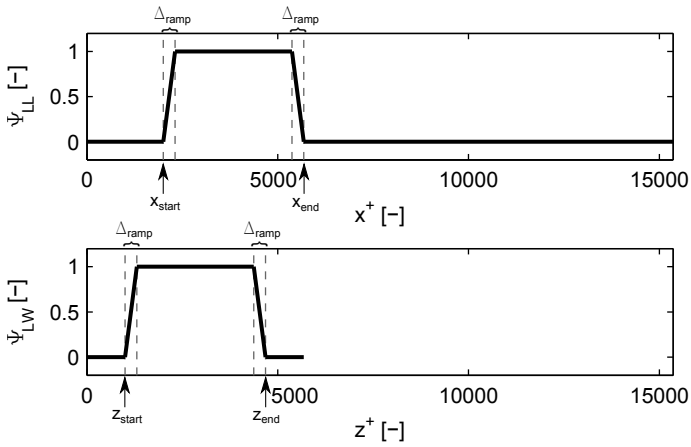

Figure 5.4: Profile functions $\Psi_{LL}(x)$ and $\Psi_{LW}(z)$ used in the LL and LW simulations.

entiable harmonics of subspace $\mathcal{C}^\infty$. The intensity of the ripple has been controlled for every case to be always less than $0.003\,A$ and is deemed to be negligible.

The total integration time is $t_{\mathrm{tot}} = 1500\,h/U_P$. This time interval corresponds in viscous units to $t^+ = 12500$. The integration time is doubled for the LW case because statistics have been averaged in the streamwise direction only, where their convergence requires longer time. The statistical sample is further increased by a factor of two by ensemble-averaging over both walls. The time step used in the computation is adapted to keep a constant CFL [37] number of 0.8.

The equations of motion are integrated in time, starting from the same unperturbed flow field as the initial condition. A constant longitudinal flow rate (CFR) is kept constant and equal to $4/3\ h\,U_P$ during the simulations, allowing the space-averaged longitudinal friction to fluctuate in time around its time-mean value. A null instantaneous spanwise pressure gradient is imposed. An additional duplicate of the LL simulation is run while keeping a constant unity pressure gradient, in order to investigate eventual differences between the two simulation approaches, usually considered equivalent for the simulation of unperturbed channel flows.

For each case, the mean wall shear stress, averaged over both walls and in

time, is computed. Additionally, the spatial evolution of the wall shear and of the integral of the local velocity profile are computed by averaging in time and along the available homogeneous direction, which is the x-direction in the LW case and z-direction in the LL case. A phase-averaging procedure is adopted to selectively average the streamwise and spanwise velocity at 12 phases of oscillation, in order to measure the properties of the Stokes profile and the induced periodic streamwise velocity fluctuations. Unless otherwise indicated, quantities reported hereinafter are scaled by h and U_P.

5.2 Wall shear

In this section, the focus is placed on the local and integral variations of the streamwise wall shear stress τ_x due to the imposition of spanwise wall oscillations. The wall shear stress is chosen as the main parameter instead of the more common skin-friction, as the former is directly related to the experimentally measured quantity, the pressure drop across a channel section, as follows:

$$-\frac{\mathrm{d}p}{\mathrm{d}x} = \frac{\tau_x}{h} \tag{5.8}$$

where the streamwise wall shear reads:

$$\tau_x = \rho\nu \left.\frac{\mathrm{d}\langle u\rangle}{\mathrm{d}y}\right|_{y=0} \tag{5.9}$$

where ρ is the density of the fluid and ν the kinematic viscosity. $\langle\cdot\rangle$ is the short-form for the averaging operator $\langle\cdot\rangle_{x,z,t}$, which stands for the time and space average along both wall-parallel directions x and z.

The drag reduction rate R can be readily expressed as a function of τ_x for CFR simulations, where the flow rate is kept constant, to give:

$$R = 1 - \frac{C_f}{C_{f,0}} \overset{CFR}{=} 1 - \frac{\tau_x}{\tau_{x,0}} \tag{5.10}$$

where $\tau_{x,0}$ is the wall shear stress in the uncontrolled case. Being based on the integral τ_w, also the drag reduction rate R is a measure of the average drag reduction over the channel walls.

Table 5.3 compares the main integral results for all the simulation cases. As expected, the integral drag reduction obtained in the two cases with confined actuation is lower than in the homogeneously controlled case. However, the comparison between the drag reduction obtained with spatially

	τ_x/ν	$100R$	$2\,\sigma_R$	AR	$100R_{\mathrm{hom}}\times$AR
Reference	8.37	–	–	–	–
Homogeneous	7.53	10.0	0.20	1	–
LL	8.19	2.1	0.19	0.22	2.2
LW	7.88	6.1	0.16	0.59	5.96

Table 5.3: Comparison of the integral streamwise wall shear τ_x and integral drag reduction rate R between homogeneous, limited-length and limited-width cases. σ_R is the standard uncertainty of the drag reduction rate, computed according to [112]. R_{hom} is the drag reduction in the homogeneous case. AR is the ratio between the controlled and the total area of the channel.

confined actuation and the homogeneous case reveals a further most interesting aspect. In particular, the integral drag reduction with confined actuation is very close to the product of the drag reduction $100\,R_{\mathrm{hom}}$, obtained in the homogeneously controlled case, with the area ratio AR, ratio between the controlled and the total area of the channel wall. This has an important implication for the spatial transients that exist at the borders of the actuated region. The onset transient, where the wall shear decreases from the unperturbed level of the uncontrolled channel to the lower value induced by the oscillations, and its counterpart at the opposite boundary of the controlled region, where the wall-shear increases back to its original unperturbed value, must be roughly symmetric. This evidence is confirmed in the following section.

5.2.1 Limited-length case

In the limited-length (LL) simulation, the streamwise extent of an indefinitely wide controlled region has been confined. Due to the newly introduced inhomogeneity, unperturbed turbulent flow enters the actuated region, where the spanwise movement gradually alters its wall shear, generating a streamwise spatial transient. At the foremost edge of the actuated region, an analogous recovery transient occurs. Here, turbulent flow in a lower-shear state leaves the actuated region while moving downstream and its skin friction gradually increases to the unperturbed value.

The streamwise wall shear stress is now a function of the streamwise

coordinate x and is computed as follows:

$$\tau_x(x) = \rho\nu \left.\frac{\mathrm{d}\langle u\rangle_{z,t}}{\mathrm{d}y}\right|_{y=0} \tag{5.11}$$

where the operator $\langle\cdot\rangle_{z,t}$ now stands for the average in time and along the remaining homogeneous direction z.

The streamwise development of the wall shear stress is shown in Figure 5.5 as fraction $\tau_x(x)/\tau_{x,0}$ of the integral shear-stress of the uncontrolled channel $\tau_{x,0}$. The shaded area represents the streamwise portion where the local maximum amplitude of oscillation is non-zero, i.e. where the virtual actuator is located. Within two vertical dashed line the actuation is homogeneous. An horizontal dash-dotted line marks the value of $\tau_x/\tau_{x,0}$ obtained in the homogeneous simulation.

First, no wall shear reduction is observed before the leading edge of the actuated region. This evidence is consistent with one laboratory [139] and a few numerical [94, 149, 150] measurements. Only Choi *et al.*[33] is an exception, where an upstream influence of the control was observed. The wall shear of the "fresh" turbulence entering the actuated region does not

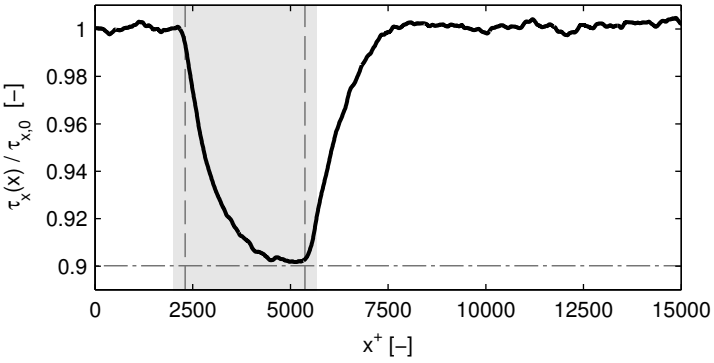

Figure 5.5: Downstream development of the wall shear stress $\tau_x(x)$ for the LL simulation, normalized by the mean wall shear $\tau_{x,0}$ of the reference channel. In the shaded area the spanwise wall velocity is non-zero. Within the vertical dashed lines the oscillation amplitude is homogeneous. The horizontal dash-dotted line marks the value of mean wall shear in the homogeneously controlled channel.

react immediately to the linearly increasing spanwise oscillations. A first decrease in shear can be observed starting from about $0.5\Delta^+_{\mathrm{ramp}}$ past the trailing edge of the actuator, where the local amplitude of oscillation is $A^+ = 1.8$. This agrees very well with the analysis by Ricco & Quadrio [138], who observed that a minimal intensity of the forcing is needed to affect the turbulent friction. Based on the definition of the empirical correlation function S (Equation 4.4), fitted with the DNS database of Quadrio & Ricco [130], they found the same value of A^+ as a minimal oscillation condition for drag reduction at oscillations with $T^+ > 30$.

The wall shear decreases gradually and reaches an asymptotic level just before the trailing edge of the actuated region, meaning that the transient is practically complete within approximately 2850 wall units. 95% of the total wall shear reduction is obtained already after 2200 wall units. This value compares very well to the available laboratory experiments, even though very different oscillation parameters and flow geometries were used. For instance, Ricco & Wu [139] measured a streamwise development of about 2200 wall units in a boundary layer with oscillations at $T^+ = 67$ and $A^+ = 11.3$. Choi *et al.* [33] observed under similar conditions a streamwise development that lasted at least 2100 wall units. More difficult to estimate due to the coarse spatial resolution, the measurements made in a boundary layer at $T^+ = 100$ with various A^+ by Gouder *et al.* [58] show a streamwise transient length of about 2000 wall units.

While the onset transient is slightly delayed, the recovery transient starts as soon as the maximum oscillation amplitude begins to decrease, i.e. Δ^+_{ramp} prior the trailing edge of the actuated region. Its downstream extent of about 2350 ν/u_τ is very close to the extent of the onset transient, showing no strong asymmetry between the two.

Figure 5.6 directly compares the present results with the laboratory experiment by Ricco & Wu [139] and the numerical investigations by Skote [150] and Yudhistira & Skote [170], all carried out in spatially developing turbulent boundary layers. The streamwise coordinate of all datasets has been rescaled in wall units, using u_τ of the unmanipulated channel for the present channel flow data and the one at the foremost edge of the controlled region for boundary layer data. Data have been shifted so that the leading edge of the actuated region coincide for all datasets and is located at $x^+ = 2000$.

In spite of the very different kinds of flow, control parameters, and hence, amount of drag reduction, the shape and downstream development (about 3000 wall units) of the onset transient is surprisingly similar for all cases.

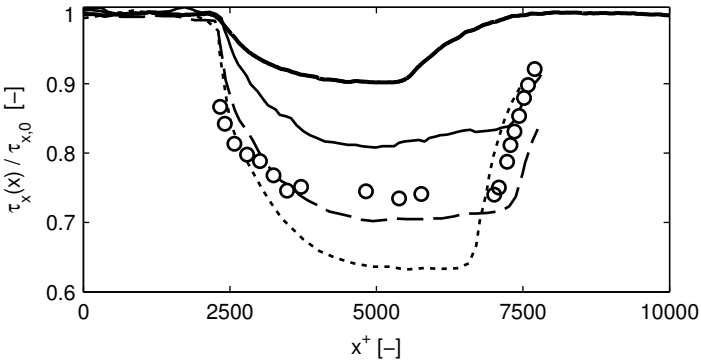

Figure 5.6: Downstream development of the wall shear stress $\tau_x(x)$, normalized by the mean wall shear $\tau_{x,0}$ of the reference channel. Thick solid line: present LL case; thin solid line: case 1 by Skote [150] ($A^+ = 6$, $T^+ = 132$); dashed line: case 2 by Skote [150] ($A^+ = 12$, $T^+ = 132$); dotted line: ($A^+ = 17$, $T^+ = 118$) by Yudhistira & Skote [170]; circles: laboratory experiment by Ricco & Wu [139] ($A^+ = 11.3$, $T^+ = 67$).

This suggests the independence, or very low sensitivity, of the spatial transient on control parameters, amount of drag reduction and flow geometry. The analogy between boundary layer and channel flow are not completely surprising and may find a rationale between the similarities of the two flows in the near-wall region [69], where the interaction between turbulent regeneration cycle and the spanwise Stokes layer occurs. More surprising is the missing dependence between the streamwise transient length and the control parameters, as this does not correspond to what happens for temporal transients in homogeneously controlled channel flows, whose duration significantly depends on A^+ [129]. Consequently, the usual approach of converting temporal transients (see for instance [8, 139] and present work Section 4.6) into spatial transients, relying upon the concept of convection velocity of turbulent fluctuations ([127], may lead to an overestimation of the spatial transient length. Moreover, the temporal transient in homogeneously controlled channel flows (not shown) is not monotonic and shows a local minimum of wall shear, followed by a recovery to a lower shear state [129]. This constitutes another difference with spatial transients observed in Figure 5.6, which show a monotonic and asymptotic behavior. At this stage, it must be noted that the slight undershoot showed by boundary

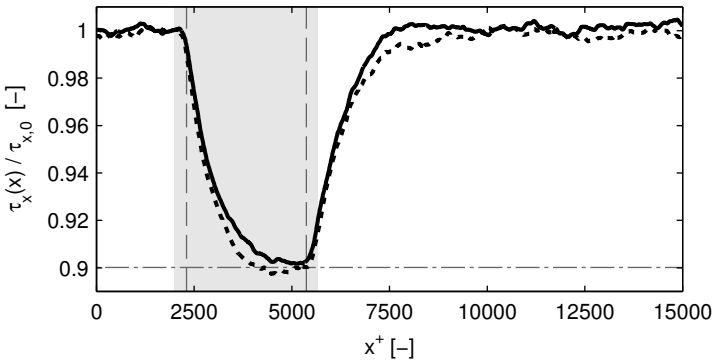

Figure 5.7: Downstream development of the wall shear stress $\tau_x(x)$ for the LL simulation. Solid line: channel flow driven at constant flow rate (CFR); Dashed line: channel flow driven at constant pressure gradient (CPG). In the latter case, $\tau_{x,0}$ is the average wall-shear in the uncontrolled region of the controlled channel flow. Other symbols as in Figure 5.5.

layer DNS data of Skote [150] is not a spatial evolution due to the sudden imposition of the control. It is rather due to the nature of the boundary layer itself, where the spatial onset transient of drag reduction and the spatial evolution of u_τ, due to the developing boundary layer thickness, intermingle. Spatial changes in u_τ induces a spatial change of the nondimensionalized control parameters, resulting in a less efficient control in the downstream region. This does not occur in the present channel flow investigation.

The recovery transient after the actuated region cannot be conclusively compared with the DNS simulation of Skote [150], as it is never resolved until its completion, probably owing to high computational costs. Nonetheless, the only simulation which shows a relatively large portion of this transient tends to confirm the previous observation. The wake transient is very similar to, yet rather shorter than, the onset transient. It exhibits a steep slope in its foremost part and a somewhat slower recovery rate at the end. This is not confirmed by the experimental measurements by Ricco & Wu [139], where the downstream extent of the recovery transient is about 2/3 shorter. Figure 5.7 compares the spatial evolution of the wall shear stress for the simulation run at constant flow rate (CFR) and at constant pressure gradient (CPG). No large differences can be observed between the

results obtained with the two simulation strategies, which are indeed very close to each other. This is again in contrast to what happens for initial temporal transients in homogeneously controlled channel flows, which are longer in CPG simulation than in CFR ones. It must be noted that temporal transients are present also in the present simulation with limited-size actuation.

Finally, a note on the CPG simulation presented as comparison in Figure 5.5. Under CPG condition, the control of either the complete or a portion of the wall results in an increase of the bulk velocity U_b at constant *average* wall shear. In the present case, only a portion of the wall is controlled, which generates a spanwise modulation of the wall shear. In the CPG framework, when the shear over the controlled section decreases, the one over the remaining uncontrolled section must increase, so as to conserve the integral wall shear. This effect vanishes as $L_x \to \infty$. In Figure 5.5, the average wall shear on the uncontrolled region has only been chosen as $\tau_{x,0}$, instead of the (always constant) global average wall shear. This seemingly arbitrary choice derives from the need to observe and compare the streamwise evolution of the wall shear past a virtual actuator and is not a direct measure of drag reduction. It reveals the difficulty to define what is meant with drag reduction in simulations within the CPG framework ([47]), especially when more exotic boundary conditions are imposed, as in the present case.

5.2.2 Limited-width case

In the limited-width (LW) simulation, the spanwise extent of an indefinitely long controlled region has been confined. Due to the newly introduced inhomogeneity, the flow properties may become a function of the spanwise coordinate and variation of the wall shear over the actuated region are expected.

The streamwise wall shear stress is now a function of the spanwise coordinate z and is computed as follows:

$$\tau_x(z) = \rho\nu \left.\frac{\mathrm{d}\langle u\rangle_{x,t}}{\mathrm{d}y}\right|_{y=0} \tag{5.12}$$

where the operator $\langle\cdot\rangle_{x,t}$ now stands for the average in time and along the remaining homogeneous direction x.

The spanwise development of the wall shear stress is shown in Figure 5.8 as a fraction $\tau_x(z)/\tau_0$ of the integral shear-stress of the uncontrolled chan-

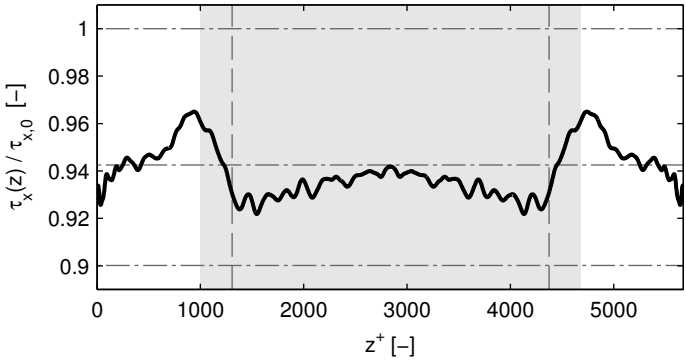

Figure 5.8: Spanwise development of the wall shear stress $\tau_x(z)$ for the LW simulation, normalized by the mean wall shear $\tau_{x,0}$ of the reference channel. In shaded area the spanwise wall velocity is non-zero. Within the vertical dashed lines the oscillation amplitude is homogeneous. The horizontal dash-dotted line marks the value of mean wall shear in the homogeneously controlled channel.

nel τ_0. The measured curves clearly show higher wiggles for the LL case. The wiggles originate from the topology of the coherent structures that populate the near-wall region. Quasi streamwise-oriented, spaghetti-like, vortical structures (quasi streamwise vortices or QSV) [70, 152, 153] lie just above the wall, starting at the uppermost part of the buffer layer. Their strong streamwise vorticity induces both high- and low-speed streaks at their sides, by pulling up low-speed fluid from the near-wall region towards the channel at one side, and pushing higher energetic flow from the bulk towards the channel walls at the other. As a result, streamwise-oriented, large fluctuation of the wall shear stress can be observed at the sides of QSV, visible as wiggles in Figure 5.8. As QSV are almost aligned with the streamwise direction [68], the average along the same direction hardly average out their induced wall-shear fluctuations. Moreover, they are advected downstream by the mean flow and recirculate in the domain due to the periodic boundary conditions, which leads to a very low variation of their streamwise position. Consequently, the very long time average adopted here was not enough to completely cancel out the wiggles.

Despite its spurious fluctuations, the spanwise distribution of the streamwise wall shear shows rather clearly a main feature: it fluctuates about a

mean value throughout the entire domain. Two upward peaks are observed at the borders of the actuated regions. Next to them, inwards the actuated region, two downward peaks can be found. Neither in the uncontrolled nor in the controlled region does the value of the local wall shear reach its uncontrolled or controlled homogeneous counterparts, which means that the effect of the control extends outside the controlled area.

This unexpected and somewhat counter intuitive feature is not surprising. Consider the scenario in which wall oscillations induce a steady reduction in wall shear on the controlled region only. Since no mean advection, that may break symmetry, occurs in the spanwise direction, spanwise gradients of streamwise shear stresses simply mix up in time by viscous and turbulent diffusion. As a result, an almost homogeneous wall shear can be observed throughout the channel.

The presence of a homogeneous wall shear combined with the imposition of a constant flow rate results in a spanwise inhomogeneity of the local mean streamwise velocity $U_b(z)$, defined as:

$$U_b(z) = \frac{1}{2\,h\,L_x\,T_{\mathrm{sim}}} \int_0^{T_{\mathrm{sim}}} \int_0^{L_x} \int_0^{2h} u \mathrm{d}x\,\mathrm{d}y\,\mathrm{d}t \tag{5.13}$$

where T_{sim} is the total simulation time after having discarded the initial

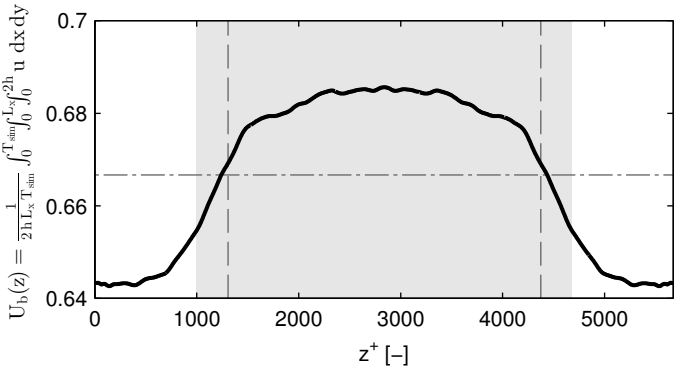

Figure 5.9: Spanwise development of local mean streamwise velocity $U_b(z)$ for the LW simulation. The bulk velocity in the uncontrolled channel is 2/3 and is here marked with a horizontal dash-dotted line. Symbols as in Figure 5.8.

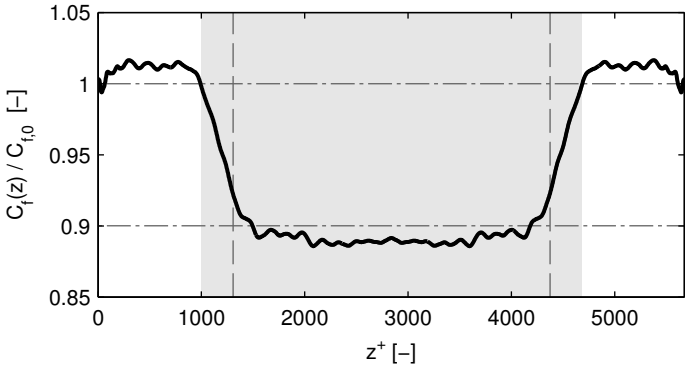

Figure 5.10: Spanwise development of local skin friction coefficient $C_f(z)$ for the LW simulation, normalized by the skin-friction coefficient $C_{f,0}$ of the uncontrolled channel. The horizontal lines mark the skin-friction of the reference and homogeneously controlled cases. Other symbols as in Figure 5.8.

transient. As figure 5.9 clearly shows, the local bulk flow velocity increases towards the center of the actuator section, while decreasing elsewhere, to fulfill the CFR constraint. The transition is smooth and the effect of the actuation extends outside the actuated area. The higher local flow rate is obtained at the cost of the same wall shear as outside the actuated region, meaning that the local skin-friction coefficient $C_f(z) = 2\tau_x(z)/(\rho U_b(z))$, based on the local bulk flow velocity $U_b(z)$, is lower over the actuated region than in the surroundings, as shown in figure 5.10. The observed phenomena are a result of the streamwise periodicity of the computational domain coupled with the unbounded geometry of the actuated section in the same direction.

The scenario over a single, isolated, spatially-confined actuator may be very different from what has been shown here. Nonetheless, one observation holds: the decrease in spanwise shear over a finite actuator causes spanwise wall shear gradients that can diffuse in the spanwise direction. This causes an acceleration of the flow over the actuated region. In a real scenario, where the streamwise extent of the actuator is limited, the acceleration means non-zero $\mathrm{d}\langle u\rangle/\mathrm{d}x$, which in turn could imply the existence of secondary motions, owing to continuity.

5.2.3 Comparison with experimental results

The information gained about the streamwise and spanwise development of the wall shear upon limited-size actuation allows us to tentatively compute the integral drag reduction about a virtual actuator, which has the same size, in wall units, as the WT1 actuator used in Chapter 4. To do so, the streamwise varying wall shear $\tau_x(x)$ is integrated between two streamwise positions, x_1 and x_2, that correspond to the locations of the taps used to measure the pressure drop across the actuator section. The LW case delivers an almost homogeneous spanwise distribution of the wall shear $\tau_x(z)$, due to the unlimited streamwise extent of the actuated region. The only quantitative information at hand, concerning limited-width actuation, results from Table 5.3, which shows the drag reduction in the limited-width and homogeneous cases to be very similar, provided that the latter is scaled with the ratio between the actuated and total wall area. Therefore, we decide to simply account for the limited width of the actuator by multiplying by the factor 2/3, the ratio between the WT1 actuator and channel width. The estimated integral drag reduction then reads:

$$R_{\text{est}} = \frac{2}{3\,(x_2 - x_1)} \int_{x_1}^{x_2} \left(1 - \frac{\tau_x(x)}{\tau_{x,0}}\right) \mathrm{d}x \tag{5.14}$$

and results in a value of 5.3%, which is still significantly higher than the 2.2% obtained in the laboratory experiment at almost identical values of T^+, A^+ and Re.

The cause of the discrepancy may be diverse. First, we studied the effect of limiting the actuated area in the streamwise and spanwise direction separately, while the combined effect of both may be different. In particular, we observed an increase in average velocity over the actuator in the limited-width case, where the actuator has a finite width but an unlimited length: A quasi homogeneous wall shear settles. Owing to continuity, this will only occur over an actuator which is also finite in length, if secondary motions in the spanwise direction are involved. In addition, the laboratory channel has side walls which are not represented in the present doubly periodic DNS. The lack of spanwise periodicity may significantly change the scenario revealed by the present LW simulation.

We conclude that the streamwise spatial transient is not the only cause of the commonly observed discrepancies between laboratory and numerical experiments, where the first exhibit lower values of drag reduction. We hint that the spanwise inhomogeneity may also play an important role in affecting integral measurements of drag reduction. A suggestive evidence

is the generally lower discrepancy, though present, observed with punctual measurement in boundary layers (for instance, [93, 139, 148, 163]) and with integral measurements in pipe flows ([8]), where the azimuthal direction is truly periodic.

5.3 Stokes layer properties

In this section we focus on the phase-average properties of the spanwise motion and in particular on the spanwise velocity and spanwise shear induced by the inhomogeneous wall motion. To this aim, we decompose the velocity vector $\mathbf{u}$ as follows:

$$\mathbf{u}(x,y,z,t) = \langle \mathbf{u} \rangle (\cdot, y) + \tilde{\mathbf{u}}(\cdot, y, \phi) + \mathbf{u}'(x,y,z,t) \tag{5.15}$$

where $\langle \mathbf{u} \rangle (\cdot, y)$ is the space and time average along the homogeneous directions and $\tilde{\mathbf{u}}(\cdot, y, \phi)$ is the phase-average periodic velocity vector. $(\cdot)$ stands for the dependency upon the additional non-homogeneous direction, that exists in simulations with spatially-confined actuation. $\mathbf{u}'$ is the random velocity field.

We stored a complete velocity field every $T/16$ time units for 30 oscillation cycles and formed a database of 480 phase-sorted fields, which have been used to compute the periodic spanwise velocity $\tilde{w}$ and the periodic spanwise shear $\mathrm{d}\tilde{w}/\mathrm{d}y$. This allow us to observe the spatial evolution of the Stokes layer and the Stokes shear induced by non-homogeneous oscillations.

We focus on the LL case first. Figures 5.11 and 5.12 show the periodic spanwise velocity $\tilde{w}(x,y)$ and spanwise shear $\partial\tilde{w}(x,y)/\partial y$ for all 16 oscillation phases at 7 different streamwise positions. The first three are located at 1/4, 1/2 and at the end of the region where the amplitude of oscillation ramps up. One is located at the center of the actuated region, while the last three are located at the beginning, 1/2 and 1/4 of the downward ramp of actuation. In the followings, the local, actual u_τ of the controlled flow is used for nondimensionalization.

Contrary to the wall shear, observed to gradually change in the previous section, the Stokes layer shows almost no streamwise development or diffusion and adapts to the local wall oscillation very quickly. Only small differences can be appreciated between position 2-4 and are due to the local change in u_τ. It is now clear that the streamwise development of the wall shear is not caused by significant streamwise changes in the Stokes layer, which immediately adapts to the local condition, even in regions where the amplitude of actuation is non-homogeneous.

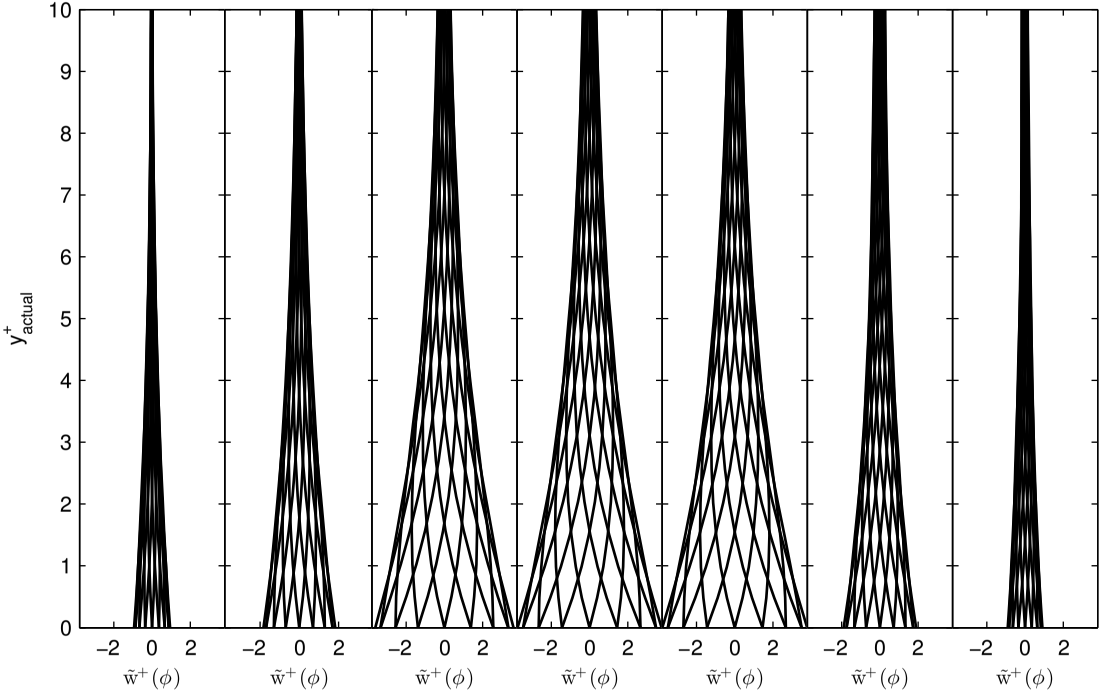

Figure 5.11: Phase-averaged spanwise velocity profiles at 7 different streamwise positions along the channel. From left to right: $0.25\Delta^+_{\text{ramp}}$, $0.5\Delta^+_{\text{ramp}}$ and Δ^+_{ramp} past the leading edge of the actuated region; in the center of the actuated region and Δ^+_{ramp}, $0.5\Delta^+_{\text{ramp}}$ and $0.25\Delta^+_{\text{ramp}}$ prior the trailing edge of the actuated region.

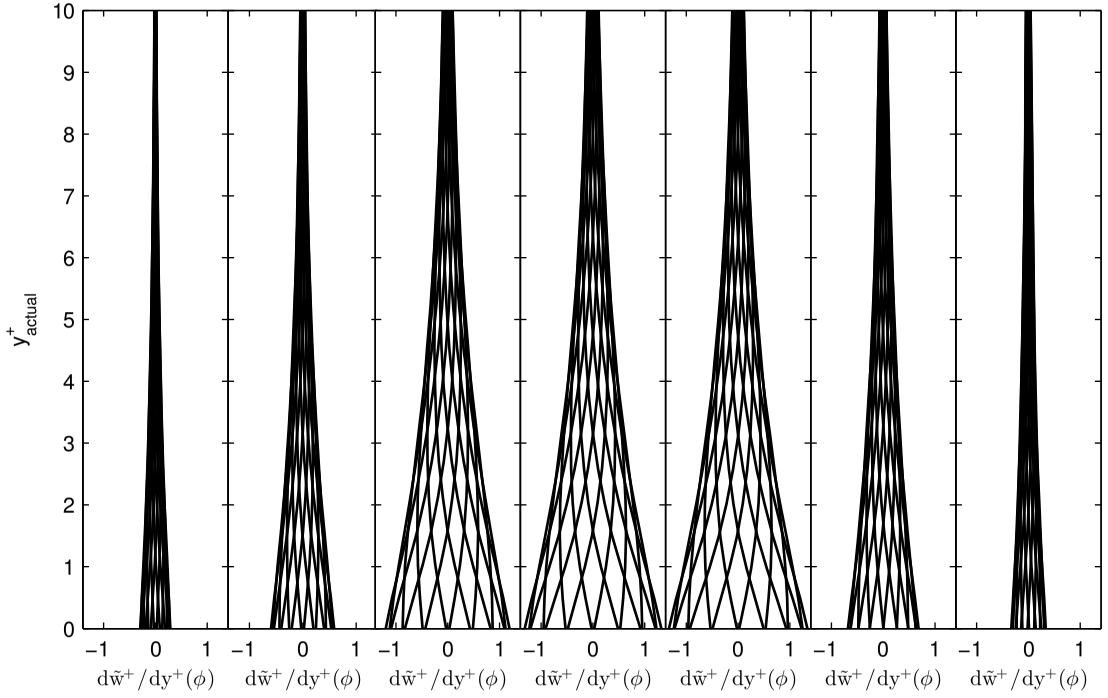

Figure 5.12: Phase-averaged spanwise shear profiles at the 7 different streamwise positions along the channel described in Figure 5.11.

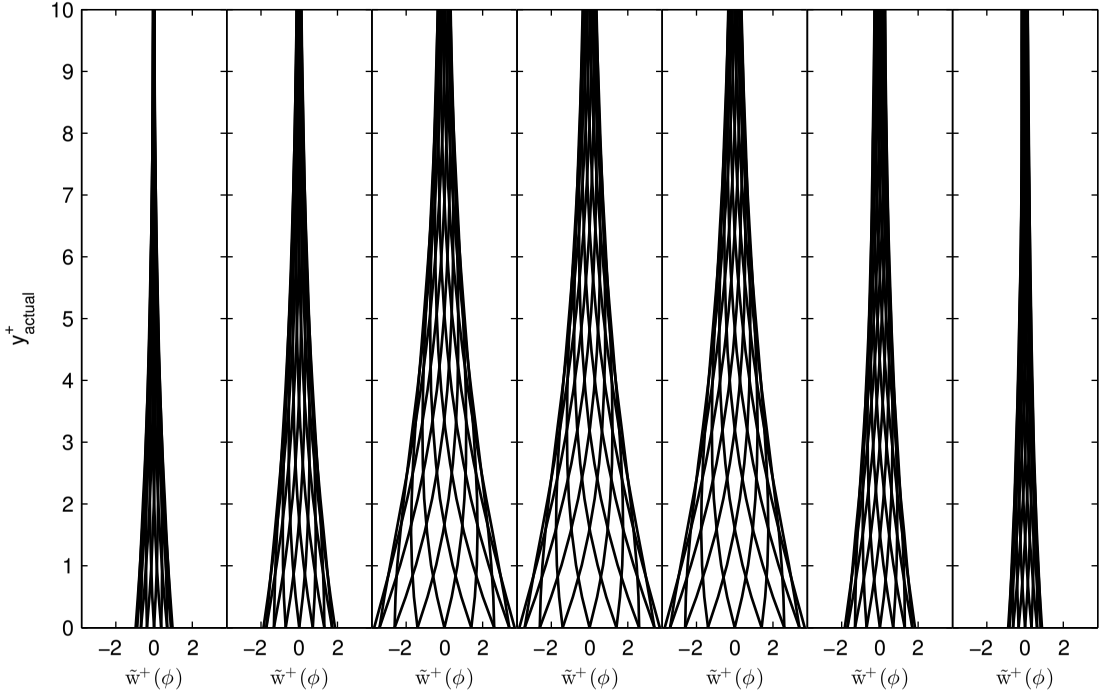

Figure 5.13: Phase-averaged spanwise velocity profiles at 7 different spanwise positions along the channel. From left to right: $0.25\Delta^+_{ramp}$, $0.5\Delta^+_{ramp}$ and Δ^+_{ramp} past the leftmost edge of the actuated region; in the center of the actuated region and Δ^+_{ramp}, $0.5\Delta^+_{ramp}$ and $0.25\Delta^+_{ramp}$ prior the rightmost edge of the actuated region.

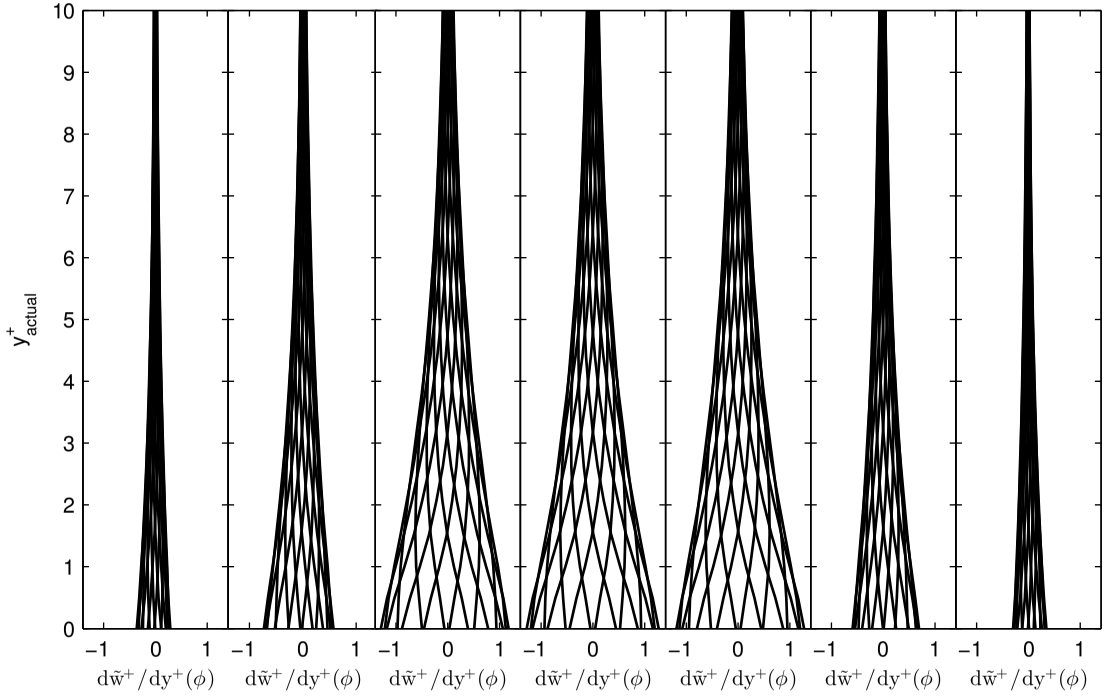

Figure 5.14: Phase-averaged spanwise shear profiles at the 7 different spanwise positions along the channel described in Figure 5.13.

The observation made for the LL case are fully confirmed for the LW case. Figures 5.13 and 5.14 show the periodic spanwise velocity $\tilde{w}(z, y)$ and spanwise shear $\partial\tilde{w}(z, y)/\partial y$ for all 16 oscillation phases at 7 different spanwise positions. Their location is analogous to the LL case: three on the upward ramp of actuation, one in the center of the homogeneously actuated region, and three on the downward ramp. The only remark is a small asymmetry of the spanwise shear profiles between the two semi-cycle of oscillation as the wall moves left and right. Positions 1-3 show slightly more pronounced negative spanwise shear, the opposite occurs for position 5-7. This is a consequence of the imposed boundary condition 5.6, which mimics a moving plate and hence imposes an oscillation on a moving boundary. A symmetric Stokes shear profile would have been observed if a reference frame that moves with the wall were adopted.

6 Influence of Re on control performance

A fundamental problem in the field of turbulent skin-friction drag reduction is to determine the performance of the available control techniques at high values of the Reynolds number Re [66, 126, 154]. Whether due to the shrinkage of space- and time- scale of wall turbulence in laboratory implementations, or to the exponential growth of the computational costs in numerical experiments, active control techniques for turbulent drag reduc-

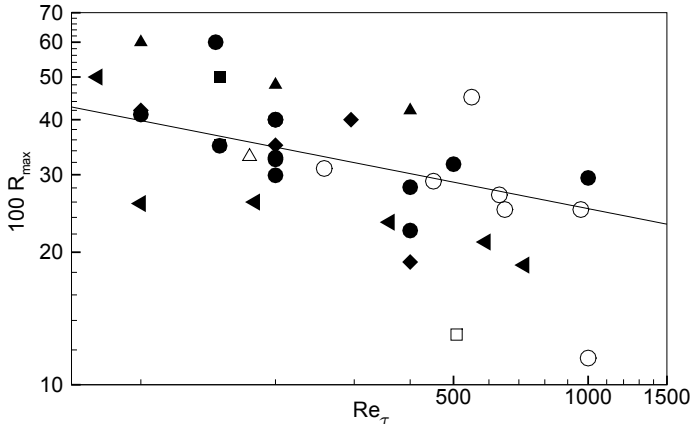

Figure 6.1: Literature data for maximum drag reduction rate $R_{\max}$ versus Re_τ for spanwise-forcing techniques. Black (white) symbols indicate results from DNS (experimental) studies. We explicitly note that the forcing amplitude is not always identical among different datasets. ○: oscillating wall [30, 33, 34, 72, 110, 130, 133, 138, 139, 158, 160, 163]; △: streamwise-traveling waves [8, 132]; □: spanwise-traveling waves [42, 43]; ◇: Lorentz force [14, 113]; ◁: reactive opposition control [29]. The solid line is $R_{\max} \sim Re_\tau^{-0.2}$.

tion are still lacking a comprehensive, thorough evaluation in high-Re flows [126], despite the fact that most applications of interest are characterized by high values of the Reynolds number Re.

The low-Re laboratory and numerical evidence available shows (Figure 6.1) that the maximum drag reduction $R_{\max}$ obtained with various control techniques based on near-wall forcing decreases for increasing Reynolds numbers, which poses the question whether sizable drag reduction is still achievable at high values of Re and hence worth pursuing.

In this Chapter, DNS information in used to obtain insights on the higher-Re performance of the spanwise-oscillating wall control technique and on its outperforming extension: the streamwise-traveling waves of spanwise wall velocity. One important distinguishing feature of this study is that a comprehensive parametric survey at higher Re is performed. In fact, most of the available studies, besides being limited to the oscillating wall, only track the neighborhood of the forcing parameters that deliver maximum drag reduction at low-Re, thus implicitly assuming that the optimal forcing conditions do not change with Re when scaled in wall units of the reference uncontrolled flow [138, 160].

Since the computational cost may rapidly become overwhelming, a large parametric study is made affordable by reducing the size of the computational domain. Shrinking this crucial discretization parameter has been shown by Gatti & Quadrio [53] to slightly bias the obtained drag reduction but only marginally affect the rate at which R decreases with Re.

The structure of the present Chapter is as follows. In Section 6.1 the numerical method and computational procedure are carefully described, along with the main discretization parameters and a brief description of the present control technique, extension of the spanwise wall oscillations. Then, the structure of the large four dimensional dataset, used to investigate a considerable part the control parameter space, is described. Section 6.2 discusses different choices for nondimensionalization and their influence on the estimation of dependency of R on Re. Finally, Section 6.3 presents the achieved drag reduction at different values of Re, first quantified through a common indicator available in literature [30], then through a novel unbiased indicator, which is found to well describe the Re-dependence of drag reduction.

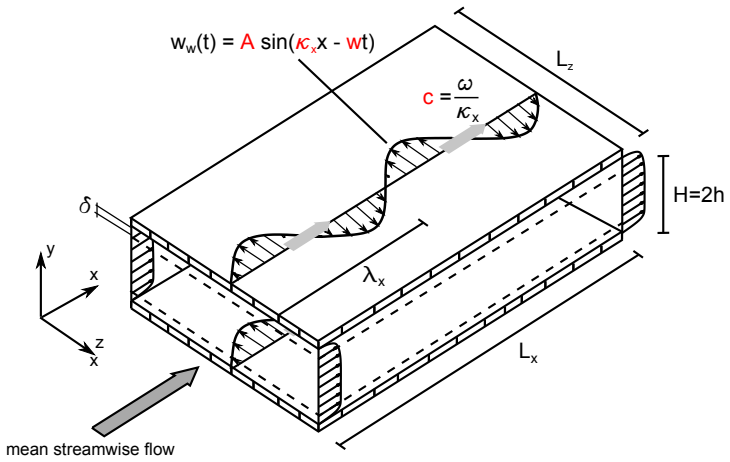

Figure 6.2: Schematic of the system for turbulent channel flow with wall traveling waves. λ_x is the streamwise wavelength and c is the phase speed of the waves (traveling forward in this sketch). L_x, L_y and L_z are the dimensions of the computational domain in the streamwise, wall-normal and spanwise directions, respectively.

6.1 Problem definition

6.1.1 Discretization and computational procedure

Direct Numerical Simulation (DNS) of turbulent flows in doubly periodic channels is used to study the effect of the Reynolds number Re on the reduction of turbulent drag reduction obtained by streamwise-traveling waves of spanwise wall velocity. From a numerical perspective, this leads to imposing at both walls the following boundary condition:

$$w_w(x,t) = A\sin(\kappa_x x - \omega t) \tag{6.1}$$

where w_w is the wall spanwise velocity, A is the amplitude of the wave, $\kappa_x = 2\pi/\lambda_x$ is the streamwise wavenumber, $\omega = 2\pi/T$ the frequency, λ_x is the wavelength and T the period. The forcing, sketched in figure 6.2, consists of a streamwise-modulated spanwise wall velocity wave with wavelength $\lambda_x = 2\pi/\kappa_x$ and period $T = 2\pi/\omega$, which travels at a speed $c = \omega/\kappa_x$ forward ($c > 0$) or backward ($c < 0$) with respect to direction of the mean flow. The three independent control parameters (A, κ_x, ω) of the control law 6.1,

combined with the Reynolds number Re, form a 4-dimensional parameter space, whose full investigation demands a insurmountable computational effort.

The newly created, large dataset is constructed with the DNS computer code developed by Luchini & Quadrio [102], adapted to best perform on the IBM Blugene/Q system at CINECA, where most of the calculations are executed. Main changes are implementation of the FFTW3 library by Frigo & Johnson [46] to efficiently compute Fast Fourier Transforms (FFTs). The peculiar feature of the present set of simulations is the limited streamwise and spanwise extent of the computational domain, as discussed below, that has made affordable the present, exceptionally large parametric study.

The governing equations are integrated forward in time, starting from an initial condition of fully developed uncontrolled channel flow generated specifically for each Reynolds number. A constant longitudinal flow rate (CFR) is kept constant and equal to $4/3hU_P$ during the simulations, where h is the channel semi-height and U_P the centerline velocity of a laminar Poiseuille flow at the same flow rate, allowing the space-averaged longitudinal friction to fluctuate in time around its time-mean value. A null instantaneous spanwise pressure gradient is imposed. Parametric DNS studies are carried out at $Re_P = U_p h/\nu = 4760$ and $Re_P = 29500$, which correspond to $Re_\tau = u_\tau h/\nu$, based on the friction velocity u_τ of the uncontrolled flow, of about 200 and 1000 respectively.

The computational domain has a streamwise length of $L_x^+ \approx 950$ and a spanwise width of $L_z^+ \approx 460$. The stream- and spanwise homogeneous directions are discretized with 96×96 Fourier modes, before aliasing, while, and 100 and 500 modes are used to discretize the y-direction at $Re_\tau = 200$ and $Re_\tau = 1000$ respectively. The streamwise and spanwise resolution are $\Delta x^+ = 9.6$ and $\Delta z^+ = 4.8$, and the wall-normal resolution varies from $\Delta y^+ = 1.0$ at the wall to 6.9 at the channel centerline. One fourth of the cases have a channel length $L_x^+ \approx 1280$ and $L_z^+ \approx 650$, to allow the imposition of control law of Equation 6.1 with several different wavenumbers. In this case, the number of Fourier modes in increased to 128×128, in order to keep the resolution unchanged. The total integration time is 12500 ν/u_τ^2. An initial transient [128] of length up to 1000 ν/u_τ^2, during which the wall shear stress decreases from the value of the uncontrolled channel down to the drag-reduced state is subtracted with an automatic procedure. Unless otherwise indicated, quantities reported hereinafter are scaled by h and U_P.

Re_P		L_x/h	L_z/h	L_x^+	L_z^+	$N_x \times N_y \times N_z$	Re_τ
4760	(A)	5.00	2.50	1000	500	$96 \times 100 \times 96$	200
4760	(B)	6.43	3.21	1286	642	$128 \times 100 \times 128$	200
29500	(A)	1.00	0.50	918	459	$96 \times 500 \times 96$	918
29500	(B)	1.36	0.68	1288	644	$128 \times 500 \times 128$	947

Table 6.1: Computational domain size, spatial resolution and friction Reynolds number Re_τ for the different sets of simulations carried out at different values of Re_P. N_x, N_y and N_z is the number of Fourier modes in the streamwise, wall-normal and spanwise directions respectively.

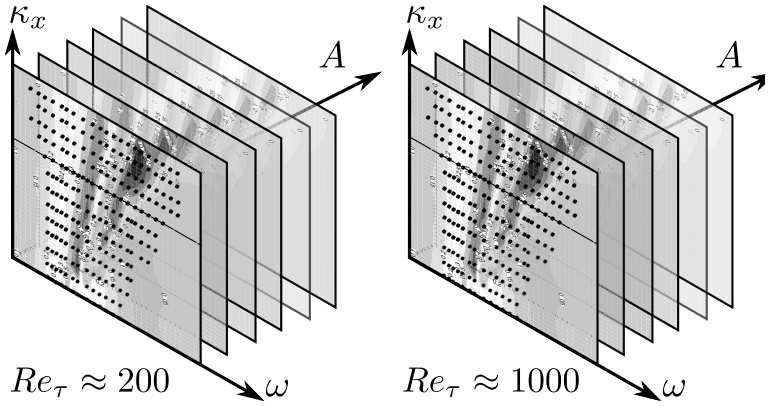

Figure 6.3: Structure of DNS database produce to study the effect of Re on control performance.

6.1.2 Control parameters

Prompted by the observation of Gatti & Quadrio [53] that the rate at which the drag reduction degrades with Re is a function of the control parameters, a vast parameter study that span a large portion of the parameter space is performed.

Figure 6.3 sketches the investigated portion of the control parameter space and aids the understanding of the enormous DNS database. 4096 independent simulations are evenly distributed between Re_τ = 200 and Re_τ = 1000. The remaining 3D parameter space (A, κ_x, ω) are first discretized in 6 slices at constant $A^+ = \{2, 4.5, 5.5, 7, 12, 20\}$. On each A^+

slice, 13 different pencils at constant wavenumber κ_x are considered, including the limiting case $\kappa_x = 0$ when the control law 6.1 reduces to the classic spanwise oscillations. Each pencils is finally divided in a (variable) discrete number of simulations, spanning a wide frequency range $-0.5 \le \omega^+ \le 1$.

In the following, several results are represented as isosurfaces at constant Re in the (A, κ_x, ω) 3D space; as contours at constant A and Re on 2D (κ_x, ω) planes or as 1D lines, in which only a variable is allowed to vary.

6.2 Viscous scaling

Control performance at different Reynolds numbers are usually compared under the reasonable assumption that the values of $(A^+, \kappa_x^+, \omega_x^+)$ that guarantee the maximum drag reduction scale in wall units. However, the definition of viscous scaling is not trivial for controlled channel flows driven at constant flow rate, for which the imposition of the control results in a change of the wall shear stress τ_x and, hence, of friction velocity u_τ. Limiting to the literature where more than one value of Re was considered, quantities have been scaled through viscous units based either on the friction velocity $u_{\tau,0}$ of the reference flow ([53, 132, 160]) or on the actual $u_{\tau,\mathrm{act}}$ of the drag-reduced flow ([108]).

Since $u_{\tau,\mathrm{act}} = u_{\tau,0}\sqrt{1-R}$, control parameters nondimensionalized by the actual and reference u_τ can be easily converted as follows:

$$A^+_{\mathrm{act}} = \frac{A^+}{\sqrt{1-R}} \qquad \kappa^+_{x,\mathrm{act}} = \frac{\kappa^+_x}{\sqrt{1-R}} \qquad \omega^+_{\mathrm{act}} = \frac{\omega^+}{1-R} \tag{6.2}$$

where R is the drag reduction rate. The choice of nondimensionalization becomes particularly delicate and may cause spurious Re effects, since R is function of all control parameters and Re.

In order to determine which scaling is more appropriate for comparing data at different Re, the drag reduction rate R achieved by wall oscillation at $A^+ = 12$ is plotted against the oscillation period T^+ and T^+_{act} in Figures Figure 6.4 and 6.5 respectively. In the following, present data are shown with empty symbols, whereas literature DNS data are shown with filled symbols. When T^+ is scaled with reference u_τ the increase of Re results in a decrease of R and in a shift of the optimal T^+ from $T^+ \approx 125$ down to $T^+ \approx 90$. However, if the oscillation period is scaled with the actual $u_{\tau,\mathrm{act}}$, the change in optimal T^+ between the two Re vanishes almost completely. Therefore, the observed shift is probably due to the decrease of R caused

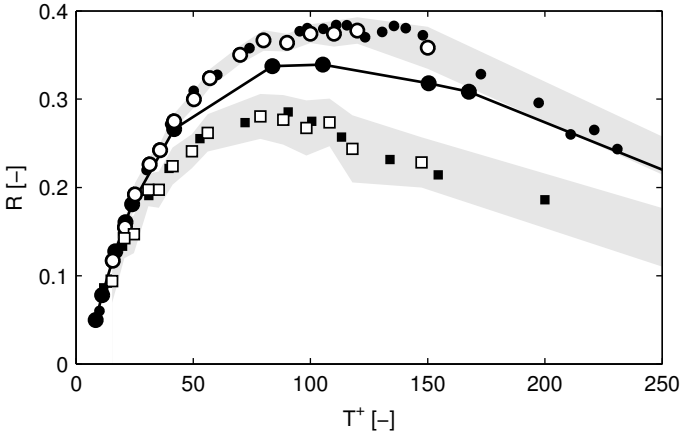

Figure 6.4: Drag reduction rate R against period of wall oscillation T^+ for oscillation amplitude $A^+ = 12$. Nondimensionalization through the friction velocity $u_{\tau,0}$ of the uncontrolled flow. ○ $Re_\tau = 200$; □ $Re_\tau = 1000$; ● and ■ are $Re_\tau = 200$ and $Re_\tau = 1000$ from Gatti & Quadrio [53] with a comparable domain size; —●— $Re_\tau = 200$ from Quadrio & Ricco [130] with a full domain size.

by Re, which reflects on an decrease of T^+_{act}, not taken into account if data are plotted against T^+.

It is worth noting that also the amplitude of oscillation A^+_{act} is not constant among the datapoints of both Figure 6.4 and 6.5. In fact, the higher R, the larger the actual oscillation amplitude A^+_{act}, thus amplifying the apparent effect of Re, whenever its change decreases R.

Normally, the only strategy to keep all control parameters constant in actual viscous units is to perform simulations at constant pressure gradient (CPG), in which the imposition of the control results in a change in U_b, while the average u_τ is imposed a priori. However, present information at different A^+ allows to predict the amount of drag reduction at a given A^+_{act} a posteriori, by interpolating the experimental data. The procedure consists of three steps. First, experimental data are linearly interpolated in the $(A^+, \kappa_x^+, \omega^+)$ space to form a Cartesian grid. Then, the grid is deformed according to Equations 6.2 to obtain $\left(A^+_{\mathrm{ref}}, \kappa^+_{x,\mathrm{ref}}, \omega^+_{\mathrm{act}}\right)$. A second linear interpolation is required to restore structured connectivity.

The results are shown in Figure 6.5 for the oscillating wall case at $A^+_{\mathrm{ref}} =$

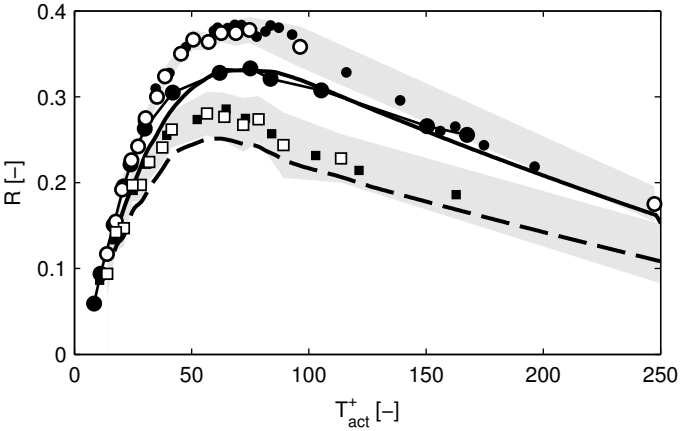

Figure 6.5: Drag reduction rate R against period of wall oscillation T^+_{act}, nondimensionalized through the friction velocity $u_{\tau,\mathrm{act}}$ of the controlled flow. Oscillation amplitude A^+ = 12. Symbols as in Figure 6.4 except: —— data Re_τ = 200 interpolated at A^+_{act} = 12; - - - data Re_τ = 1000 interpolated at A^+_{act} = 12; —●— Re_τ = 200 from Quadrio & Ricco [131] at constant pressure gradient with a full domain size.

12 as a solid and dashed line for Re_τ = 200 and Re_τ = 1000 respectively. At both Re the achieved drag reduction is lower, as it does not affect the amplitude of oscillation, which is indeed constant. The relative drop of maximum R with Re is also reduced.

Figure 6.6 compares the contours of R in both reference (a) and actual (b) scaling and extends the observations of Quadrio & Ricco [131] to higher Reynolds numbers. The highly inhomogeneity of the Re-effect throughout the parameter space makes difficult to evince whether the scaling in actual viscous units is more appropriate. However, the contour lines at Re_τ = 1000 seem to be slightly tilted compared to the low-Re ones, when scaled in reference units, probably as an effect of the lower R at high Re.

Overall, it appears that a consistent scaling of drag reduction is required for such flows, where drag reduction may be so high that the friction Reynolds number is significantly changed. The present evidence leans towards the the actual scaling as proper choice for representing the influence of the Reynolds number on control performance.

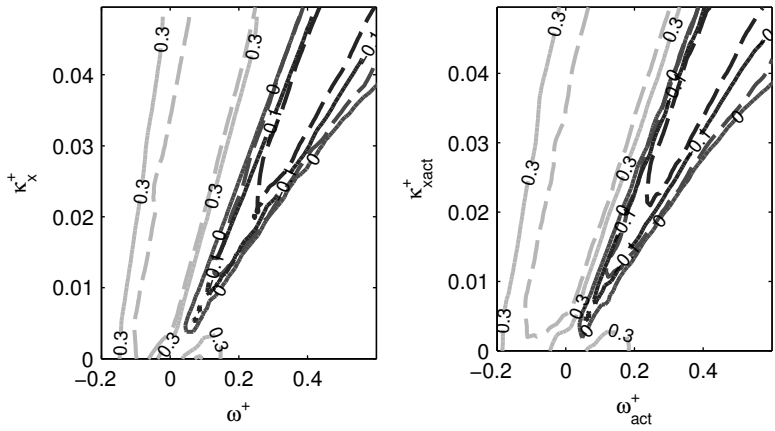

Figure 6.6: Contours of drag reduction R versus ω^+ and κ_x^+ for traveling waves at $A^+ = 12$ with reference scaling (a) and $A^+_{\mathrm{act}} = 12$ with actual scaling (b). —— $Re_\tau = 200$; - - - $Re_\tau = 1000$. Colors correspond to contours levels, which are indicated by numbers at $Re_\tau = 200$ only.

6.3 Drag reduction

In this Section, the focus is posed on the drag reduction and its dependence on both the Reynolds number Re and the control parameters. The large DNS dataset is first exploited to experimentally describe the function

$$R = (Re_\tau, A^+, \kappa_x^+, \omega^+) \tag{6.3}$$

within the large portion of the investigated parameter space. Then, the influence of Re on drag reduction, hereinafter Re-effect, is quantified through classical estimators proposed in the literature, which are shown to be unsuitable to describe function 6.3. Finally, a mathematical relationship between the Reynolds number and the drag reduction, obtained extending the concept of "protrusion height" used for riblets, is found to predict the dominant part of the Re-effect, which is not specific to the particular control technique but rather inherent in the definition of drag reduction rate. Once the protrusion height is used as unbiased estimator to epurate the pathological Re-effect, technique-specific effects of the Reynolds number can be evidenced.

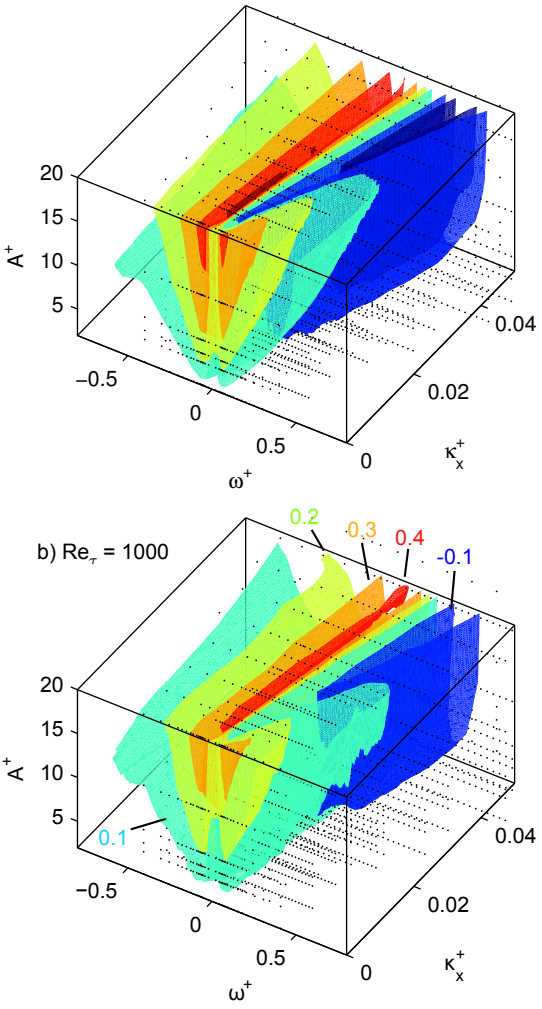

Figure 6.7: Isosurfaces of drag reduction in the 3D space (A, κ_x, ω) of the control parameters for (a) $Re_\tau = 200$ and $Re_\tau = 1000$.

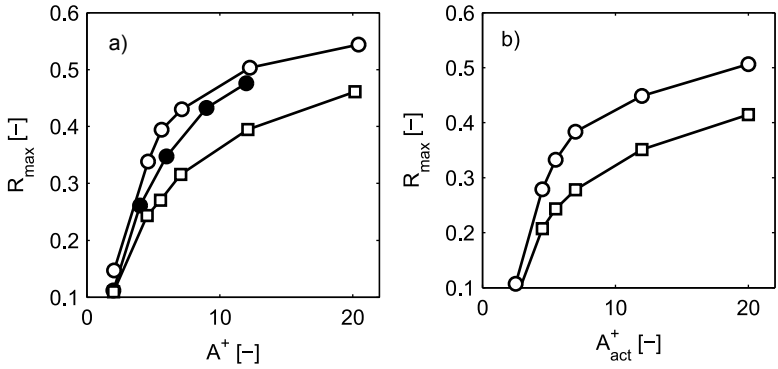

Figure 6.8: Maximum obtained drag reduction $R_{\max}$ versus the control amplitude A^+ (a), scaled in reference viscous units, and A^+_{act}, scaled in actual viscous unit. —○— Re_τ = 200; —□— Re_τ = 1000 ; —●— Re_τ = 200 from Quadrio *et al.* [132].

6.3.1 R as a function of Re_τ and control parameters

Figure 6.7 globally represents the whole DNS dataset as isosurfaces of drag reduction rate in the control parameter space. The cloud of black dots represents the 2024 datapoints used for interpolation at each Re. This overview already confirms that the drag reduction rate decreases throughout the whole dataset when the Re is increased from Re_τ = 200 to Re_τ = 1000. For instance, The connected region where $R > 0.5$ at Re_τ = 200 is not visible at Re_τ = 1000. Interestingly, the region of drag increase is most affected by the change in Reynolds number. The isosurface at $R = -0.2$ disappears at Re_τ = 1000 and the one at $R = -0.1$ shrinks significantly.

Figure 6.8 compares the maximum achievable drag reduction at the two Re against the forcing amplitude scaled in reference (a) and actual (b) viscous units. The drag reduction monotonically increases for increasing A^+ at both Re, yet at a gradually decreasing rate. The present data at Re_τ = 200 agrees well with the DNS at the same Reynolds number but with a regular domain size by Quadrio *et al.* [132]. A slight overestimation, consequence of the small domain size used in the present investigation, has been observed not to significantly bias the rate at which R depends on Re by Gatti & Quadrio [53]. Consistently with the observations of Section 6.2, when data are re-scaled in actual $u_{\tau,\mathrm{act}}$, R is lower.

Drag reduction contours in the 2D $\left(\kappa^+_{x,\mathrm{act}}, \omega^+_{\mathrm{act}}\right)$-space at constant A^+_{act} =

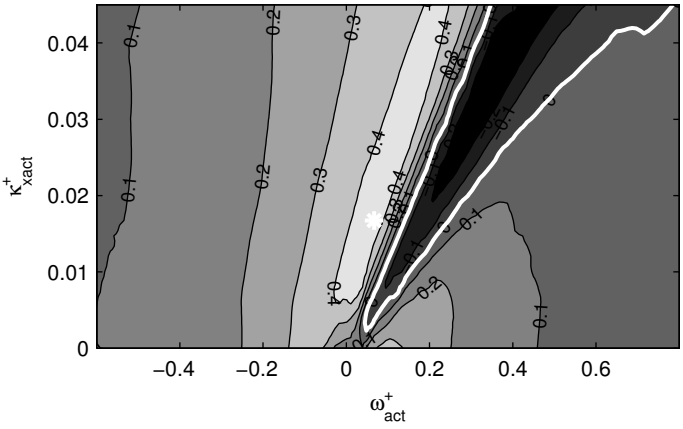

(a)

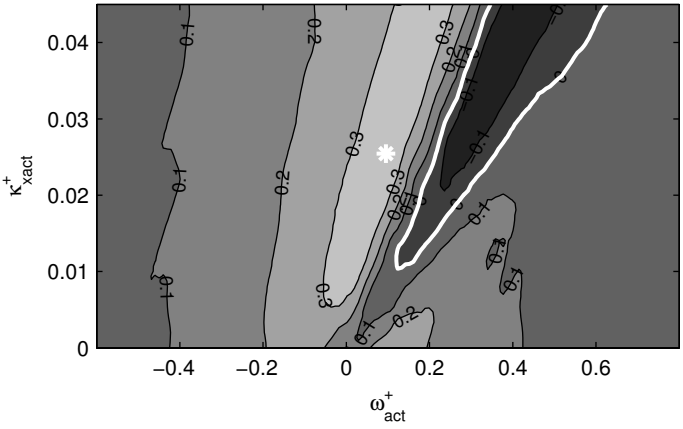

(b)

Figure 6.9: Contour of drag reduction in the $\left(\kappa^+_{x,act}, \omega\right)$ plane, scaled in actual viscous units, at $A^+_{\text{act}} = 12$. (a) $Re_\tau = 200$; (b) $Re_\tau = 1000$.

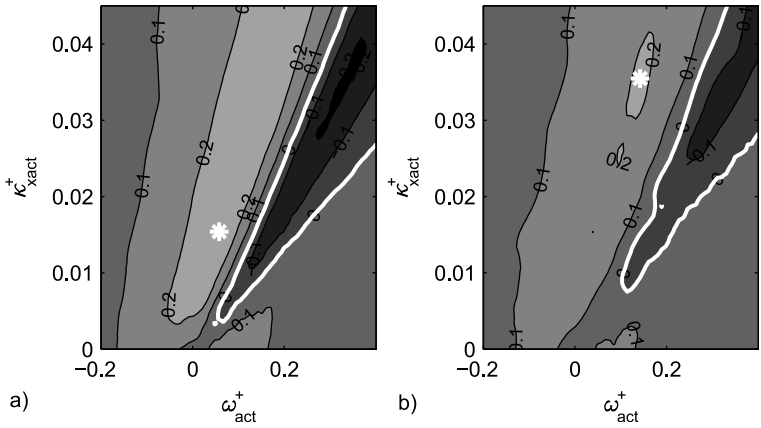

Figure 6.10: Contour of drag reduction in the $\left(\kappa^+_{x,act}, \omega\right)$ plane, scaled in actual viscous units, at $A^+_{\mathrm{act}} = 4.5$. (a) $Re_\tau = 200$; (b) $Re_\tau = 1000$.

12 are shown in Figure 6.9. The drag reduction reduces at higher Re at a rate which depends on the control parameters, being steeper in the low-wavenumber, low-frequency tail of the ridge of drag reduction ad valley of drag increase, as anticipated by Gatti & Quadrio [53]. As a result location of the maximum drag reduction in the $\left(\kappa^+_{x,\mathrm{act}}, \omega^+_{\mathrm{act}}\right)$ plane lifts upwards along the ridge toward higher wavenumber and frequencies. The shrinkage of the low-wavenumber tail of the drag increase region is such that portions of the parameter space leading to drag increase at $Re_\tau = 200$ yield drag reduction at $Re_\tau = 1000$, as the upward shift of the zero-R contour shows.

The same can be observed at the lower forcing amplitude at $A^+_{\mathrm{act}} = 4.5$, where the region at $R > 0.2$ significantly shrinks when Re_τ is increased from $Re_\tau = 200$ to $Re_\tau = 1000$. However, the contour $R = 0.1$ is practically unaffected by the change of Re, which indicates that R is less sensitive to Re at higher frequencies.

6.3.2 Relative change of R

To describe quantitatively how a change in Re affects the drag reduction rate R, it can be assumed that, at least within the present range of Reynolds numbers, the functional 6.3 simplifies to:

$$R = R\left(Re_\tau, A^+, \kappa^+_x, \omega^+\right) = g\left(Re_\tau\right) f\left(A^+, \kappa^+_x, \omega^+\right) \tag{6.4}$$

where the function $g(Re_\tau)$ reads:

$$g(Re_\tau) = \alpha Re_\tau^\gamma \tag{6.5}$$

with α and γ two empirical coefficient. The seemingly arbitrary choice of evaluating the Re-effect in terms of the coefficient γ is proposed for the first time by J.-I. Choi *et al.* [30], which suggest $\gamma \approx -0.2$ for the oscillating wall technique. Since then, it has been used as simple benchmark in many other studies [44, 53, 108, 160], which essentially confirmed the result. However, other choices are possible and should be considered. Belan & Quadrio [13], for instance, found that their predictions of maximum achievable R, computed for a bulk Reynolds number up to one million, are better fitted by a law of the type $g(Re_\tau) = \alpha + Re_\tau^\gamma$. Obviously, both the coefficients α and γ could eventually be considered as functions of the parameters themselves, and/or of Re.

Sticking to the functional dependence of Equation 6.5, the coefficient γ can be computed as:

$$\gamma = \frac{\log\left(R_2/R_1\right)}{\log\left(Re_{\tau,2}/Re_{\tau,1}\right)} \tag{6.6}$$

and is represented in Figure 6.11 for waves at $A^+ = 12$ in reference (a) scaling and $A^+_{\mathrm{act}} = 12$ in actual (b) scaling. Contours of high drag reduction and high drag increase are also superimposed, to ease the understanding. In contrast to what observed for drag reduction, the map of γ present a high noise level, especially in region where the drag reduction is lower. Moreover, it is worth noting that Equation 6.6 is undefined in regions of the parameter space where the increase in Re causes the sign of R to change or where $R = 0$. The measured value of γ varies strongly throughout the parameter space. It it $\gamma \approx -0.3$ in the region of drag increase and about the center of the axis, i.e. for wall oscillations at large periods; it is $-0.3 \leq \gamma \leq -0.2$ on the part of the drag reduction ridge that is closer to the drag increase valley; it is $\gamma \approx -0.1$ elsewhere. Interestingly, a large part of the drag reduction ridge exists, where R decays at a slower rate than the well accepted value of $Re_\tau^{-0.2}$. The present scenario is consistent also for different values of A^+ (not shown).

Beside infringing the functional dependence 6.4, the strong dependency of γ on the control parameters suggests that it may not be a suitable parameter to efficaciously describe the dependency of R on Re.

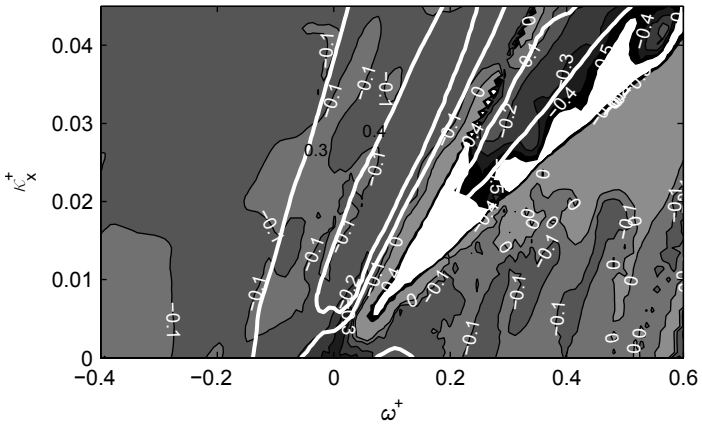

(a)

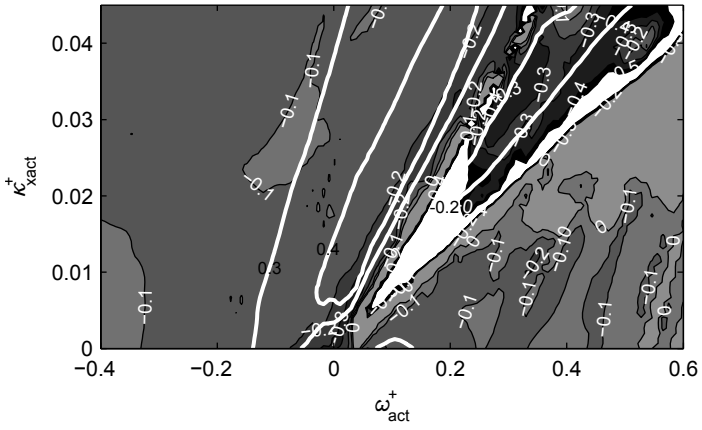

(b)

Figure 6.11: Contour of the sensitivity exponent γ in the $\left(\kappa_{x,act}^+, \omega\right)$ plane, computed at $A^+ = 12$ and reference scaling (a) or at $A_{\text{act}}^+ = 12$ and actual scaling (b).

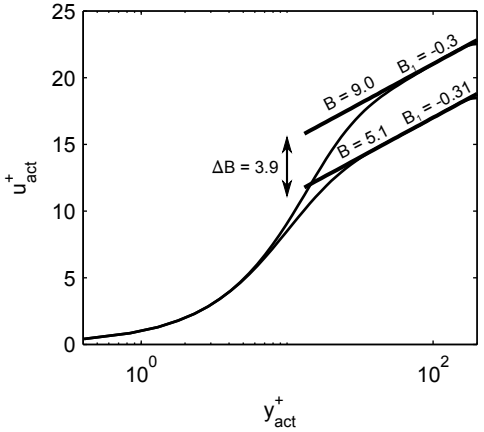

Figure 6.12: Mean velocity profile u^+_{act} versus y^+ before and after the imposition of wall oscillations, obtained through DNS of a channel flow at constant pressure gradient and Re_τ = 200. Number are the coefficients of Equation 6.8.

6.3.3 Mathematical relationship between R and Re

The concept of "protrusion height", well-known in the field of passive control by riblets [51, 101], is here extended to the present active control technique, in order to find a mathematical relationship between R and Re, which bases on the control-induced changes of mean turbulent velocity profile.

Figure 6.12 shows the mean streamwise velocity profile u^+_{act} versus the wall normal coordinate y^+ of a channel flow before and after the imposition of wall oscillations at T^+_{act} = 75. Two additional simulations at constant pressure gradient and regular domain size of $L_x = 4\pi h$ and $L_z = 2\pi h$ are performed, in order to guarantee unambiguous viscous scaling.

Similarly to what usually observed for riblets, the forcing results in an upward shift of the logarithmic velocity profile:

$$u^+ = \frac{1}{\kappa} \ln y^+ B \tag{6.7}$$

where $\kappa = 0.41$ is the von Kármán constant and B is the so-called near-wall intercept and defines the "height" of the log-law.

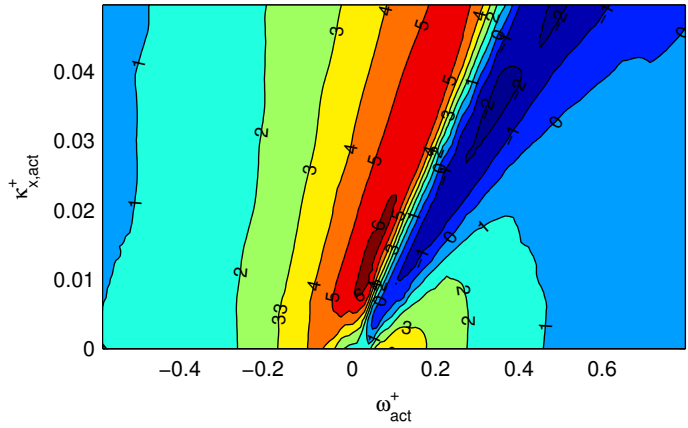

(a)

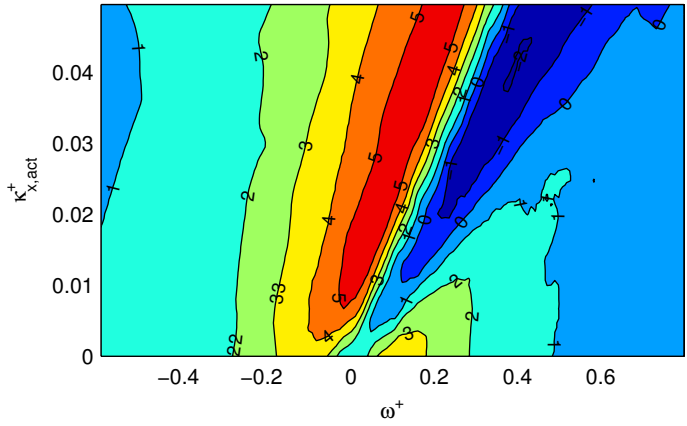

(b)

Figure 6.13: Contour of the unbiased estimator ΔB in the $\left(\kappa^+_{x,act}, \omega\right)$ plane, scaled in actual viscous units, at $A^+_{\text{act}} = 12$. (a) $Re_\tau = 200$; (b) $Re_\tau = 1000$.

The Prandtl-von Kármán friction relation holds for both controlled and uncontrolled turbulent channel flows and reads:

$$\frac{U_c}{u_\tau} = \frac{1}{\kappa}\ln\left[Re_c\frac{u_\tau}{u_c}\right] + B + B_1 \tag{6.8}$$

where B_1 is a constant independent of the wall layer. The DNS data of Figure 6.12 show that B_1 is not significantly affected by the imposition of the control. Equation 6.8 can be rewritten in terms of Re_τ and $c_f = 2\left(u_\tau/U_c\right)^2$ as follows:

$$\sqrt{\frac{2}{c_f}} = \frac{1}{\kappa}\ln Re_\tau + B + B_1 \tag{6.9}$$

As in turbulent channel flow U_c is not a convenient velocity scale, it is convenient to convert Equation 6.9 in terms of U_b by substituting Equation 2.15 to obtain:

$$\sqrt{\frac{2}{C_f}} = \frac{1}{\kappa}\ln Re_\tau + B + B_1 - \frac{1}{\kappa} \tag{6.10}$$

Equation 6.8 is evaluated at both $C_{f,0}$ and C_f, the friction coefficient of the uncontrolled case at $Re_{\tau,0}$ and of the drag-reduced channel at Re_τ. By subtracting the two relations one obtains:

$$\sqrt{\frac{2}{C_f}} - \sqrt{\frac{2}{C_{f,0}}} = \frac{1}{\kappa}\ln\frac{Re_\tau}{Re_{\tau,0}} + \Delta B \tag{6.11}$$

where ΔB is the upward lift of the log-law region due to the imposition of the control.

Under the assumption of constant flow rate, Equation 6.11 can be further manipulated by substituting $C_f = C_{f,0}\left(1-R\right)$ and $Re_\tau = Re_{\tau,0}\sqrt{1-R}$, to yield:

$$\Delta B = \sqrt{\frac{2}{C_{f,0}}}\left[\left(1-R\right)^{-1/2} - 1\right] - \frac{1}{\kappa}\ln\left(1-R\right)^{1/2} \tag{6.12}$$

In the constant pressure gradient framework for which $Re_\tau = Re_{\tau,0}$, Equation 6.11 further simplifies to:

$$\Delta B = \sqrt{\frac{2}{C_{f,0}}}\left[\left(1-R\right)^{-1/2} - 1\right] \tag{6.13}$$

provided that R is defined as the relative change in C_f.

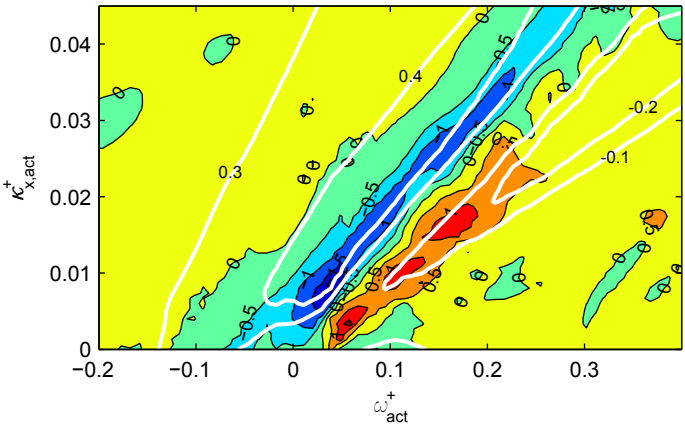

Figure 6.14: Variation of the estimator $\delta(\Delta B) = \Delta B(Re_\tau = 1000) - \Delta B(Re_\tau = 200)$ in the $\left(\kappa^+_{x,act}, \omega\right)$ plane, scaled in actual viscous units, at $A^+_{\text{act}} = 12$.

Given that the present control technique also results in a shift ΔB of the logarithmic profile and assumed that this shift depends on the properties of the generalized Stokes layer only, Equation 6.12 can be exploited to predict the effects of Re on R.

Figure 6.13 shows the map of ΔB, estimated through Equation 6.12, for traveling waves at $Re_\tau = 200$ and $Re_\tau = 1000$. Data are represented in actual scaling and the forcing amplitude is $A^+_{act} = 12$. The maps of ΔB at the two different Re appear very similar, meaning that a ΔB is only marginally influenced by a change of Reynolds number. ΔB is therefore an unbiased estimator of drag reduction, in the sense that it is strictly related to the drag reduction ratio, epurated from the Re-dependency which just arises from natural changes of the mean velocity profile with Re.

The difference between the two maps $\Delta B\,(Re_\tau = 1000) - \Delta B\,(Re_\tau = 200)$ is shown in Figure 6.14, together with the contours of high drag reduction and drag increase at low Re. The change in ΔB represents the non trivial component of the Re-effect, which is deemed to be specific of the present control technique. The variation of ΔB with Re is identically zero for a large part of the parameter space, except on a small strip centered between the drag reduction and drag increase region and is severer at very-low frequencies and wavenumbers. Interestingly, a part of the drag reduction ridge leading $R > 0.3$ is mostly unaffected by technique-specific effects of

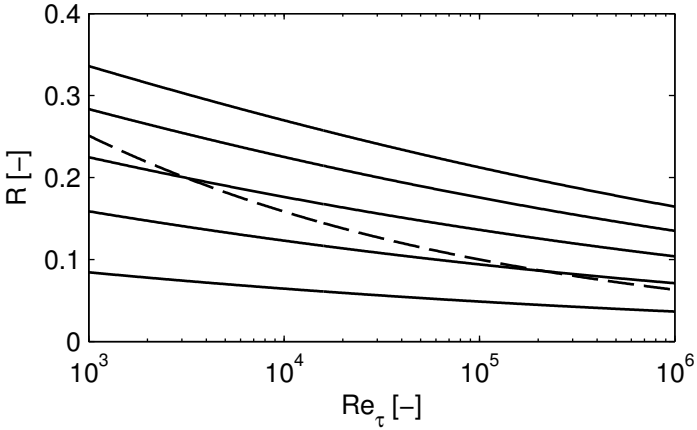

Figure 6.15: Drag reduction at high-Re. —— Prediction of Equation 6.12, assuming that ΔB does not vary with Re; - - - empirical law $R \propto Re_\tau^{-0.2}$;

the Reynolds number, hinting the possibility of high drag reduction at high values of the Reynolds number.

For the first time, figure 6.14 shades light on the effect of Re on drag reduction, highlighting the non trivial Re-effect that must be related with the modification in the interaction between the Stokes layer and near-wall turbulence with Re.

The capability of Equation 6.12 to correctly predict the unavoidable part of the Re-effect can be exploited to tentatively extrapolate the amount of drag reduction theoretically achievable at high values of Re_τ, as done in Figure 6.15. Here, the drag reduction rate obtained with $\Delta B = 1 \div 5$ is computed at Re_τ up to 10^6, assuming that ΔB is constant with Re. Sizable drag reduction could be theoretically achieved. Therefore, future effort should be focused on understanding the mechanisms behind the technique-specific Re-effect, in order to develop control techniques less prone to it.

7 Summary and Conclusions

The present work faced main open issues concerning the practical implementation of flow control aimed at turbulent skin-friction drag reduction via spanwise wall oscillations. First, actuators based on a novel technology have been investigated, developed and tested. The effect of using actuators with finite and small size has been assessed. Finally, the capital question whether drag reduction can be achieved in turbulent flow at high Reynolds number has been addressed.

In Chapter 3, the suitability of dielectric elastomer actuators (DEA) for turbulent flow-control applications have been assessed. The influence of a major design parameter, the amount of pre-stretch given to the elastomer membrane, has been found to largely influence the dielectric and mechanical properties of DEAs. As a consequence, static and dynamic actuation performance has been tuned by varying the amount and direction of pre-stretch. An optimal pre-stretch combination has been found to yield the best trade-off between actuation amplitude and frequency. Main phenomena occurring during dynamic actuation of the simplest dielectric elastomer membrane actuator have been investigated, showing that inhomogeneous large and fast wall-oscillations at frequency up to 200 Hz is possible. The hyperelastic properties of the dielectric membrane have been used to explain and eventually predict the experimental evidence. Finally, DEA-based oscillating surfaces, capable of large in-plane wall motions, have been developed, focusing on improving robustness and reliability, their Achilles' heel. Their electromechanical response has been characterized and described through simple phenomenological models, which allow the estimation of the electromechanical efficiency. The real power required for imposing wall oscillations has been measured.

Spanwise oscillating surfaces based on dielectric elastomer actuators have been tested in a laboratory experiment conducted in a fully turbulent air channel flow. Their integration into the wind tunnel is carefully described and shown to be of crucial importance, as the smallest imperfections and unevenness resulted in higher values of the baseline skin friction even at low Reynolds numbers. Relative reductions of the skin-friction drag up to 2.5% have been measured when the actuator were arranged in opposite-wall

configuration. The present result has been compared with the available literature data through a well-established empirical correlation and poor agreement has been shown, being the achieved drag reduction lower. The existence of a spatial transient at the leading edge of the actuated section, where the wall shear decreases from the unperturbed level of the uncontrolled channel to the lower value induced by the oscillations, has been investigated as possible cause of the disagreement. First, the empirical correlation has been corrected to account for the spatial transient, whose extent has been estimated by converting DNS information on initial temporal transient through the concept of convection velocity of skin-friction fluctuations, showing qualitative agreement, especially regarding the value of the optimal period of oscillation. Then, additional experiments have been realized, in which three actuators have been cascaded downstream, thus imposing spanwise oscillation on a longer streamwise portion of the channel. Reduction of friction drag up to almost 5% have been measured. For the first time in the field of spanwise oscillation, the information on real power consumption of the actuator system has been exploited to evaluate the energetic efficiency of the control, in terms of net power saving, the balance between the control savings and costs, and gain, measure of the overall efficiency of the control, product of the electromechanical and aerodynamic efficiency. Although negative, the net power saving enabled by dielectric elastomer actuators is several order of magnitude larger than what estimated with conventional actuator technologies in previous studies.

In Chapter 5, the effect of inhomogeneous actuation, occurring at the boundaries of an actuated region of finite extent, have been studied by Direct Numerical Simulations of fully developed turbulent channel flows, focusing on eventual changes in maximum achievable drag reduction. To this aim, the streamwise and spanwise extent of the controlled region has been limited and the spatial distribution of wall shear measured. The streamwise spatial transient at the leading edge of the actuator has been found to extend for 3000 ν/u_τ downstream. A comparison with results available in literature has shown that the transient is insensitive to changes of control parameters or flow geometry. The longer initial temporal transient observed in channel flows driven at constant pressure gradient (CPG) with respect to the constant flow rate (CFR) counterparts does not correspond to a longer spatial onset transient, as additional numerical simulation performed in CPG framework has shown. Limiting the spanwise extent of the controlled region results in the production of wall-normal velocity in the regions where the spanwise velocity varies in the spanwise direction, owing

to continuity. The effect of the control extends outside the control region and the flow over the actuator locally possess higher mean velocity. The effect of inhomogeneous actuation have been investigated as source of the discrepancy between the wind-tunnel measurements and the prediction of empirical correlations based on numerical results, by directly comparing the experimental investigations to their numerical idealized representation. Although the presence of the spatial transient decreases the achievable value of drag reduction, it does not completely explain the lower value of drag reduction measured in the laboratory experiment, which is still almost two times lower than the numerical simulation with finite actuation. It has been argued that the combined effect of limited stream- and spanwise extent of the actuated region on drag reduction could be stronger than in the present simulations, in which the two direction have been addressed separately.

The rate at which the drag reduction deteriorates at increasing Re has been investigated in Chapter 6. Streamwise-traveling wave of spanwise wall velocity, a generalization of the spanwise wall oscillations, has been chosen as model control strategy thanks to its high theoretical energetic performance. A newly created, large DNS dataset of fully developed turbulent channel flows modified by traveling waves with various control parameters at $Re_\tau = 200$ and $Re_\tau = 1000$ has been produced and explored. It has been demonstrated that the control-induced modification of the mean turbulent velocity profile consists of an upward shift of the logarithmic region, described by the near-wall intercept coefficient B. In analogy with riblets, it has been assumed that B depends on the properties of spanwise generalized Stokes layer only and not on Re. This hypothesis has been proven to be valid for most DNS data, for which an equation has been derived that predict the rate at which the drag reduction decay with Re, which has been employed to predict that sizable drag reduction can be achieved at Re typical of most aeronautical applications. For some datapoints, confined in a small region of the control parameter space, B has been found to change with Re. Here, the existence of a Reynolds number effect that is specific to the present control technique has been clearly evidenced.

The presented work addressed different open questions of fundamental interest in the field of flow control. Nonetheless, during this work many other new open issues were recognized, which should be addressed in future work to help understand the phenomena behind skin-friction drag reduction and to guide future attempt of its implementation.

Dielectric elastomer actuators have been investigated for flow control application. Further improvement of their electromechanical characteristic

can be achieved through miniaturization, which reduces dielectric failures, improves the out-of-plane stiffness and increases the resonance frequency. Further work should be oriented in developing arrays of miniaturized actuators. Batch-processing manufacturing should be considered as means to achieve high degree of reproducibility among actuator batches.

Actuator arrays seem a viable strategy to locally implement wall oscillations on a large surface. However, the effect of inhomogeneous actuation have been found to influence the amount of achievable drag reduction. Future studies should assess the effect of inhomogeneous actuator and investigate the existence of actuator arrangements that optimize the achievable amount of drag reduction.

Although the streamwise transient of drag reduction has been observed to reduce the achievable amount of drag reduction on an actuator surface, it does not completely explain the discrepancy between the amount of drag reduction obtained in laboratory and numerical experiments. Further investigations should be aimed at thoroughly investigating other possible causes of the disagreement, especially when the actuated region is relatively small in size.

The Reynolds number effect on drag reduction has been shown to be mostly caused by the shrinking of the near-wall region, when scaled in outer units, for increasing Re. Other effect of Re have been evidenced which just depend on the present control technique and occur for specific combinations of the control parameters. Further studies should be aimed at investigating how the induced spanwise wall shear interacts with near-wall turbulence, in order to explain the mechanisms behind the loss of control performance with Re.

A Scaling of flow quantities

Flow and flow-related quantities have been often presented throughout the work in nondimensional form. This practice has the major advantage of immediately highlighting the relative magnitude of a quantity with respect to typical flow velocity, time and length scales, which are meaningful for the investigated flow phenomena. However, estimating the physical dimension of such nondimensional quantities can be difficult, especially for the readers approaching the field of fluid mechanics for the first time. This appendix briefly recalls the characteristic flow scales which have been used for nondimensionalization and estimates their dimensions for typical laboratory or numerical experiments performed in the present work. Characteristic velocity, time and length scales can be very diverse depending on the kind of flow which is considered. The following discussion refers to a channel flow, the model problem considered in the present work, but extends with few modifications to other wall-bounded flows as pipe flows and boundary layers. In a statistically stationary turbulent channel flow two main flow scales are identified: the outer and the inner scales.

Outer scaling

The outer scales are easily defined relying upon the basic integral properties of the flow. The outer length scale L is a characteristic length of the flow domain in internal flows or of the wetted body in external ones. In the present case of a channel flow, the length scale L is the channel semi-height h, which is expected to be the characteristic size of the largest flow features in the channel. A typical velocity scale U_b is the bulk flow velocity, i.e. the average volumetric flow rate per unit cross-sectional area, which is typical of the advection process by the mean flow. Typical large flow features of size L are advected downstream by the mean flow with a velocity U_b. A time scale t can be obtained by combining the outer velocity and length so that $t = L/U_b$. In other words, t is the time which a flow with average velocity U_b requires to flow over a distance L. In the laboratory channel flow investigated in the present work the channel semi-height is $L = 12.6$ mm, the bulk velocity is varied between 3 m/s and 9 m/s and the typical

outer timescale varies accordingly between 0.0042 s and 0.0014 s. In Direct Numerical Simulations performed at constant flow rate, the outer scaling is the natural choice for nondimensionalization, since all the aforementioned flow scales are known and imposed a priori.

Inner scaling

Near the wall of wall-bounded flows the viscous diffusion of momentum is largest and thus plays an important role in determining the local flow properties. It may be argued that typical flow features which occur close to the wall have dimensions which are related to the typical velocity, length and time scales of skin-friction. These scales can be readily derived from characteristic friction-related quantities such as the kinematic viscosity ν, and the wall shear stress τ_w. The velocity scale u_τ, the so-called friction velocity, typical of viscous diffusion of momentum, is obtained as follows:

$$u_\tau \quad [m/s] = \sqrt{\frac{\tau_w \quad [kg^2/s^2m]}{\rho \quad [kg/m^3]}} \tag{A.1}$$

A characteristic length of the viscous diffusion phenomena, named viscous length δ_ν, follows as:

$$\delta_\nu \quad [m] = \frac{\nu \quad [m^2/s]}{u_\tau \quad [m/s]} \tag{A.2}$$

In this way the kinematic viscosity $\nu = \delta_\nu u_\tau$ can be interpreted as the product of the friction velocity u_τ and the viscous length δ_ν. The typical time scale of friction is the viscous time

$$t_\nu \quad [s] = \frac{\delta_\nu}{u_\tau} = \frac{\nu \quad [m^2/s]}{u_\tau^2 \quad [m^2/s^2]} \tag{A.3}$$

simply computed from the viscous length and velocity scales.

The ratio between the viscous and the outer length scale yields a very important nondimensional parameter, the friction Reynolds number Re_τ, frequently used in the present work:

$$\frac{\delta_\nu}{h} = \frac{\nu}{u_\tau h} = \frac{1}{Re_\tau} \tag{A.4}$$

where obviously $Re_\tau = u_\tau h/\nu$. It results that the friction Reynolds number is a comparison between the order of magnitudes of the typical length

scale of viscosity relative to the characteristic outer length scale of the flow problem. The higher Re_τ, the thinner is the region close to the wall in which the viscous effects are predominant.

As already shown in Chapter 2.1, the viscous scales play an important role in the description of near-wall turbulence. In fact, many flow properties, such as the region above the wall in which the mean streamwise velocity grows linearly, the average size of vortical structures, the amplitude of velocity fluctuations, becomes nearly independent of the Reynolds number, once non dimensionalized with viscous units. Particularly interesting for the present work is the fact that the period at which wall oscillations achieve the maximum drag reduction is constant with Re_τ if scaled in viscous units. This suggests that the time scale of the wall actuation relative to the time scale of viscous diffusion is an important parameter for successful actuation and, indirectly, that drag reduction may be related to modifications of the turbulent flow within the near-wall region, where viscous effects are dominant.

In both numerical and laboratory experiments of the present work the Reynolds number based on the bulk flow velocity U_b and the channel height is typically $Re_b = 2U_b h/\nu \approx 6000$, which corresponds to a friction Reynolds number Re_τ of about 200. In the laboratory channel flow this Reynolds numbers are achieved at a bulk velocity of approximately 3.5 m/s in air at room temperature, for which the kinematic viscosity is 1.49×10^{-5}. The wall shear stress τ_w has been measured to be 0.065 Pa, which corresponds to a friction velocity u_τ of about 0.23 m/s when the air density is 1.20 kg/m^3. As a result the friction length is then as small as 66 μm and the viscous time t_ν corresponds to 2.80×10^{-4} s.

Bibliography

[1] M. Acarlar and C. Smith. A Study of Hairpin Vortex in a Laminar Boundary Layer. Part I. Hairpin Vortex Generated by a Hemisphere Protuberance. *J. Fluid Mech.*, 175:1–41, 1987.

[2] V. Agarwal and V. Srivastava. Thickness dependence of breakdown field in thin films. *Thin Solid Films*, 8(5):377–381, Nov. 1971.

[3] S. Akbari, S. Rosset, and H. R. Shea. Improved electromechanical behavior in castable dielectric elastomer actuators. *Appl. Phys. Lett.*, 102(7):071906–071906–5, 2013.

[4] S. Akbari and H. R. Shea. An array of 100μm × 100μm dielectric elastomer actuators with 80% strain for tissue engineering applications. *Sens. Actuators A*, 186(0):236 – 241, 2012.

[5] S. Akbari and H. R. Shea. Microfabrication and characterization of an array of dielectric elastomer actuators generating uniaxial strain to stretch individual cells. *J. Micromech. Microeng.*, 22(4):045020, 2012.

[6] R. Akhavan, W. Jung, and N. Mangiavacchi. Control of wall turbulence by high frequency wall oscillations. *AIAA Paper 93-3282*, 1993.

[7] I. A. Anderson, T. A. Gisby, T. G. McKay, B. M. O'Brien, and E. P. Calius. Multi-functional dielectric elastomer artificial muscles for soft and smart machines. *J. Appl. Phys.*, 112(4):–, 2012.

[8] F. Auteri, A. Baron, M. Belan, G. Campanardi, and M. Quadrio. Experimental assessment of drag reduction by traveling waves in a turbulent pipe flow. *Phys. Fluids*, 22(11):115103/14, 2010.

[9] P. Bandyopadhyay. Stokes mechanism of drag reduction. *J. Appl. Mech.*, 73:483–489, 2006.

[10] J. B. Barlow, R. W. H., and A. Pope. *Low-speed wind tunnel testing*. John Wiley & Sons, 1999.

[11] A. Baron and M. Quadrio. Turbulent drag reduction by spanwise wall oscillations. *Appl. Sci. Res.*, 55:311–326, 1996.

[12] Y. Basar and D. Weichert. *Nonlinear Continuum Mechanics of Solids*. Springer, 2000.

[13] M. Belan and M. Quadrio. A perturbative model for predicting the high-Reynolds-number behaviour of the streamwise travelling waves technique in turbulent drag reduction. *ZAMM*, 2013.

[14] T. W. Berger, J. Kim, C. Lee, and J. Lim. Turbulent boundary layer control utilizing the Lorentz force. *Phys. Fluids*, 12(3):631–649, 2000.

[15] G. Berselli, R. Vertechy, B. Mitja, and V. P. Castelli. Dynamic modeling and experimental evaluation of a constant-force dielectric elastomer actuator. *J. Intel. Mat. Syst. Str.*, 24:779–791, 2013.

[16] J. Biggs, K. Danielmeier, J. Hitzbleck, J. Krause, T. Kridl, S. Nowak, E. Orselli, X. Quan, D. Schapeler, W. Sutherland, and J. Wagner. Elektroaktive polymere: Entwicklungen und perspektiven dielektrischer elastomere. *Angew. Chem.*, 125(36):9581–9595, 2013.

[17] J. L. Bigué, P. Chouinard, S. Proulx, G. Miron, and J. Plante. Preliminary assessment of manufacturing impacts on dielectric elastomer actuator reliability. In *Proc. CANSMART*, 2009.

[18] R. Blackwelder and H. Eckelmann. Streamwise vortices associated with the bursting phenomenon. part 3. *J. Fluid. Mech.*, 94:577, 1979.

[19] R. Blackwelder and R. Kaplan. On the Wall Structure of the Turbulent Boundary Layer. *J. Fluid Mech.*, 76:89–112, 1976.

[20] J. Blok. Dielectric breakdown of polymer films. *J. Appl. Phys.*, 40(1):288, 1969.

[21] C. Bolzmacher, J. Biggs, and M. Srinivasan. Flexible dielectric elastomer actuators for wearable human-machine interfaces. In *Proc. SPIE, EAPAD*, volume 6168, pages 616804–616804–12, 2006.

[22] P. Bradshaw and R. D. Metha. Design rules for small low speed wind tunnels. *Aeronaut. J.*, 73:442–449, 1979.

[23] C. G. Cameron, J. Szabo, S. Johnstone, J. Massey, and J. Leidner. Linear actuation in coextruded dielectric elastomer tubes. *Sens. Actuators A*, 147(1):286 – 291, 2008.

[24] C. Canuto, M. Y. Hussaini, A. Quarteroni, and T. A. Zang. *Spectral Methods. Evolution to Complex Geometries and Applications to Fluid Dynamics*. Springer, 2007.

[25] F. Carpi, P. Chiarelli, A. Mazzoldi, and D. De Rossi. Electromechanical characterisation of dielectric elastomer planar actuators: comparative evaluation of different electrode materials and different counterloads. *Sens. Actuators A*, 107(1):85 – 95, 2003.

[26] F. Carpi, D. De Rossi, R. Kornbluh, R. Pelrine, and P. Sommer-Larsen, editors. *Dielectric Elastomers as Electromechanical Transducers*. Elsevier, 2008.

[27] F. Carpi and M. Gei. Predictive stress/stretch models of elastomers up to the characteristic flex. *Smart Mater. Struct.*, 22(10):104011, 2013.

[28] L. N. Cattafesta and M. Sheplak. Actuators for active flow control. *Ann. Rev. Fluid Mech.*, 43(1):247–272, 2011.

[29] Y. Chang, S. S. Collis, and S. Ramakrishnan. Viscous effect in control near-wall turbulence. *Phys. Fluids*, 14:4069–4080, 2002.

[30] J.-I. Choi, C.-X. Xu, and H. J. Sung. Drag reduction by spanwise wall oscillation in wall-bounded turbulent flows. *AIAA J.*, 40(5):842–850, 2002.

[31] K.-S. Choi. Near-wall structure of turbulent boundary layer with spanwise-wall oscillation. *Phys. Fluids*, 14(7):2530–2542, 2002.

[32] K.-S. Choi and B. Clayton. The mechanism of turbulent drag reduction with wall oscillation. *Int. J. Heat Fluid Flow*, 22:1–9, 2001.

[33] K.-S. Choi, J. DeBisschop, and B. Clayton. Turbulent boundary-layer control by means of spanwise-wall oscillation. *AIAA J.*, 36(7):1157–1162, 1998.

[34] K.-S. Choi and M. Graham. Drag reduction of turbulent pipe flows by circular-wall oscillation. *Phys. Fluids*, 10(1):7–9, 1998.

[35] S. T. Choi, J. Y. Lee, J. O. Kwon, S. Lee, and W. Kim. Liquid-filled varifocal lens on a chip. In *Proc. SPIE, EAPAD*, volume 7208, pages 72080P–72080P–9, 2009.

[36] P. Chouinard and J. Plante. Bistable antagonistic dielectric elastomer actuators for binary robotics and mechatronics. *IEEE/ASME Trans. Mechatronics*, 17(5):857 –865, 2012.

[37] R. Courant, K. Friedrichs, and H. Lewy. Über die partiellen Differenzengleichungen der mathematischen Physik. *Math. Ann.*, 100(1):32–74, 1928.

[38] M. Danikas. On the breakdown strength of silicone rubber. *IEEE Trans. Dielect. Elect. Insulation*, 1(6):1196–1200, Dec. 1994.

[39] R. Dean. Reynolds number dependence of skin friction and other bulk flow variables in two-dimensional rectangular duct flow. *Trans. ASME I: J. Fluids Eng.*, 100:215, 1978.

[40] S. S. Dearing, J. F. Morrison, and L. Iannucci. Electro-active polymer (EAP) "dimple" actuators for flow control: Design and characterisation. *Sens. Actuators A*, 157(2):210 – 218, 2010.

[41] G. Di Cicca, G. Iuso, P. Spazzini, and M. Onorato. PIV investigation of turbulent boundary layer manipulated by spanwise wall oscillations. *J. Fluid Mech.*, 467:41–56, 2002.

[42] Y. Du and G. E. Karniadakis. Suppressing wall turbulence by means of a transverse traveling wave. *Science*, 288:1230–1234, 2000.

[43] Y. Du, V. Symeonidis, and G. E. Karniadakis. Drag reduction in wall-bounded turbulence via a transverse travelling wave. *J. Fluid Mech.*, 457:1–34, 2002.

[44] C. Duque-Daza, M. Baig, D. Lockerby, S. Chernyshenko, and C. Davies. Modelling turbulent skin-friction control using linearised Navier-Stokes equations. *J. Fluid Mech.*, 702:403–414, 2012.

[45] F. Forlani and N. Minnaja. Thickness influence in breakdown phenomena of thin dielectric films. *Phys. Status Solidi B*, 4(2):311–324, 1964.

[46] M. Frigo and S. Johnson. The design and implementation of FFTW3. *Proc. IEEE*, 93(2):216–231, 2005.

[47] B. Frohnapfel, Y. Hasegawa, and M. Quadrio. Money versus time: evaluation of flow control in terms of energy consumption and convenience. *J. Fluid Mech.*, 700:406–418, 2012.

[48] K. Fukagata, K. Iwamoto, and N. Kasagi. Contribution of Reynolds stress distribution to the skin friction in wall-bounded flows. *Phys. Fluids*, 14(11):L73–L76, 2002.

[49] M. Gad-el Hak. *Flow Control – Passive, Active and Reactive Flow Management*. Cambridge University Press, Cambridge, 2000.

[50] B. Ganapathisubramani, N. Hutchins, J. Monty, D. Chung, and I. Marusic. Amplitude and frequency modulation in wall turbulence. *J. Fluid Mech.*, 712:61–91, 2012.

[51] R. Garcia-Mayoral and J. Jiménez. Drag reduction by riblets. *Phil. Trans. R.Soc. A*, 369(1940):1412–1427, 2011.

[52] R. Garcia-Mayoral and J. Jiménez. Hydrodynamic stability and the breakdown of the viscous regime over riblets. *J. Fluid. Mech.*, 678:317–347, 2011.

[53] D. Gatti and M. Quadrio. Performance losses of drag-reducing spanwise forcing at moderate values of the Reynolds number. *Phys. Fluids*, 25:125109(17), 2013.

[54] A. Gent. A new constitutive relation for rubber. *Rubber Chem. Technol.*, 69(1):59–61, 1996.

[55] A. P. Gerratt and S. Bergbreiter. Dielectric breakdown of PDMS thin films. *J. Micromech. Microeng.*, 23(6):067001, June 2013.

[56] Y. F. Goh, Y. S. Poon, S. Akbari, H. Shea, and A. Koh, S. J. Ultra-actuation of acrylic-based artificial muscles. In *Proc. EuroEAP*, 2014.

[57] K. Gouder. *Turbulent Friction Drag Reduction Using Electroactive Polymer Surfaces.* PhD thesis, Imperical College, London, 2011.

[58] K. Gouder, M. Potter, and J. Morrison. Turbulent friction drag reduction using electroactive polymer and electromagnetically driven surfaces. *Exp. Fluids*, 54(1):1441, 2013.

[59] A. Güttler. *High accuracy determination of skin-friction differences in an air channel flow based on pressure drop measurement.* PhD thesis, Karlsruhe Institute of Technology, 2015.

[60] H. Haus, M. Matysek, H. Mößinger, and H. F. Schlaak. Modelling and characterization of dielectric elastomer stack actuators. *Smart Mater. Struct.*, 22(10):104009, 2013.

[61] B. Helgee and P. Bjellheim. Electric breakdown strength of aromatic polymers: dependence on film thickness and chemical structure. *IEEE Trans. Elect. Insulation*, 26(6):1147–1152, Dec. 1991.

[62] C.-M. Ho and Y.-C. Tai. MEMS and fluid flow. *Ann. Rev. Fluid Mech.*, 30:579–612, 1998.

[63] M. Hodgins, G. Rizzello, D. Naso, and A. York. An electromechanically coupled model for the dynamic behavior of a dielectric electro-active polymer actuator. *Smart Mater. Struct.*, 23(10):104006, 2014.

[64] J. Huang, S. Shian, R. M. Diebold, Z. Suo, and D. R. Clarke. The thickness and stretch dependence of the electrical breakdown strength of an acrylic dielectric elastomer. *Appl. Phys. Lett.*, 101(12):122905, 2012.

[65] N. Hutchins and I. Marusic. Evidence of very long meandering features in the logarithmic region of turbulent boundary layers. *J. Fluid Mech.*, 2007.

[66] K. Iwamoto, K. Fukagata, N. Kasagi, and Y. Suzuki. Friction drag reduction achievable with near-wall manipulation at high Reynolds numbers. *Phys. Fluids*, 17(011702):4, 2005.

[67] J. Jansen, J. Van Doren, M. Heydary-Fyrozyaee, and Y. Yortsos. *Model-based control: bridging rigorous theory and advanced technology*, chapter Front controllability in two-phase porous media flow, pages 203–219. Springer, 2009.

[68] J. Jeong, F. Hussain, W. Schoppa, and J. Kim. Coherent structures near the wall in a turbulent channel flow. *J. Fluid Mech.*, 332:185–214, 1997.

[69] J. Jiménez, S. Hoyas, M. P. Simens, and Y. Mizuno. Turbulent boundary layers and channels at moderate reynolds numbers. *J. Fluid Mech.*, 657:335–360, 8 2010.

[70] J. Jiménez and A. Pinelli. The autonomous cycle of near-wall turbulence. *J. Fluid Mech.*, 389:335–359, 1999.

[71] R. Jones, W. Peng, B. Lassen, and R. Sarban. Dielectric elastomers and compliant metal electrode technology. In *15th IEEE Medit. Electrotech. Conf.*, pages 368–373, April 2010.

[72] W. Jung, N. Mangiavacchi, and R. Akhavan. Suppression of turbulence in wall-bounded flows by high-frequency spanwise oscillations. *Phys. Fluids A*, 4 (8):1605–1607, 1992.

[73] M. Jungmann. *Entwicklung elektrostatischer Festkörperaktoren mit elastischen Dielektrika für den Einsatz in taktilen Anzeigefeldern.* PhD thesis, Technische Universität Darmstadt, 2004.

[74] R. Karsten and H. F. Schlaak. Adaptive absorber based on dielectric elastomer stack actuator with variable stiffness. In *Proc. SPIE, EAPAD*, volume 8340, pages 834020–834020–8, 2012.

[75] N. Kasagi, Y. Hasegawa, and K. Fukagata. Towards cost-effective control of wall turbulence for skin-friction drag reduction. volume 132 of *Adv. Turb. XII*, pages 189–200. Springer, 2009.

[76] N. Kasagi, Y. Suzuki, and K. Fukagata. MEMS-based feedback control of turbulence for drag reduction. *Annu. Rev. Fluid Mech.*, 41:231–251, 2009.

[77] C. Keplinger, T. Li, R. Baumgartner, Z. Suo, and S. Bauer. Harnessing snap-through instability in soft dielectrics to achieve giant voltage-triggered deformation. *Soft Matter*, 8:285–288, 2012.

[78] H. Kim and F. Shi. Thickness dependent dielectric strength of a low-permittivity dielectric film. *IEEE Trans. Dielect. Elect. Insulation*, 8(2):248–252, Apr. 2001.

[79] J. Kim and T. Bewley. A linear systems approach to flow control. *Annu. Rev. Fluid Mech.*, 39:383–417, 2007.

[80] J. Kim and F. Hussain. Propagation velocity of perturbations in turbulent channel flow. *Phys. Fluids A*, 5(3):695–706, 1993.

[81] J. Kim and P. Moin. Numerical investigation of turbulent channel flow. *J. Fluid Mech.*, 118:341–377, 1982.

[82] J. Kim, P. Moin, and R. Moser. Turbulence statistics in fully developed channel flow at low Reynolds number. *J. Fluid Mech.*, 177:133–166, 1987.

[83] S. J. Kline, W. C. Reynolds, F. A. Schraub, and P. W. Runstadler. The structure of turbulent boundary layers. *J. Fluid Mech.*, 30:741–773, 1967.

[84] G. Kofod. *Dielectric elastomer actuators*. PhD thesis, The Technical University of Denmark, 2001.

[85] G. Kofod. The static actuation of dielectric elastomer actuators: how does pre-stretch improve actuation? *J. Phys. D*, 41(21):215405, 2008.

[86] G. Kofod, M. Paajanen, and S. Bauer. Self-organized minimum-energy structures for dielectric elastomer actuators. *Appl. Phys. A*, 85(2):141–143, 2006.

[87] G. Kofod, P. Sommer-Larsen, R. Kornbluh, and R. Pelrine. Actuation response of polyacrylate dielectric elastomers. *J. Intell. Mater. Syst. Struct.*, 14(12):787–793, Dec. 2003.

[88] M. Kollosche and G. Kofod. Electrical failure in blends of chemically identical, soft thermoplastic elastomers with different elastic stiffness. *Appl. Phys. Lett.*, 96(7):071904, 2010.

[89] M. Kollosche, H. Stoyanov, H. Ragusch, S. Risse, A. Becker, and G. Kofod. Electrical breakdown in soft elastomers: Stiffness dependence in un-pre-stretched elastomers. In *Proc. 10th IEEE, ICSD*, pages 1–4. IEEE Piscataway, NJ, USA, 2010.

[90] R. D. Kornbluh, R. Pelrine, J. Joseph, R. Heydt, Q. Pei, and S. Chiba. High-field electrostriction of elastomeric polymer dielectrics for actuation. In *Proc. SPIE, EAPAD*, volume 3669, pages 149–161, 1999.

[91] R. D. Kornbluh, R. Pelrine, Q. Pei, S. Oh, and J. Joseph. Ultrahigh strain response of field-actuated elastomeric polymers. In *Proc. SPIE, EAPAD*, volume 3987, pages 51–64, 2000.

[92] G. Kovacs and L. Düring. Contractive tension force stack actuator based on soft dielectric eap. In *Proc. SPIE,EAPAD*, volume 7287, pages 72870A–72870A–15, 2009.

[93] F. Laadhari, L. Skandaji, and R. Morel. Turbulence reduction in a boundary layer by a local spanwise oscillating surface. *Phys. Fluids*, 6 (10):3218–3220, 1994.

[94] S. Lardeau and M. A. Leschziner. The streamwise drag-reduction response of a boundary layer subjected to a sudden imposition of transverse oscillatory wall motion. *Phys. Fluids*, 25(7):–, 2013.

[95] C. Lee, J. Kim, D. Babcock, and R. Goodman. Application of neural networks to turbulence control for drag reduction. *Phys. Fluids*, 9:1740–1747, 1997.

[96] C. Lee, J. Kim, and H. Choi. Suboptimal control of turbulent channel flow for drag reduction. *J. Fluid Mech.*, 358:245–258, 1998.

[97] P. Lochmatter. *Development of a Shell-like Electroactive Polymer EAP Actuator.* PhD thesis, Swiss Federal Institute of Technology, 2007.

[98] P. Lotz. *Dielektrische Elastomerstapelaktoren für ein peristaltisches Fluidfördersystem.* PhD thesis, Technische Universitäet Datmstadt, 2010.

[99] P. Lotz, M. Matysek, and H. F. Schlaak. Fabrication and application of miniaturized dielectric elastomer stack actuators. *IEEE/ASME Trans. Mechatron.*, 16(1):58–66, 2011.

[100] S. S. Lu and W. Willmarth. Measurements of the structure of the reynolds stress ina turbulent boundary layer. *J. Fluid. Mech.*, 60:481–511, 1973.

[101] P. Luchini, F. Manzo, and A. Pozzi. Resistance of a grooved surface to parallel flow and cross-flow. *J. Fluid Mech.*, 228:87–109, 1991.

[102] P. Luchini and M. Quadrio. A low-cost parallel implementation of direct numerical simulation of wall turbulence. *J. Comp. Phys.*, 211(2):551–571, 2006.

[103] l. Maffli, S. Rosset, and H. R. Shea. Zipping dielectric elastomer actuators: characterization, design and modeling. *Smart Mater. Struct.*, 22(10):104013, 2013.

[104] I. Marusic, D. D. Joseph, and K. Mahesh. Laminar and turbulent comparisons for channel flow and flow control. *J. Fluid Mech.*, 570:467–477, 2007.

[105] R. Mathis, N. Hutchins, and I. Marusic. Large-scale amplitude modulation of the small-scale structures in turbulent boundary layers. *J. Fluid Mech.*, 2009.

[106] M. Matysek. *Dielektrische elastomelastomer in multilayer-technologie für taktile displays*. PhD thesis, Technische Universität Darmstadt, 2009.

[107] M. Matysek, H. Haus, H. Mößinger, D. Brokken, P. Lotz, and H. F. Schlaak. Combined driving and sensing circuitry for dielectric elastomer actuators in mobile applications. In *Proc. SPIE, EAPAD*, volume 7976, pages 797612–797612–11, San Diego, CA, USA, 2011.

[108] R. Moarref and M. R. Jovanović. Model-based design of transverse wall oscillations for turbulent drag reduction. *J. Fluid Mech.*, 707:205–240, 2012.

[109] E. M. Mockensturm and N. Goulbourne. Dynamic response of dielectric elastomers. *Int. J. Nonlinear Mech.*, 41(3):388 – 395, 2006.

[110] N. V. Nikitin. On the mechanism of turbulence suppression by spanwise surface oscillations. *Fluid Dyn.*, 35(2):185–190, 2000.

[111] R. W. Ogden, G. Saccomandi, and I. Sgura. Fitting hyperelastic models to experimental data. *Comput. Mech.*, 34(6):484–502, 2004.

[112] T. Oliver, N. Malaya, U. Rhys, and R. Moser. Estimating Uncertainties in Statistics Computed from DNS. *Phys. Fluids*, 26(3):–, 2014.

[113] J. Pang and K.-S. Choi. Turbulent drag reduction by Lorentz force oscillation. *Phys. Fluids*, 16(5):L35–L38, 2004.

[114] R. Pelrine and R. Kornbluh. Variable-stiffness-mode dielectric elastomer devices. *Adv. Sci. Tech.*, 61:192, 2008.

[115] R. Pelrine, R. Kornbluh, J. Joseph, and S. Chiba. Electrostriction of polymer films for microactuators. In *Proc. IEEE, MEMS*, pages 238–243. IEEE, 1997.

[116] R. Pelrine, R. Kornbluh, J. Joseph, R. Heydt, Q. Pei, and S. Chiba. High-field deformation of elastomeric dielectrics for actuators. *Mater. Sci. Eng. C*, 11(2):89 – 100, 2000.

[117] R. Pelrine, R. Kornbluh, Q. Pei, and J. Joseph. High-speed electrically actuated elastomers with strain greater than 100%. *Science*, 287(5454):836–839, 2000.

[118] R. Pelrine, R. D. Kornbluh, J. Eckerle, P. Jeuck, S. Oh, Q. Pei, and S. Stanford. Dielectric elastomers: generator mode fundamentals and applications. In *Proc. SPIE, EAPAD*, volume 4329, pages 148–156, 2001.

[119] R. E. Pelrine, R. D. Kornbluh, and J. P. Joseph. Electrostriction of polymer dielectrics with compliant electrodes as a means of actuation. *Sens. Actuators A*, 64:77–85, 1998.

[120] A. Pimpin, Y. Suzuki, and N. Kasagi. Micro electrostrictive actuator with metal compliant electrodes for flow control applications. In *Proc. IEEE, MEMS*, pages 478–481, 2004.

[121] J.-S. Plante. *Dielectric elastomer actuators for binary robotics and mechatronics*. PhD thesis, MIT, 2006.

[122] J.-S. Plante and S. Dubowsky. Large-scale failure modes of dielectric elastomer actuators. *Int. J. Solids Struct.*, 43(25-26):7727–7751, Dec. 2006.

[123] A. Poole and J. D. Booker. Classification and selection of actuator technologies with consideration of stimuli generation. In *Proc. SPIE, EAPAD*, volume 6927, pages 692728–692728–10, 2008.

[124] S. Pope. *Turbulent Flows*. Cambridge University Press, Cambridge, 2000.

[125] A. Price, M. Giousouf, H. Krüger, J. Maas, and J. Wagner. Advancement of dielectric elastomer actuators towards industrial applications. In *Proc. ACTUATOR*, 2014.

[126] M. Quadrio. Drag reduction in turbulent boundary layers by in-plane wall motion. *Phil. Trans. R. Soc. A*, 369(1940):1428–1442, 2011.

[127] M. Quadrio and P. Luchini. Integral time-space scales in turbulent wall flows. *Phys. Fluids*, 15(8):2219–2227, 2003.

[128] M. Quadrio and P. Ricco. Initial transient of a turbulent boundary layer with spanwise oscillations. Technical report, Dipartimento di Ingegneria Aerospaziale – Politecnico di Milano – DIA-SR 02-14, 2002.

[129] M. Quadrio and P. Ricco. Initial response of a turbulent channel flow to spanwise oscillation of the walls. *J. Turbul.*, 4(7), 2003.

[130] M. Quadrio and P. Ricco. Critical assessment of turbulent drag reduction through spanwise wall oscillation. *J. Fluid Mech.*, 521:251–271, 2004.

[131] M. Quadrio and P. Ricco. The laminar generalized Stokes layer and turbulent drag reduction. *J. Fluid Mech.*, 667:135–157, 2011.

[132] M. Quadrio, P. Ricco, and C. Viotti. Streamwise-traveling waves of spanwise wall velocity for turbulent drag reduction. *J. Fluid Mech.*, 627:161–178, 2009.

[133] M. Quadrio and S. Sibilla. Numerical simulation of turbulent flow in a pipe oscillating around its axis. *J. Fluid Mech.*, 424:217–241, 2000.

[134] M. Randazzo, R. Buzio, G. Metta, G. Sandini, and U. Valbusa. Architecture for the semi-automatic fabrication and assembly of thin-film based dielectric elastomer actuators. In *Proc. SPIE, EAPAD*, volume 6927, pages 69272D–69272D–10, 2008.

[135] O. Reynolds. An experimental investigation on the circumstances which determine whether the motion of water shall be direct or sinuous, and the law of resistance in parallel channels. *Proc. R. Soc. London A*, 35:84, 1883.

[136] P. Ricco. Modification of near-wall turbulence due to spanwise wall oscillations. *J. Turbul.*, 5(24), 2004.

[137] P. Ricco, C. Ottonelli, Y. Hasegawa, and M. Quadrio. Changes in turbulent dissipation in a channel flow with oscillating walls. *J. Fluid Mech.*, 700:77–104, 2012.

[138] P. Ricco and M. Quadrio. Wall-oscillation conditions for drag reduction in turbulent channel flow. *Intl J. Heat Fluid Flow*, 29:601–612, 2008.

[139] P. Ricco and S. Wu. On the effects of lateral wall oscillations on a turbulent boundary layer. *Exp. Therm. Fluid Sci.*, 29(1):41–52, 2004.

[140] S. K. Robinson. Coherent motions in the turbulent boundary layer. *Ann. Rev. Fluid Mech.*, 23:601–639, 1991.

[141] W. C. Röntgen. Über die durch Electricität bewirkten Form- und Volumenänderungen von dielectrischen Körpern. *Ann. Phys.*, 11:771–786, 1880.

[142] S. Rosset, P. Gebbers, B. M. O'Brien, and H. Shea. The need for speed. In *Proc. SPIE, EAPAD*, volume 8340, pages 4–12, 2012.

[143] S. Rosset, M. Niklaus, P. Dubois, and H. Shea. Mechanical characterization of a dielectric elastomer microactuator with ion-implanted electrodes. *Sens. Actuators A*, 144(1):185 – 193, 2008.

[144] S. Rosset, M. Niklaus, P. Dubois, and H. Shea. Large-stroke dielectric elastomer actuators with ion-implanted electrodes. *J. Microelectromech. Syst.*, 18(6):1300–1308, Dec 2009.

[145] S. Rosset and H. R. Shea. Flexible and stretchable electrodes for dielectric elastomer actuators. *Appl. Phys. A*, 110(2):281–307, 2013.

[146] H. Schlichting and K. Gersten. *Boundary-Layer Theory*. Springer, Berlin, 2000.

[147] J. Sheng, H. Chen, B. Li, and Y. Wang. Nonlinear dynamic characteristics of a dielectric elastomer membrane undergoing in-plane deformation. *Smart Mater. Struct.*, 23(4):045010, 2014.

[148] L. Skandaji. Etude de la structure d'une couche limite turbulente soumise à des oscillations trasversales de la paroi. *PhD Thesis, Ecole Centrale de Lyon*, 1997.

[149] M. Skote. Turbulent boundary layer flow subject to streamwise oscillation of spanwise wall-velocity. *Phys. Fluids*, 23(081703):4, 2011.

[150] M. Skote. Temporal and spatial transients in turbulent boundary layer flow over an oscillating wall. *Int. J. Heat Fluid Flow*, 38:1–12, 2012.

[151] G. A. Slipher and J. E. Hubbard. Exploitation of higher-order membrane modes for improved synthetic jet performance. *AIAA J*, 47:1388–1407, 2009.

[152] C. Smith and S. Schwartz. Observation of streamwise rotation in the near-wall region of a turbulent boundary layer. *Phys. Fluids*, 26(3):641, 1983.

[153] C. R. Smith and S. P. Metzler. The characteristics of low-speed streaks in the near-wall region of a turbulent boundary layer. *J. Fluid Mech.*, 129:27–54, 4 1983.

[154] P. Spalart and J. McLean. Drag reduction: enticing turbulence, and then an industry. *Phil. Trans. R. Soc. A*, 369(1940):1556–1569, 2011.

[155] K. H. Stark and C. G. Garton. Electric strength of irradiated polythene. *Nature*, 176(4495):1225–1226, Dec. 1955.

[156] P. Steinmann, M. Hossain, and G. Possart. Hyperelastic models for rubber-like materials: consistent tangent operators and suitability for treolar's data. *Arch. Appl. Mech.*, 82(9):1183–1217, 2012.

[157] Z. Suo. Theory of dielectric elastomers. *Acta Mech. Solida Sin.*, 23:549–578, 2010.

[158] S. Tamano and M. Itoh. Drag reduction in turbulent boundary layers by spanwise traveling waves with wall deformation. *J. Turbul.*, 13:N9, 2012.

[159] T. Theodorsen. Mechanism of turbulence. In *Proc. Midwest. Conf. Fluid Mech. 2nd, Columbus, Ohio*, pages 1–18, 1952.

[160] E. Touber and M. Leschziner. Near-wall streak modification by spanwise oscillatory wall motion and drag-reduction mechanisms. *J. Fluid Mech.*, 693:150–200, 2012.

[161] L. Treolar. *The Physics of Rubber Elasticity.* Oxford University Press, 1975.

[162] A. Tröls, A. Kogler, R. Baumgartner, R. Kaltseis, C. Keplinger, R. Schwödiauer, I. Graz, and S. Bauer. Stretch dependence of the electrical breakdown strength and dielectric constant of dielectric elastomers. *Smart Mater. Struct.*, 22(10):104012, 2013.

[163] S. Trujillo, D. Bogard, and K. Ball. Turbulent boundary layer drag reduction using an oscillating wall. *AIAA J.*, 1997.

[164] P. Viswanath. Aircraft viscous drag reduction using riblets. *Prog. Aerospace Sci.*, 38:571 – 600, 2002.

[165] G. Vittori and R. Verzicco. Direct simulation of transition in an oscillatory boundary layer. *J. Fluid Mech.*, 371:207–232, 1998.

[166] J. Wagner, J. Krause, K. Clauberg, T. Feller, E. Orselli, C. Schilling, D. Lellinger, I. Alig, D. Uhl, H. Bö se, R. Rabindranath, H.-R. Kretschmer, O. Theile, P. Lotz, T. Grotepaß, H. Haus, H. Mößinger,

and H. Schlaak. Multilayer dielectric elastomer stack actuators. In *Proc. ACTUATOR*, 2014.

[167] J. M. Wallace, H. Eckelmann, and S. Brodkey. The wall region in turbulent shear flow. *J Fluid. Mech.*, 54:39–48, 1972.

[168] A. Wingert, M. Lichter, and S. Dubowsky. On the design of large degree-of-freedom digital mechatronic devices based on bistable dielectric elastomer actuators. *IEEE/ASME Trans. Mechatronics*, 11(4):448–456, 2006.

[169] A. Yakeno, Y. Hasegawa, and N. Kasagi. Modification of quasi-streamwise vortical structure in a drag-reduced turbulent channel flow with spanwise wall oscillation. *Phys. Fluids*, 26(8):–, 2014.

[170] I. Yudhistira and M. Skote. Direct numerical simulation of a turbulent boundary layer over an oscillating wall. *J. Turbul.*, 12:N9, 2011.

[171] S. Zaremski and M. Amitay. Electroactive polymer based flow control at low reynolds numbers. In *64th Annual Meeting*, volume 56, 2011.

[172] X. Zhang, C. Löwe, M. Wissler, B. Jähne, and G. Kovacs. Dielectric elastomers in actuator technology. *Adv. Eng. Mater.*, 7:361–367, 2005.

[173] X. Zhao and Z. Suo. Method to analyze electromechanical stability of dielectric elastomers. *Appl. Phys. Lett.*, 91(6), 2007.

[174] X. Zhao and Q. Wang. Harnessing large deformation and instabilities of soft dielectrics: Theory, experiment, and application. *Appl. Phys. Rev.*, 1(2):–, 2014.

Nomenclature

Latin letters

upper case

symbol	SI unit	description
A	m/s	Wall oscillation velocity
A^+	–	Nondimensional oscillation velocity
A^+_{th}	–	Nondimensional threshold velocity
A^+_{ref}	–	Oscillation velocity nondimensionalized by reference viscous units
A^+_{act}	–	Oscillation velocity nondimensionalized by actual viscous units
C_f	–	Skin friction coefficient
$C_{f,0}$	–	Skin friction of the unmaniplated flow
$C^{(r)}_{f,0}$	–	Skin friction on the reference section of the unmaniplated flow
$C^{(r)}_f$	–	Skin friction on the reference section of the controlled flow
C	–	Capacitance
C	F	Capacitance
C^∞	–	Undefinitely differentiable function
E	V/m	Electric field
E_B	V/m	Dielectric breakdown field strength
E_B^{int}	V/m	Intrinsic dielectric breakdown field strength
F_e	N	Force in equibiaxial load
F_x, F_y, F_z	N	Force in x-, y- and z- direction
G	–	Gain
H	m	Channel height

J_m	–	Gent limiting stretch
L_A^+	m	Nondimensional length of the actuator surface
L_{tap}	m	Streamwise distance of two consecutive pressure taps
L_x, L_y, L_z	m	Domain length in the x-, y- and z- direction
N_x, N_x, N_x	–	Number of Fourier modes/collocation points
	–	in the x-, y- and z- direction
Ra	μm	Average surface roughness
Re	–	Reynolds number
Re_b	–	Reynolds number based on the bulk velocity
Re_c	–	Reynolds number based on the centerline velocity
Re_τ	–	Reynolds number based on the friction velocity
$Re_{\tau,0}$	–	Reynolds number based on the friction velocity
	–	of an unmanipulated flow
Re_δ	–	Reynolds number based on the Stokes layer thickness
R	–	Drag reduction rate
R_{hom}	–	Drag reduction rate of an homogeneously controlled
	–	channel flow
R_{max}	–	Maximum drag reduction rate
$Q_{1\ldots4}$	–	Quadrands of the $\langle u'v' \rangle$ quadrant map
P	W	Pumping power
P_0	W	Pumping power of the unmanipulated flow
P_{in}	W	Input power
S	–	Net power saving rate
S_{max}	–	Maximum net power saving rate
S^+	–	Correlation coefficient for drag reduction
S_x, S_y, S_z	–	Strain in x-, y- and z-direction
T	s	Period of wall oscillation
T^+	–	Nondimensional period of wall oscillation
T^+_{opt}	–	Optimal nondimensional period of wall oscillations
T_{sim}	–	Nondimensional total simulation time
U_b	m/s	Bulk velocity
U_c	m/s	Centerline velocity
$U_{c,\log}$	m/s	Centerline velocity predicted by the defect velocity law

U_p	m/s	Centerline velocity of a Poiseuille flow
U_{tot}	J	Total energy
U_{m}	J	Mechanical energy
U_{e}	J	Electrical energy
U_{s}	J	External source energy
W	m	Channel width
Y	Pa	Young elastic modulus
Z_e	Ω	Electrical impedance
Z_{mech}	Ns/m	Mechanical impedance

lower case

symbol	SI unit	description
a	m^2	Electrode area in actuated state
a_0	m^2	Electrode area in unactuated state
a_m^+	–	Maximum nondimensional acceleration
c	Kg/s	Damping coefficient
c^+	–	Nondimensional wave speed
c_f	–	Skin-friction based on the centerline velocity
c_w	m/s	Convection speed of skin-friction fluctuations
c_w^+	–	Nondimensional convection speed
	–	of skin-friction fluctuations
d	m	Actuation stroke
d_0	m	Electrode diameter in the unactuated state
d_1	m	Electrode diameter after pre-stretching
d_{act}	m	Electrode diameter upon actuation
d_{max}	m	Maximum deformation upon actuation
f_0 f_e	1/s	Frequency of the electrical signal
$f_{e,\text{lim}}$	1/s	Cut-off frequency
f_{res}	1/s	Resonance frequency
h	m	Channel semi-height
h^+	–	Nondimensional channel semi-height

k	N/m	Stiffness
ℓ^+	–	Nondimensional reference Stokes layer thickness
m	kg	Mass
Δp	Pa	Pressure difference
Δp_{fm}	Pa	Pressure drop across the flow meter
p_w	Pa	Wall pressure
p_e	Pa	Maxwell pressure
t	s	Time
t_ν	s	Viscous time
u	m/s	Velocity
$\tilde{u}$	m/s	Phase-averaged velocity
u^+	m/s	Nondimensional velocity
u^+_{act}	m/s	Velocity nondimensionalized with actual viscous units
u', v', w'	m/s	Velocity fluctuations in x-, y- and z-direction
u_τ	m/s	Friction velocity
$u_\tau^{(r)}$	m/s –	Friction velocity computed with the wall shear in the reference section
$\langle u \rangle^+_x$	m/s	Velocity average in x-direction and time
$\langle w \rangle$	m/s	Spanwise velocity
$\langle \tilde{w} \rangle$	m/s	Average spanwise velocity
$\langle \tilde{w}^+ \rangle$	–	Nondimensional average spanwise velocity
w_w	m/s	Spanwise wall velocity
x, y, z	m –	Extent of the electrode area in x-,y-,z- coordinates upon actuation
x_0, y_0, z_0	m –	Extent of the electrode area in x-,y-,z- coordinates in unactuated state
x^+, y^+, z^+	–	Nondimensional spatial coordinates

Greek letters

upper case

symbol	SI unit	description

Φ	V	Potential difference
Ψ	–	Profile function

lower case

symbol	SI unit	description
α	–	Empirical coefficient
γ	–	Empirical coefficient
δ	m	Stokes layer thickness
δ_ν	m	Viscous length
δ_{opt}	m	Optimal Stokes layer thickness
ϵ_0	F/m	Vacuum permittivity
ϵ_r	–	Dielectric contant (relative permittivity)
σ	Pa	Stress
σ_x, σ_y, σ_z	Pa	Stresses in the x-, y-, z-direction
$\sigma_{p,x}$, $\sigma_{p,z}$	Pa	Pre-stresses in the x-, z-direction
σ_R	–	Standard uncertainty on drag reduction
λ_x, λ_y, λ_z	–	Stretch in x-, y-, z-direction
$\lambda_{p,x}$, $\lambda_{p,z}$	–	Pre-stretch in x-, z-direction
λ^{act}	–	Active stretch
λ^{bi}	–	Equi-biaxial stretch
λ^+	–	Nondimensional wavelenght
ν	m^2/s	Kinematic viscosty
μ_e	Pa	Shear modulus
τ	Pa	Shear stress
τ_0	Pa	Shear stress in the uncontrolled flow
τ_x	Pa	Streamwise wall shear stress
$\tau_{x,0}$	Pa –	Streamwise wall shear stress in the uncontrolled flow
ρ	kg/m^3	Density
ρ_s	Ω m	Bulk resistivity

ρ_e	$\mathrm{kg/m^3}$	Area density
κ	–	von Karman constant
κ^+	–	Nondimensional wavenumber
κ^+_{ref}	–	Wavenumber nondimensionalized
	–	with the reference viscous units
κ^+_{act}	–	Wavenumber nondimensionalized
	–	with the actual viscous units
ω	1/s	Angular frequency
ω^+	1/s	Nondimensional angular frequency
ω^+_{ref}	1/s	Angular frequency nondimensionalized
	–	with the reference viscous units
ω^+_{act}	1/s	Angular frequency nondimensionalized
	–	with the actual viscous units

Abbreviations

Abbreviations

symbol	description
AC	Alternating current
CAM	CAMera
CCD	Charged Coupled Device
CFR	Constant Flow Rate
CMOS	Complementary Metal Oxide Semiconductor
CPG	Constant Pressure Gradient
DEA	Dielectric Elastomer Actuator
DEMES	Dielectric Elastomer Minimum Energy Structures
DESA	Dielectric Elastomer Stack Actuator
DI	Drag Increase
DR	Drag Reduction
DNS	Direct Numerical Simulation
EAP	ElectroActive Polymer
EMI	ElectroMechanical Instability
FOV	Fields Of View
fps	frames per second
LL	Limited Width
LSS	Low Speed Streak
LW	Limited Length
PDMS	PolyDiMethylSiloxane
PMMA	PolyMethyl MethAcrylate
PVC	PolyVinyl Chloride
PU	PolyUrethane
QSV	Quasi Streamwise Vortex
WT1	Wind Tunnel 1
WT2	Wind Tunnel 2
ZNMF	Zero Net Mass Flux

List of Figures

List of Tables

Davide Gatti

Institute for
Fluid Mechanics and Aerodynamics
Technische Universität Darmstadt
Alarich-Weiß-Str. 10
D-64287 Darmstadt
Germany

phone: +49 6151 16-3733
fax: +49 6151 16-2048
email:
gatti@csi.tu-darmstadt.de

Personal

Born on February 18, 1986, S. Angelo Lodigiano, Italy
(Italian citizenship)

Education

01/2012 - 12/2014	Doctoral research in Mechanical Engineering (Dr.-Ing.), Technische Universität Darmstadt, Darmstadt, Germany
03/2009 - 12/2011	studies in Aeronautical Engineering (M.Sc.), Politecnico di Milano, Milan Italy
09/2006 - 02/2009	studies in Aerospace and Aeronautical Engineering (B.Sc.), Politecnico di Milano, Milan Italy